UNIVERSIDAD NACIONAL AUTÓNOMA
DE MÉXICO

FACULTAD DE CIENCIAS

Development of a Kinetic Model for Strong Pulse X-ray Interaction with Diatomic Molecules

T E S I S

QUE PARA OBTENER EL TÍTULO DE:

Físico

PRESENTA:

Miguel Ángel Silva Toledo

TUTORA

Dra. Nina Rohringer

Ciudad Universitaria, CDMX

1. Datos del alumno
Silva
Toledo
Miguel Angel
57 14 25 67
Universidad Nacional Autónoma de
México
Facultad de Ciencias
Física
308598939

2. Datos del tutor
Dra.
Nina
Rohringer

3. Datos del sinodal 1
Dr.
José Ignacio
Jiménez
Mier y Terán

4. Datos del sinodal 2
Dr.
Víctor
Romero
Rochín

5. Datos del sinodal 3
Dra.
Rocío
Jaúregui
Renaud

6. Datos del sinodal 4
Dr.
Raúl
Rangel
Rojo

8. Datos del trabajo escrito
Development of a Kinetic Model for Strong Pulse X-ray Interaction
with Diatomic Molecules
111 p
2016

A mi familia y amigos de toda la vida

Abstract

Understanding the ultrafast motion of electrons and holes after the interaction with ultra-intense x-ray radiation is fundamental to a broad range of applications.

In this thesis we study the ultrafast electronic response of a molecular gas of carbon monoxide (CO) to the interaction with a x-ray Free-Electron Laser (XFEL) beam. X-ray Free-Electron Lasers (XFELs) are novel laser sources that produce x-ray pulses of umprecedented high intensity and in the femtosecond range.

A theoretical approach based on a molecular rate equation model, enables us to determine the time-dependent probabilities of all the energetically accessible involved electronic states by keeping track of the photoionization, fluorescence decay and Auger decay events. We couple the rate equations to the evolution of the XFEL photon flux, to account for the attenuation of the pulse as it propagates along the gas-phase medium.

Numerical simulations predict sequential multi-photoionization of the sample, which depends on XFEL beam parameters, such as the photon fluence, pulse duration and photon energy. It is found that CO under the influence of a XFEL beam interacts several times with a single x-ray pulse, by a sequence of inner-shell photoionization events followed by Auger decay. Pulses with comparable energy but decreasing pulse duration favor the production of lower charge states, whereas pulses with increasing duration lead to severe electronic damage and therefore to higher charge states. Moreover, CO becomes quasi-transparent at high intensities, owing to core-hole formation and to the reduction of the absorption probability of the created ion.

We also review an experimental approach to stimulate Resonant Inelastic X-ray Scattering (sRIXS) in CO and study the background signal that can mask the sRIXS. For this, we extend the above model to the interaction with a pump-probe field that is temporally overlapped. By tuning the peak intensity of the pump pulse, one may control the transmission of the probe pulse and vice versa, thus, reducing the electronic damage induced by the probe field.

Resumen

El entendimiento del movimiento ultra rápido de electrones y huecos en moléculas al interactuar con radiación de rayos-x de gran intensidad es fundamental para diversas aplicaciones.

En esta tesis se desarrolla un estudio sobre la respuesta electrónica ultra rápida que experimenta un gas molecular de monóxido de carbono (CO) cuando se le hace incidir un haz de rayos-x generado por un láser de electrones libres. Los láseres de electrones libres de rayos-x (XFELs) son fuentes de láseres pulsados de rayos-x de alta intensidad y con duraciones del orden de femtosegundos.

Para este trabajo se desarrolla un enfoque teórico basado en un modelo de ecuaciones de tasas de cambio, el cual permite determinar la dependencia temporal de las probabilidades de ocupación de todos los estados que son energéticamente accesibles. Para ello, se rastrean procesos como fotoionización, decaimiento Auger y fluorescencia. Asimismo, para tomar en cuenta la propagación del pulso de rayos-x a lo largo del medio gaseoso, las ecuaciones de tasas de cambio se acoplan a la ecuación de movimiento del flujo de fotones.

Las simulaciones numéricas predicen daño electrónico -reacomodamiento o pérdida de electrones- en la molécula, el cual depende de los parámetros del haz de luz, como son el flujo de fotones, la duración del pulso y la energía del fotón. Se encuentra que la molécula interacciona varias veces con un sólo pulso de rayos-x, mediante una secuencia de eventos de fotoionización seguidos por decaimiento Auger. Pulsos con energía comparable pero con menor duración contribuyen a la formación de iones con cargas bajas, en tanto que pulsos más duraderos favorecen la producción de iones más positivamente cargados y, por tanto, a una mayor afectación a la estructura electrónica de la molécula. Además, se halla que el CO se vuelve cuasi transparente a muy altas intensidades, debido a la formación de huecos en capas internas y a la reducción de la probabilidad de absorción por el ion creado.

Al final, se hace breve revisión de un enfoque experimental para estimular dispersión Raman en rayos-x (sRIXS) con CO y se estudia la señal de fondo que podría obtenerse al capturar el espectro correspondiente.

Teniendo este objetivo, se extiende el modelo de un sólo pulso a la situación en donde un pulso de bombeo y otro de prueba están superpuestos temporalmente e inciden en el gas molecular.

Las simulaciones muestran que al ajustar la intensidad pico del pulso de bombeo, se puede controlar la transmisión del pulso de prueba y viceversa, reduciendo así el daño electrónico inducido por el pulso de bombeo.

Contents

Chapter 1

Introduction

X-rays are a type of electromagnetic radiation with wavelengths ranging from $\sim$ 100 eV to $\sim$ 100 keV (10^{-2} to 10 nm.). They were discovered in 1895 by the German physicist Wilhelm Röntgen [1], and since then x-rays have been a valuable tool for medical, chemical and physical research and diagnosis.

Some useful properties and applications of x-ray radiation are: (1) the absorption of x-rays generally involves an inner-shell electron and the creation of an excited state, which relaxes via ejecting a photon and/or electron. The energy of the emitted particle in the relaxation process is element specific, which can be used as a complementary technique to characterize the chemical composition of a sample [2, 3, 4, 5]. (2) inner-shell relaxation is in the femtosecond (or shorter) temporal regime (10^{-15} s), in such a way that decay particles reflect the molecular geometry at the instant of x-ray absorption. (3) The energy carried by x-ray photons make them to have a relatively small probability of being absorbed. Consequently, due to the large penetration depth permits medical imaging and applications in airports and border security. (4) x-rays offer very short wavelengths of the order of interatomic distances in molecules, which allow to decipher structures in atomic detail, as they are diffracted by the atoms in a crystal or in a solid [6, 5].

In physics, chemistry and biology, the most used x-ray source of high brightness is synchrotron radiation, which is the spontaneous radiation from electrons moving in an undulator magnet located in an electron storage ring [7]. A large number of these facilities, so-called third generation facilities, have been built in many countries, since they have demonstrated to be of great advantage for the scientific, technological and industrial development of a nation. Even in Mexico initiatives have been presented for constructing the Mexican Synchrotron. The US Advanced Photon Source at the Argonne National Laboratory, the Positron-Elektron-Tandem-Ring-Anlage (PETRA) at the Deutsches Elektronen-Synchrotron (DESY) in Hamburg, Germany and

the SPring-8 in Hyogo Prefecture, Japan, are some of the current most powerful synchrotron radiation facilities in operation.

Useful as it is, synchrotron radiation has its limitations. The minimum x-ray pulse duration is about picoseconds (10^{-12} s), and the number of photons that one can focus on a small sample is limited, which makes challenging to do high-resolution spectroscopy. Moreover, x-ray synchrotron radiation is incoherent. Having a coherent x-ray source with a large number of photons focused on a few millimeters and squeezed in time duration of femtoseconds has long been a dream of many scientists. X-ray Free-Electron Laser (XFEL) [8] dramatically improves the properties of synchrotron radiation sources. The XFEL radiation is transversely coherent, pulses are femtoseconds long, and the number of photons focused to an area surpasses third generation facilities by roughly nine orders of magnitude or larger [9].

Over the last recent years researchers carried out a considerable amount of experiments with these ultrafast and ultra-intense x-ray pulses. Among them are the creation of an atomic scale motion picture of a chemical process [10] or the ability to unravel the complex molecular structure of a single protein or virus [11, 12]. The unprecedented high peak brightness of the x-ray pulses enabled the first realization of an inner-shell atomic x-ray laser in the keV photon-energy regime [13]. Also, it has been possible to study matter under extreme conditions (similar to those in the interior of planets) [14, 15, 16], the nanoscale dynamics in a material [17] and even to better understand superconductivity [18]. Such investigations have unleashed further work on femtochemistry, x-ray quantum optics, structural biology, warm dense matter and solid-state physics, which may lead to the development of new medicines and give rise to the creation of new materials with optimized properties.

Further research using ultrafast and ultra-intense x-rays will definitely contribute to revolutionize our understanding of biological, chemical and physical processes and may pave the way to their control.

1.1 Free-electron lasers

Existent x-ray Free-Electron Lasers (FELs) are the extreme ultraviolet (EUV) and soft x-ray ($\sim$ 300 eV to a few keV) Free-electron -LASer in Hamburg (FLASH) at DESY [19] and the seeded Free-Electron laser Radiation for Multidisciplinary Investigations (FERMI), in Trieste, Italy. The Linac Coherent Light Source (LCLS) [20] in Menlo Park, California, USA. and the SPring-8 Angstrom Compact Free Electron Laser (SACLA) [8], which deliver photons in the hard x-ray domain (several keV or higher). A new hard x-ray facility currently under construction is the European XFEL [21] at DESY and there are plans to build two additional hard x-ray FELs; the SwissFEL at Paul

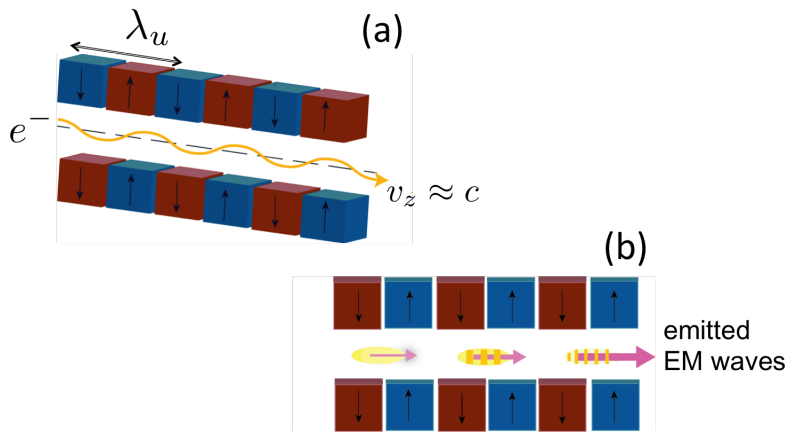

Figure 1.1: Mechanism of a x-ray Free-Electron Laser. (a) The optical amplification is activated when relativistic electrons enter to the periodic array of magnets (undulator) of period λ_u. (b) A self-organized (collective) interaction between electrons and the radiation they emit triggers the formation of bunches and microbunches. The electromagnetic emission of electrons in microbunches separated from each other by one wavelength is correlated and leads to a coherent amplification of the electromagnetic field [24]

.

Scherrer Institut in Switzerland [22] and the Pohang Accelerator Laboratory (PAL)-XFEL, in Pohang, Korea. New FELs will be added to FLASH and LCLS as an upgrade [23].

In the present section we give a simple and brief description of XFEL's mechanism. Of particular interest is what are the physical principles that make XFELs to provide ultra-intense, ultrafast and short wavelength pulses. Furthermore, we highlight the shape of the intensity distribution of the emitted XFEL radiation, since it distinguishes XFEL pulses from conventional lasers and represents a matter of concern for x-ray nonlinear processes.

1.1.1 Principle of XFEL mechanism

A Free-Electron Laser consists of a linear accelerator (LINAC) followed by a periodic structure of dipole magnets (undulator) that generate an alternating magnetic field with period λ_u, usually of a few millimeter. When a single electron propagates through the undulator, the periodic magnetic field forces it onto a oscillatory trajectory. Since the electron moves with a longitudinal speed close to the speed of light, $v_z \approx c$, and due to its transverse acceleration, an electromagnetic wave train -or pulse- of x-rays is emitted into a narrow forward cone (see Fig 1.1 (a)).

After the first "seed" electron enters to the undulator and radiates a wave train, the wave's magnetic field acts back onto the transverse velocity of

the rest of electrons creating a longitudinal Lorentz force that pushes electrons to bunch. If the accelerator is sufficiently long, the electrons within a bunch oscillate in a self-organized (collective) motion under the effect of the undulator, forming microbunches with a periodicity equal to the emitted wavelength λ_{EM}. At this point, their electromagnetic (EM) wave emission is correlated and coherently amplified along the undulator until saturation is reached.

Interestingly, the electromagnetic field adds up in a very efficient way, so that the collective interaction makes the magnitude of the emitted electric field to be proportional to the number of electrons in the bunch N_{e^-}, and thus the peak intensity I_{EM} to $N_{\mathrm{e}^-}^2$ [20, 25] (unlike conventional lasers where the amplification process happens due to population inversion and the intensity is proportional to the number of elements in the active medium). Typically, the number of electrons in a bunch is of the order of 10^9 to 10^{10}, so that the peak intensity can be very large [9]. In fact, when the FEL reaches saturation the number of coherent photons emitted spontaneously by one electron going through the undulator can be as large as 10^3 to 10^4 [9]. Thus, a pulse emitted by an electron bunch can have 10^{11} to 10^{14} x-ray coherent photons.

On the other hand, in the reference frame of electrons (travelling together at $v_z \approx c$) they would be subject to a shorter undulator period corrected by a factor of γ due to the Lorentz contraction, where $\gamma = (1 - v_z^2/c^2)^{-1}$. Since the emitted wavelength corresponds to the periodicity of the undulator λ_u/γ they would shorten their wavelength in the same proportion. Moreover, while the emitted wave train moves along the $z-$direction, on the laboratory reference frame there is an additional Doppler shift to consider with a correction factor $\sim 2\gamma$. The result is that the relativistic and Doppler effects downscale the wavelength to

$$\lambda_{\mathrm{EM}} \approx \frac{\lambda_u}{2\gamma^2} \tag{1.1}$$

Electrons are accelerated to velocities such that the Lorentz factor reaches the value $\gamma \approx 10^3$. Then, following Rel. 1.1 we find that $\lambda_{\mathrm{EM}} \approx 10^{-3}/2 \cdot 10^{-6} = 10^{-9}$ m which corresponds to wavelengths in the x-ray domain [20].

The duration of the emitted pulse can be estimated by taking into account that each electron going through the undulator emits a wave train consisting of a number of wavelengths equal to the number of undulator periods N_u. The pulse duration τ is found to be

$$\tau = \frac{N_u \lambda_{\mathrm{EM}}}{c} \tag{1.2}$$

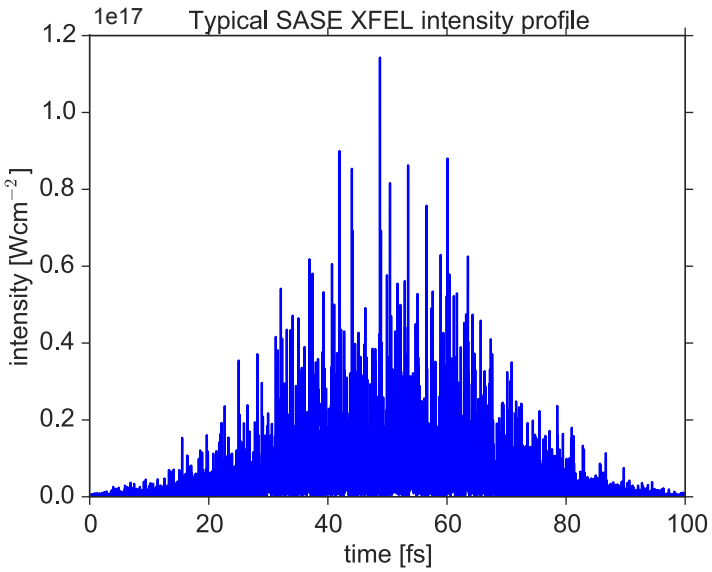

Figure 1.2: Simulated SASE intensity profile. The XFEL pulse has $N_{\text{EM}} = 10^{12}$ photons focused into a circular focal radius of 1.5 μm. The photon wavelength is set to $\lambda_{\text{EM}} = 1.2$ nm (~ 1 KeV), pulse duration to $\tau = 100$ fs, and spectral bandwidth to $\Delta\lambda_{\text{EM}} = 137.7$ nm (~ 9 eV).

Usually in XFEL facilities, the number of undulator periods N_u is of the order of 10^2, so pulse durations are about $\tau \approx 10^2 \cdot 10^{-9}/10^8 = 10^{-15}$ s, i.e, are in femtosecond timescales [20]. The gain bandwidth (or relative spectral bandwidth) σ_ω is given by

$$\sigma_\omega \equiv \frac{\Delta\lambda_{\text{EM}}}{\lambda_{\text{EM}}} = \frac{1}{N_u} \tag{1.3}$$

Accordingly, gain bandwidths are roughly of $\Delta\lambda_{\text{EM}}/\lambda_{\text{EM}} \approx 10^{-2}$ [20]. Electron and photon beam parameters of present-day XFEL facilities may be found in Refs. [26, 21].

1.1.2 Intensity profile of SASE FEL

The x-ray radiation emitted by an electron that is injected in an undulator consists of random radiation noise. The bunching of the electrons and, consequently, the progressive amplification of the EM-field has the effect of smoothing out the temporal distribution of the radiation intensity. This means that the self-amplified spontaneous emission (SASE) spectrum has a very short coherence time with a broadband, noisy spectrum. The photons are said to come in subpulses (or in "spikes"), and the intensity in each of them changes randomly [27, 28] (see Fig 1.2). Besides, the shape of the ra-

diated SASE pulses and the emission spectrum fluctuates from shot to shot, together with shifts of the central wavelength [29, 30].

A numerical approach to simulate a XFEL pulse with a SASE intensity profile, following the scheme proposed by G. Vannucci and M.C. Teich, 1980 [31], can be found in Appendix A.

1.2 Previous work

Understanding the response of individual atoms to intense x-rays is essential for most Free-Electron Laser applications. In contrast to the single-photon absorption at present synchrotron radiation facilities, the interaction of XFEL pulses with matter is rather nonlinear. Namely, for intense x-rays, the dominant interaction mechanism is sequential multi-photon ionization.

Structural biologists, for example, may be concerned by the electronic response in biological samples after the interaction with XFEL radiation, since the induced electronic rearrangement can influence the diffraction pattern [32, 11]. Therefore, optimal laser parameters must be established to reduce the damage in the sample and to prevent its destruction before the diffraction pattern is recorded.

One of the first experiments carried out at LCLS involved neon [33]. In that experiment it was found that, for sufficiently high photon energies (far above the $K1s$-ionization threshold), the XFEL pulse can strip neon from inside out of all its electrons by a sequence of inner-shell photoionization and Auger decay events [33, 34]. At the employed high intensities, the neon atom can even become transparent due to rapid ejection of inner-shell electrons. Photoabsorption was also studied with atomic xenon using as well the LCLS FEL [35]. Here, the striking fact was that just with the absorption of less than ten photons with energies around 1 keV, led to the creation of Xe^{+36}.

The theory behind the observations in neon and xenon was based on a rate equation approach [34, 36], which gave results in very good agreement with experimental data. Certainly, such success of the model -together with further investigations on isolated atoms [37, 38, 39]- forecasted its extension to more complex systems, such as molecules. However, an extension to molecules is challenging, since in addition to photoionization and decay processes, there could be also dissociation of the molecule, and sharing of valence-shell electrons between its constituent atoms. So far, the vast majority of theoretical and experimental studies on absorption of ultra-bright XFEL pulses by molecules were done considering molecular Nitrogen (N_2), due to its relatively simple description [40, 41, 42, 43, 44].

In this thesis we theoretically investigate the electronic structure response in diatomic molecules to the interaction with a high-intensity, ultrafast x-ray pulse. Carbon monoxide (CO) is chosen as the prototypical molecule and only photoionization, fluorescence and Auger decay processes are considered. We make an extension of the problem of a single diatomic molecule blasted by a XFEL beam to the situation where a molecular gas-phase target is considered. Thereby the attenuation of the pulse as it travels along the medium must be taken into account. Furthermore, since pump-probe techniques are widely used in spectroscopic experiments, we study as well the interaction of a molecule with a pump-probe field by considering two temporally overlapping XFEL pulses with different pulse parameters.

The theoretical approach is based on a molecular rate-equation model, which is coupled to the evolution of the intensity distribution of the x-ray pulse. The corresponding equations are solved self-consistently by the `XCO_REQ` program, developed for this thesis.

`XCO_REQ` is a result of a joint collaboration between the Center for Free-Electron Laser Science (CFEL)-DESY Theory Division and the Quantum Optics with X-rays group. The CFEL-DESY Theory Division developed `XMOLECULE` toolkit [45], which calculates the transition rates of all the possible molecular multiple-hole configurations formed during the interaction with the XFEL pulse, builds and solves the molecular rate equations. For the present work, `XCO_REQ` uses the transition rates together with the rate equation code of `XMOLECULE` and stitches it to the propagation of the XFEL pulse following a scheme similar to the one implemented by C. Weninger and N. Rohringer, 2014 in Ref.[46].

1.3 Outline of this thesis

The thesis is organized as follows: in chapter 2, we give a brief introduction to the theory underlying x-rays processes implemented in `XMOLECULE` toolkit [45]. To treat x-ray-molecule interactions, a consistent *ab initio* framework based on nonrelativistic quantum electrodynamics, Hartree-Fock theory and time-dependent perturbation theory is outlined.

Chapter 3 is concerned with the description of electronic dynamics by means of a molecular rate-equation model, which considers all the photoionization and relaxation rates presented in chapter 2. The derivation of the equation that simulates the propagation of the pulse along an absorbing medium within classical electrodynamics is also presented. The chapter ends by explaining how the rate equations and the equation for the evolution of the XFEL beam are solved by `XMOLECULE` and `XCO_REQ`.

In chapter 4, numerical results yielded by `XCO_REQ` assuming a single x-ray pulse are discussed. We consider a XFEL pulse that interacts with a gas of

neutral CO molecules, and analyze its temporal and spatial evolution under the variation of XFEL beam parameters, such as, photon energy, photon fluence and pulse duration. Additionally, we study the transmission of the x-ray pulse as a function of the incoming peak intensity.

Chapter 5 reviews an approach to stimulate x-ray Raman scattering in CO based on a two-color pulse scheme [47]. To study the transmission of the pump and probe pulses as well as the contribution of the created ions to the background signal, we extend the model of chapter 4 to pump-probe experiments. For this, we include an additional equation that propagates the probe field.

Finally, we unify our advances concerning the understanding of high-intensity absorption and multi-photoionization processes in CO in chapter 6.

Chapter 2

Interaction of molecules with XFELs

This chapter is based on the following publications:

Robin Santra.

"PHD Tutorial: Concepts in x-ray physics",

J. Phys. B: At. Mol. Opt. Phys., ***42****, 023001 (2009).*

Yajiang Hao, Ludger Inhester, Kota Hanasaki, Sang-Kil Son and Robin Santra.

"Efficient electronic structure calculation for molecular ionization dynamics at high x-ray intensity",

Structural Dynamics, **2***, 041707 (2015)*

2.1 Introduction

In this chapter we review the theory underlying the interaction of x-rays with matter, particularly with small quantum systems such as atoms and molecules. At this spatial level ($\sim 1\mathring{A} = 10^{-10}$ m) it becomes more convenient to use an adequate set of units to make the theoretical treatment much easier. Therefore throughout this chapter atomic units (abbreviated as [a.u.]) are used [48]. Within atomic units the electron mass m_e, the elementary charge e, the reduced Planck's constant $\hbar \equiv h/2\pi$ and the Coulomb's constant $k_e = 1/(4\pi\varepsilon_0)$ by definition are all unity. The speed of light in vacuum c, adopts another value through the fine structure constant α, namely, $c = 1/\alpha = \hbar c/e^2 \approx 137$.

We also address the question of what are the different x-ray induced processes that are triggered when a diatomic molecule is blasted by a XFEL

beam. For this, we present the theoretical foundations as well as the approximations that are assumed in XMOLECULE toolkit [45].

The chapter is structured as follows. We first introduce in section 2.2 the total Hamiltonian of the radiation-matter system by using nonrelativistic quantum electrodynamics (QED), which comprises the sum of three Hamiltonians: a molecular, an electromagnetic and an interaction Hamiltonian. In section 2.3 and section 2.4, solutions for the electromagnetic and interaction Hamiltonian are presented. With such solutions, in section 2.5 a time-dependent perturbation approach is carried out so that in section 2.6 is applied to derive the expressions for the different transition rates of the x-ray induced processes. Finally, a brief summary of the chapter is drawn in section 2.7.

2.2 The Hamiltonian

Photon energies delivered by XFELs are far below the electron rest energy ($m_e = 511$ keV). This huge difference allows us to neglect relativistic effects (such as spin-orbit coupling, pair production and relativistic structure responses), so that relativistic QED is disregarded [49, 50, 5].

The constituents of molecules are nuclei and electrons. Therefore a complete and accurate theoretical treatment is by far more difficult than in atoms, since nuclei dynamics can come into play and affect electron motion. However for molecules a smart simplification can be done, provided that nuclei are much heavier than electrons (the ratio of the electron mass to the nuclear mass $M_N \geq 938$ MeV is about a thousandth ($m_\mathrm{e}/M_\mathrm{N} \approx 10^{-3}$)). This essentially implies that, although the nuclear vibration period can be of a few femtoseconds (comparable to the duration of a typical XFEL pulse), the amplitud of the oscillation is unmeaningful to affect the electronic response -considered in this thesis- to the XFEL radiation. Consequently, in the following, to decipher the molecular electronic wave function we just focus on electronic interactions by omitting its dependence on the nuclei's position [51].

In the present work we assume that the molecule can only respond to the interaction with the XFEL beam by means of photoionization, fluorescence and Auger decay.

2.2.1 The electromagnetic Hamiltonian

We assume that the electromagnetic field of free-electron lasers can be described by the Maxwell's equations in free space (i.e. in absence of currents

and sources), which in terms of the electric (**E**) and magnetic (**B**) fields, are written as

$$\nabla \cdot \mathbf{B} = 0, \tag{2.1a}$$

$$\nabla \times \mathbf{E} + \alpha \frac{\partial \mathbf{B}}{\partial t} = 0, \tag{2.1b}$$

$$\nabla \cdot \mathbf{E} = 0, \tag{2.1c}$$

$$\nabla \times \mathbf{B} - \alpha \frac{\partial \mathbf{E}}{\partial t} = 0 \tag{2.1d}$$

The zero divergence of **B** and **E** introduces the vector and scalar potentials, **A** and φ, respectively, which relate the former fields via

$$\mathbf{B} = \nabla \times \mathbf{A}, \qquad \mathbf{E} = -\alpha \frac{\partial \mathbf{A}}{\partial t}, \tag{2.2}$$

where we used the fact that there are no sources and therefore **E** is purely transverse ($\varphi = 0$). Additionally, by adopting the Coulomb gauge condition ($\nabla \cdot \mathbf{A} = 0$) and upon substitution of Eq.(2.2) into Eq.(2.1d) one finds that the EM field satisfies the well-known wave equation

$$\nabla^2 \mathbf{A}(\mathbf{r}, t) - \frac{\partial^2 \mathbf{A}}{\partial t^2}(\mathbf{r}, t) = 0, \tag{2.3}$$

which describes the radiation field as plane wave solutions. It follows then that within some volume V the vector potential **A** can be represented as the Fourier expansion over a collection of modes $(\mathbf{k}, \lambda)$, such that

$$\mathbf{A}(\mathbf{r}, t) = \frac{1}{2\sqrt{V}} \sum_{\mathbf{k}} \left(\mathbf{A}_{\mathbf{k}}(t) e^{i\mathbf{k}\cdot\mathbf{r}} + \mathbf{A}_{\mathbf{k}}(t)^* e^{-i\mathbf{k}\cdot\mathbf{r}} \right). \tag{2.4}$$

where $\mathbf{k}$ is the wave vector and $\mathbf{A}^*_{\mathbf{k}} = \mathbf{A}_{-\mathbf{k}}$, since vector potential amplitudes must be real.

Also worth recalling is that the Coulomb gauge implies a transversal nature of the propagating waves, i.e., for any given $\mathbf{k}$ there are two transverse directions. Hence, there is a polarization vector $\hat{\varepsilon}_{\mathbf{k},\lambda}$ with two polarization orientations ($\lambda = 1, 2$). Due to the normalization condition [52], the different polarization vectors $(\mathbf{k}, \lambda)$ are such that

$$\mathbf{k} \cdot \hat{\varepsilon}_{\mathbf{k},\lambda} = 0, \qquad \hat{\varepsilon}^*_{\mathbf{k},1} \cdot \hat{\varepsilon}_{\mathbf{k},2} = 0. \tag{2.5}$$

Each of the time-dependent amplitudes of Eq. (2.4), with angular frequency $\omega_{\mathbf{k}} = |\mathbf{k}|/\alpha$, are represented as

$$\mathbf{A}_{\mathbf{k}}(t) = \sum_{\lambda} A_{\mathbf{k},\lambda} \hat{\varepsilon}_{\mathbf{k},\lambda}(t) e^{-i\omega_{\mathbf{k}} t}. \tag{2.6}$$

Now that we have found the solutions to Maxwell's equations, we determine the EM energy. Under all the previously assumed conditions, the classical energy of the EM field reads

$$H_{\mathrm{EM}} = \frac{1}{8\pi} \int_V d\mathbf{r} \, (|\mathbf{E}|^2 + |\mathbf{B}|^2) \tag{2.7}$$

$$= \frac{1}{8\pi} \int_V d\mathbf{r} \sum_{\mathbf{k},\lambda} \left(\alpha^2 \left| \frac{\partial \mathbf{A}_{\mathbf{k}}}{\partial t} \right|^2 + |\mathbf{k} \times \mathbf{A}_{\mathbf{k}}|^2 \right). \tag{2.8}$$

To quantize the EM field we first consider that the components of $\mathbf{A}$ correspond to the generalized coordinates, i.e., $\mathbf{q}_{\mathbf{k}}(t) = \mathbf{A}_k(t)$. Then after substitution of this last relation into Eq. (2.8) and by defining the canonical momentum as

$$\mathbf{p}_{\mathbf{k}}(t) = -i \frac{\omega_{\mathbf{k}} \alpha^2}{4\pi} \mathbf{A}_{\mathbf{k}}(t), \tag{2.9}$$

the EM Hamiltonian in terms of the canonical coordinates is [53]

$$H_{\mathrm{EM}} = \sum_{\mathbf{k}} \left(\frac{2\pi}{\alpha^2} |\mathbf{p}_{\mathbf{k}}|^2 + \frac{\alpha^2 \omega_{\mathbf{k}}^2}{8\pi} |\mathbf{q}_{\mathbf{k}}|^2 \right). \tag{2.10}$$

From Eq. (2.8) we can read off that every mode is mathematically equivalent to the quantum harmonic oscillator Hamiltonian. This brings us to the idea that the individual oscillation amplitudes $\mathbf{A}_{\mathbf{k},\lambda}$ can be decomposed as well into sums of annihilation $\hat{a}^\dagger_{\mathbf{k},\lambda}$ and creation $\hat{a}_{\mathbf{k},\lambda}$ operators [54] in a way that,

$$A_{\mathbf{k},\lambda} = \sqrt{\frac{4\pi}{\omega_{\mathbf{k}} \alpha^2}} \cdot \frac{1}{\sqrt{2}} (\hat{a}_{\mathbf{k},\lambda} + \hat{a}^\dagger_{-\mathbf{k},\lambda}) \tag{2.11}$$

Here, $\hat{a}^{\dagger}_{\mathbf{k},\lambda}(\hat{a}_{\mathbf{k},\lambda})$ creates (destroys) a photon with energy $\omega_{\mathbf{k}}$ and mode $(\mathbf{k},\lambda)$. Therefore they obey the bosonic conmutation relations

$$[\hat{a}_{\mathbf{k},\lambda},\hat{a}^{\dagger}_{\mathbf{k}',\lambda'}]=\delta_{\mathbf{k},\mathbf{k}'}\delta_{\lambda,\lambda'};\quad [\hat{a}_{\mathbf{k},\lambda},\hat{a}_{\mathbf{k}',\lambda'}]=[\hat{a}^{\dagger}_{\mathbf{k},\lambda},\hat{a}^{\dagger}_{\mathbf{k}',\lambda'}]=0. \tag{2.12}$$

Substitution of Eq.(2.11) into both Eq. (2.6) and Eq. (2.8), takes us to the quantized electromagnetic field

$$\hat{\mathbf{A}}(\mathbf{r})=\sum_{\mathbf{k},\lambda}\sqrt{\frac{2\pi}{V\omega_{\mathbf{k}}\alpha^2}}\left(\hat{a}_{\mathbf{k},\lambda}\hat{\varepsilon}_{\mathbf{k},\lambda}e^{i\mathbf{k}\cdot\mathbf{r}}+\hat{a}^{\dagger}_{\mathbf{k},\lambda}\hat{\varepsilon}^{*}_{\mathbf{k},\lambda}e^{-i\mathbf{k}\cdot\mathbf{r}}\right) \tag{2.13}$$

The time-dependency has been omitted in the last expression, since we want to work in the Schrödinger picture, where time is encoded in the wave function and not in operators. Hence, the corresponding EM Hamiltonian after dropping the zero-point energy is written as [49, 50]

$$\hat{H}_{\text{rad}}=\sum_{\mathbf{k},\lambda}\omega_{\mathbf{k}}\hat{a}^{\dagger}_{\mathbf{k},\lambda}\hat{a}_{\mathbf{k},\lambda}. \tag{2.14}$$

2.2.2 The minimal-coupling Hamiltonian

According to the *Principal of Minimal Coupling* in classical electrodynamics, an electron at position $\mathbf{r}$ in an EM field is described by the Hamiltonian

$$\hat{H}=\frac{1}{2}\left[\hat{\mathbf{p}}-\alpha\hat{\mathbf{A}}(\mathbf{r})\right]^2+q\varphi(\mathbf{r}), \tag{2.15}$$

where $\mathbf{p}=-i\nabla$ is the quantum momentum operator and φ is the Coulomb interaction potential between charged particles

$$\varphi(\mathbf{r})=\sum_{j}\frac{1}{|\mathbf{r}-\mathbf{r}_j|}. \tag{2.16}$$

As it was done with the EM Hamiltonian, it will be favorable for us to express the Hamiltonian of Eq. (2.15) within the second-quantization language since it paves the particle-hole formalism that will be introduced later on [55]. For this, we begin considering the components of the Pauli Spinor $\hat{\psi}$

$$\hat{\psi}(\mathbf{x}) = \begin{pmatrix} \hat{\psi}_{+1/2}(\mathbf{r}) \\ \hat{\psi}_{-1/2}(\mathbf{r}) \end{pmatrix} \tag{2.17}$$

whose operators $\hat{\psi}^\dagger_\sigma(\mathbf{r})$ ($\hat{\psi}_\sigma(\mathbf{r})^\dagger$) create (annihilate) an electron at position $\mathbf{r}$ with spin projection quantum number σ, and satisfy the fermionic relations:

$$[\hat{\psi}_\sigma(\mathbf{r}), \hat{\psi}^\dagger_{\sigma'}(\mathbf{r}')] = \delta_{\sigma,\sigma'}\delta^{(3)}(\mathbf{r}-\mathbf{r}'), \qquad [\hat{\psi}_\sigma(\mathbf{r}), \hat{\psi}_{\sigma'}(\mathbf{r}')] = [\hat{\psi}^\dagger_\sigma(\mathbf{r}), \hat{\psi}^\dagger_{\sigma'}(\mathbf{r}')] = 0. \tag{2.18}$$

It follows that, within second-quantization, by expanding the right-hand side of Eq. (2.15) and imposing again the Coulomb Gauge condition, one finds that the Hamiltonian is made out of the sum of two terms: a molecular Hamiltonian $\hat{H}_{\text{mol}}$, and an interaction Hamiltonian $\hat{H}_{\text{in}}$.

The molecular Hamiltonian is found to be

$$\hat{H}_{\text{mol}} = \hat{T}_{\text{N}} + \hat{V}_{\text{NN}} + \hat{H}_{\text{el}}, \tag{2.19}$$

whose contributions stand for the kinetic energy of the nuclei

$$\hat{T}_N = -\frac{1}{2}\sum_n \frac{\nabla^2_n}{M_n}, \tag{2.20}$$

the nucleus-nucleus repulsion

$$\hat{V}_{NN} = \sum_{n<n'} \frac{Z_n Z_{n'}}{|\mathbf{R}_n - \mathbf{R}_{n'}|} \tag{2.21}$$

$$, \tag{2.22}$$

and the electronic Hamiltonian

$$\begin{aligned} \hat{H}_{\text{el}} &= \int d\mathbf{r}\ \hat{\psi}^\dagger(\mathbf{r})\left[-\frac{1}{2}\nabla^2 - \sum_n \frac{Z_n}{|\mathbf{r}-\mathbf{R}_n|}\right]\hat{\psi}(\mathbf{r}) \\ &+ \frac{1}{2}\int d\mathbf{r}\int \mathbf{r}\hat{\psi}^\dagger(\mathbf{r})\hat{\psi}^\dagger(\mathbf{r}')\frac{1}{|\mathbf{r}-\mathbf{r}'|}\hat{\psi}(\mathbf{r}')\hat{\psi}(\mathbf{r}), \end{aligned} \tag{2.23}$$

where $\mathbf{R}_n, M_n$ and Z_n the position, mass and charge of the nth nucleus, respectively. The Hamiltonian $\hat{H}_{\text{el}}$ involves the contribution of the single-particle operators: the electron kinetic energy and the nuclei-electron interaction. But also the two-particle operator: the electron-electron interaction. The factor $1/2$ in the double integral of Eq. (2.23) is to ensure that each interaction is included once.

On the other hand, the interaction Hamiltonian is given by

$$\hat{H}_{\text{int}} = \alpha \int d\mathbf{r}\ \hat{\psi}^{\dagger}(\mathbf{r}) \left[\hat{\mathbf{A}} \cdot \frac{\nabla}{i} \right] \hat{\psi}(\mathbf{r}) + \frac{\alpha^2}{2} \int d\mathbf{r}\ \hat{\psi}^{\dagger}(\mathbf{r}) \hat{A}^2(\mathbf{r}) \hat{\psi}(\mathbf{r}) \tag{2.24}$$

The first term, $\hat{\mathbf{A}} \cdot \nabla$ describes processes in which one photon is created or annihilated, such as absorption and fluorescence; whereas the second term A^2 leads to the simultaneous destruction and creation of a photon, like one-photon scattering [5, 54, 56].

Hence, altogether Eq.(2.14), (2.19) and (2.24) lead to a total Hamiltonian of matter coupled to the EM field given by

$$\hat{H} = \hat{H}_{\text{EM}} + \hat{H}_{\text{mol}} + \hat{H}_{\text{int}} \tag{2.25}$$

2.3 Solutions of the electromagnetic Hamiltonian

As we introduced in the first chapter, the SASE FEL pulse consists of subpulses. The number of these subpulses and the subpulses durations, amplitudes, and phases fluctuate from shot to shot randomly [57, 58, 59]. In fact, in some cases this spiky nature could play an important role during light-matter interaction [60, 34, 61, 62]. However for the purposes of this thesis, we can assume -to a first approximation- simpler temporal shaped pulses without loosing the essential physics [34].

Based on the above assessments, we consider that the eigenstate of $\hat{H}_{\text{EM}}$ is given by the photon Fock state $|N_{\text{EM}}\rangle$ containing N_{EM} photons in the mode $(\mathbf{k}_{\text{in}}, \lambda_{\text{in}})$ [5], i.e.,

$$\hat{H}_{\text{EM}}|N_{\text{EM}}\rangle = N_{\text{EM}} \cdot \omega_{\text{in}}|N_{\text{EM}}\rangle \qquad \text{with} \qquad \hat{a}^{\dagger}_{\mathbf{k},\lambda}\hat{a}_{\mathbf{k},\lambda}|N_{\text{EM}}\rangle = \delta_{\mathbf{k},\mathbf{k}_{\text{in}}}\delta_{\lambda,\lambda_{\text{in}}} N_{\text{EM}}|N_{\text{EM}}\rangle \tag{2.26}$$

2.4 Molecular electronic structure calculation

2.4.1 n-particle and n-hole states

We consider a molecular system composed of N_{N} nuclei and N_{el} electrons with a closed-shell ground state. Let the $|\Psi_0^{N_{\mathrm{el}}}\rangle$ be the ground state electronic wavefunction, such that, $\hat{H}_{\mathrm{el}}|\Psi_0^{N_{\mathrm{el}}}\rangle = E_0^{N_{\mathrm{el}}}|\Psi_0^{N_{\mathrm{el}}}\rangle$. Within the *mean field* model , $|\Psi_0^{N_{\mathrm{el}}}\rangle$ may be approximated by the total antisymmetric product of spin orbitals -a so called Slater determinant-

$$|\Psi_0^{N\mathrm{el}}\rangle \approx \prod_{i=1}^{N_{\mathrm{el}}} \hat{c}_i^\dagger |0\rangle, \tag{2.27}$$

where the operator $\hat{c}_i^\dagger$ creates the spin-orbital $|\psi_i\rangle$ ($\hat{c}_i^\dagger|0\rangle = |\psi_i\rangle$), given by the product of the position and spin states (the index i comprises both quantum numbers) and

$$[\hat{c}_i, \hat{c}_j^\dagger] = \delta_{i,j}; \quad [\hat{c}_i, \hat{c}_j] = [\hat{c}_i^\dagger, \hat{c}_j^\dagger] = 0. \tag{2.28}$$

With an analogous reasoning, a *one-hole* state can be defined through the annihilation operator as

$$|\Psi_i^{N\mathrm{el}-1}\rangle \equiv \hat{c}_i |\Psi_0^{N_{\mathrm{el}}}\rangle \tag{2.29}$$

The set of spin orbitals $\{|\psi_i\rangle\}$ with orbital energies ε_i forms the eigenbasis of the electronic one-body Hamiltonian $\hat{F}$ (which in our case will correspond to the Hartree-Fock Hamiltonian). In fact, $\hat{F}$ satisfies the eigenvalue equation

$$\hat{F}|\psi_i\rangle = \varepsilon_i |\psi_i\rangle \tag{2.30}$$

Then according to Koopman's theorem and provided that Eq. (2.27) is being assumed [48], the orbital energy ε_i associated with the spin orbital $|\psi_i\rangle$ is such that

$$E_0^{N_{\mathrm{el}}} - E_i^{N_{\mathrm{el}}-1} = \langle \Psi_0^{N_{\mathrm{el}}} | \hat{H}_{\mathrm{el}} | \Psi_0^{N_{\mathrm{el}}} \rangle - \langle \Psi_i^{N_{\mathrm{el}}-1} | \hat{H}_{\mathrm{el}} | \Psi_i^{N_{\mathrm{el}}-1} \rangle = \varepsilon_i \tag{2.31}$$

i.e., equals the difference between the energy of the neutral groundstate and the excited ionic state. Furthermore, from Eq. (2.29), we can construct *singly*

excited N_{el}-Slater determinant by adding to $|\Psi_i^{N_{\text{el}}-1}\rangle$ an electron in an initially unoccupied virtual orbital $|\psi_a\rangle$ (virtual orbitals are symbolized by $a, b, c, d...$ and refer to states in the continuum)

$$|\Psi_i^a\rangle \equiv \hat{c}_a^\dagger \hat{c}_i |\Psi_0^{N_{\text{el}}}\rangle, \tag{2.32}$$

and thus, in the same fashion, a basis in Fock space may be built by arbitrary n-particle-n-hole excitation classes $|\Psi_{i_1,i_2,...,i_N}^{a_1,a_2,...,a_N}\rangle$. Moreover, with these assumptions, the set of spin orbitals derived from Eq. (2.30) for a specific electronic state *approximately* describe also electronic states where *few* electrons have been added (removed).

To finish off, we would like to remark that the connection between the Pauli Spinors $\hat{\psi}(\mathbf{r})$ and $\hat{\psi}^\dagger(\mathbf{r})$ (Eq. (2.17)) and the set of spin orbitals $\{|\psi_i\rangle\}$ lies through the expansion of the former as [5, 55]

$$\begin{aligned} \hat{\psi}(\mathbf{r}) &= \sum_i \psi_i(\mathbf{r}) \hat{c}_i \\ \hat{\psi}^\dagger(\mathbf{r}) &= \sum_i \psi_i^*(\mathbf{r}) \hat{c}_i^\dagger, \end{aligned} \tag{2.33}$$

The set of Eqs. (2.33) turn to be useful when determining x-ray induced processes.

2.4.2 The Hartree-Fock-Slater Method

We move now onto the application of the Hartree-Fock-Slater method (HFS) for calculating all the (energetic) accessible electronic configurations. With the assumptions presented in section 2.4.1 it is found that $\hat{H}_{\text{el}} \approx \hat{F}$. Actually, in the present case the one body Hamiltonian $\hat{F}$ corresponds to the Hartree-Fock-Slater operator, so that the associated effective single-electron Schrödinger equation for the molecular orbital (MO) $|\psi_i\rangle$ reads [45]

$$\left[\frac{-1}{2}\nabla^2 + V_{\text{eff}(\mathbf{r})}\right]\psi_i(\mathbf{r}) = \varepsilon_i \psi_i(\mathbf{r}) \tag{2.34}$$

and

$$V_{\text{eff}}(\mathbf{r}) = -\sum_A \frac{Z_A}{|\mathbf{r} - \mathbf{R}_A|} + \int d\mathbf{r} \frac{\rho(\mathbf{r}')}{|\mathbf{r} - \mathbf{r}'|} + V_X(\mathbf{r}) \tag{2.35}$$

The three terms of the effective potential V_{eff} can be interpreted as follows: the first is the nuclear Coulomb potential -where the nuclear charge and coordinates are denoted by Z_A and $\mathbf{R}_A$, respectively-.The second comes from the electron-electron interaction with electronic density $\rho(\mathbf{r})$. The third term V_X is the *exchange term* and is approximated by the Slater exchange potential [63],

$$V_{\text{X}}(\mathbf{r}) = -\frac{3}{2}\left[\frac{3}{\pi}\rho(\mathbf{r})\right]^{1/3} \tag{2.36}$$

The electronic density $\rho(\mathbf{r})$ is the sum of squared MO's weighted by the occupation numbers $\hat{c}_i\hat{c}_i^\dagger = n_i \in \{0,1,2\}$; or expressly,

$$\rho(\mathbf{r}) = \sum_{i,j}\langle\psi_i|c_i^\dagger c_j|\psi_i\rangle = \sum_i n_i|\psi_i(\mathbf{r})|^2 \tag{2.37}$$

and subject to the restriction

$$\int d\mathbf{r}\ \rho(\mathbf{r}) = N_{\text{el}} \tag{2.38}$$

With the above expressions, we find that the expectation value of the Hamiltonian is the total energy, which is given by the sum of the nucleus-nucleus repulsion energy and the electronic energy [45].

$$E_{\text{total}} = \sum_{A<B}\frac{Z_A Z_B}{|\mathbf{R}_A - \mathbf{R}_B|} + \sum_i n_i\varepsilon_i - \frac{1}{2}\int d\mathbf{r}\int d\mathbf{r}'\frac{\rho(\mathbf{r})\rho(\mathbf{r}')}{|\mathbf{r}-\mathbf{r}'|} + \frac{3}{8}\left(\frac{3}{\pi}\right)^{1/3}\int d\mathbf{r}\rho(\mathbf{r})^{4/3} \tag{2.39}$$

Now, in order to solve Schrödinger's equation (Eq. (2.34)) and thereby to determine the set of molecular orbitals, we suppose that each MO is a linear combination of atomic orbitals (LCAO), i.e.,

$$\psi_i(\mathbf{r}) := \sum_{\mu}^{N_{\text{basis}}} C_{\mu i}\ \varphi_\mu(\mathbf{r}), \tag{2.40}$$

where $C_{\mu i}$ is the coefficient of the μth atomic orbital (AO) for the ith MO. At the same time, each AO is a single basis function and is member of a *minimal* basis set. For chemical elements from B to Ne, $N_{\text{basis}} = 5$ the basis functions are:
$\varphi_{1s} = \varphi_{100}; \varphi_{2s} = \varphi_{200}; \varphi_{2p_x} = (\varphi_{211} + \varphi_{21-1})/\sqrt{2}; \varphi_{2p_y} = (\varphi_{211} - \varphi_{21-1})/(i\sqrt{2})$

and $\varphi_{2p_z} = \varphi_{210}$ [45]. An atomic function $\varphi_\mu(\mathbf{r})$ for a given $\mu \equiv (n, l, m)$ is represented with a radial wave function $u_\mu(r)$ and spherical harmonics as

$$\varphi_{nlm}(\mathbf{r}) = \frac{u_{nl}(r)}{r} Y_{lm}(\theta, \varphi), \tag{2.41}$$

Using the LCAO scheme with the constraint $\langle \psi_i | \psi_j \rangle = \delta_{i,j}$ transforms Eq. (2.34) into the Roothaan-Hall equation [64]. In this *ab initio* framework, providing a first guess for the set of AOs, the coefficients $C_{\mu i}$ are obtained by solving self-consistently the Roothaan-Hall equation.

2.5 Time-dependent perturbation Theory

Certainly, it is $\hat{H}_{\text{int}}$ what permits the study of the various processes that can take place within photon-matter interaction, i.e., the transition probabilities from some initial state $|I\rangle$ to another final state $|F\rangle$. In pursuance of the determination of this quantity, the interaction Hamiltonian may be treated as a perturbation term and $|I\rangle$, just like $|F\rangle$, as eigenstates of the unperturbed Hamiltonian [65]

$$\hat{H}_0 \equiv \hat{H}_{\text{EM}} + \hat{H}_{\text{mol}}, \tag{2.42}$$

The solutions to the total Hamiltonian $\hat{H} = \hat{H}_0 + \hat{H}_{\text{int}}$ -and thereby the calculation of the transition rates- are commonly found using the interaction picture (or Dirac representation) of quantum mechanics [66, 67]. In the interaction picture -where both observables and wave function depend on time- the state vector is represented by

$$|\Psi, t\rangle_{\text{int}} = e^{i\hat{H}_0 t} |\Psi, t\rangle, \tag{2.43}$$

and satisfies the equation of motion

$$i\frac{\partial}{\partial t} |\Psi, t\rangle_{\text{int}} = e^{i\hat{H}_0 t} \hat{H}_{\text{in}} e^{-i\hat{H}_0 t} |\Psi, t\rangle_{\text{int}}, \tag{2.44}$$

where the ket $|\Psi, t\rangle$ stands for the wave function in the Schrödinger picture.

Within the interaction picture by accepting that before the interaction starts ($t \to -\infty$) the molecule-photon system is found in the pure state $|I\rangle =$

$\lim_{t\to\infty}|\Psi,t\rangle_{\rm int}$ and that after a long time ($t\to+\infty$) falls into the orthogonal state $|F\rangle$, the corresponding transition rate, in agreement with Fermi's golden rule and to a first-order approximation [56], is found to be

$$\Gamma_{I\to F} \approx 2\pi\delta(E_F-E_I)|\langle F|\hat{H}_{\rm int}|I\rangle|^2, \tag{2.45}$$

where E_I and E_F are the energies of the initial state and final state, respectively.

To study some of the processes induced by $\hat{H}_{\rm int}$ in Eq. (2.45), we will assume that the eigenstates $|I\rangle$ and $|F\rangle$ consist of a product of a photon Fock state and a electronic wave function, for example,

$$|I\rangle = |\Psi_0^{N\rm el}\rangle|N_{\rm EM}\rangle \quad \text{and} \quad |F\rangle = |\Psi_i^a\rangle|N'_{\rm EM}\rangle \tag{2.46}$$

thus $E_I = E_0^{N_{\rm el}} + N_{\rm EM}\cdot\omega_{\rm in}$ and $E_F = \varepsilon_a + E_i^{N'_{\rm el}} + N'_{\rm EM}\cdot\omega_{\rm in}$ for arbitrary number of electrons $N_{\rm el}, N'_{\rm el}$ and photons $N_{\rm EM}, N'_{\rm EM}$. The quantity ε_a denotes the energy of the virtual orbital (continuum state).

2.6 Photoionization and relaxation processes

In this section we present some processes induced by the interaction of x-rays with matter [L. Inhester et. al., 2016 (manuscript in preparation)].

2.6.1 Photoionization

Photoionization is understood as the process where an atom or a molecule absorbs a photon and the photon energy is transferred to a bounded electron, ejecting the electron out from the partner particle. In other words it promotes the annihilation of a photon with energy $\omega_{\rm in}$ and of an electron from an ith MO, while a continuum state -labeled by a- is created. The initial and final state then should be evaluated in $\Gamma_{I\to F}$ (Eq.(2.45)) as

$$|I\rangle = |\Psi_0^{N_{\rm el}}\rangle|N_{\rm EM}\rangle \tag{2.47}$$

$$|F\rangle = |\Psi_i^a\rangle|N_{\rm EM}-1\rangle = \hat{c}_a^\dagger\hat{c}_i|\Psi_0^{N_{\rm el}}\rangle|N_{\rm EM}-1\rangle \tag{2.48}$$

It follows that the photoionization rate reads

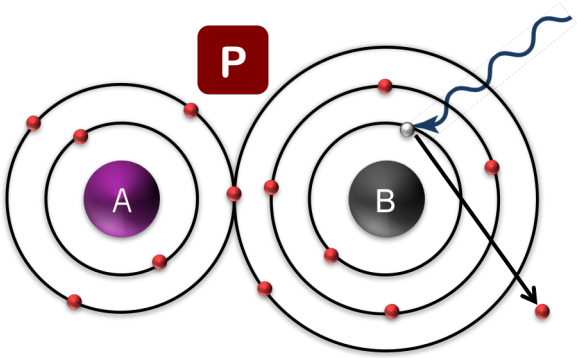

Figure 2.1: Photoionization. The molecule-radiation system is initially defined by the state $|I\rangle = |\Psi_0^{N_{\text{el}}}\rangle|N_{\text{EM}}\rangle$. A photon is absorbed by an electron in the ith MO and the electron is ejected into the continuum. The final state is $|F\rangle = \hat{c}_a^\dagger \hat{c}_i |\Psi_0^{N_{\text{el}}}\rangle|N_{\text{EM}} - 1\rangle$.

$$\begin{aligned}
\Gamma_j^a &= 2\pi\delta(\varepsilon_a - \varepsilon_i - \omega_{\text{in}}) \\
&\times \left| \langle \Psi_i^a | \langle N_{\text{EM}} - 1 | \alpha \int d\mathbf{r}\, \hat{\psi}^\dagger(\mathbf{r}) \hat{\mathbf{A}}(\mathbf{r}) \cdot \frac{\nabla}{i} \hat{\psi}(\mathbf{r}) | \Psi_0^{N_{\text{el}}} \rangle | N_{\text{EM}} \rangle \right|^2 \\
&= \frac{4\pi^2}{\omega_{\text{in}}} \alpha \cdot j_{\text{EM}} \cdot \delta(\varepsilon_a - \varepsilon_i - \omega_{\text{in}}) \\
&\times \left| \sum_{p,q} \langle \psi_p | e^{i\mathbf{k}_{\text{in}} \cdot \mathbf{r}} \hat{\varepsilon}_{\mathbf{k}_{\text{in}}, \lambda_{\text{in}}} \cdot \frac{\nabla}{i} | \psi_q \rangle \langle \Psi_0^{N_{\text{el}}} | \hat{c}_a^\dagger \hat{c}_i \hat{c}_p^\dagger \hat{c}_q | \Psi_0^{N_{\text{el}}} \rangle \right|^2
\end{aligned} \tag{2.49}$$

where the x-ray photon flux has been defined as

$$j_{\text{EM}} = \frac{1}{\alpha} \frac{N_{\text{EM}}}{V} \tag{2.50}$$

Following orthogonality conditions and using the fact that the rate is given by the product between the photon flux and the photoionization cross section, i.e, $\Gamma_i^a = \sigma_i^a(\omega_{\text{in}}) \cdot j_{\text{EM}}$, we find

$$\begin{aligned}
\sigma_i^a(\omega_{\text{in}}) &= \frac{4\pi^2}{\omega_{\text{in}}} \alpha \delta(\varepsilon_a - \varepsilon_i - \omega_{\text{in}}) \\
&\times \left| \langle \psi_a | e^{i\mathbf{k}_{\text{in}} \cdot \mathbf{r}} \hat{\varepsilon} \cdot \frac{\nabla}{i} | \psi_i \rangle \right|^2,
\end{aligned} \tag{2.51}$$

Although the spatial extension of a molecule could be comparable to the XFEL's accessible photon wavelengths [21], the dominant interaction with x-rays is from core electrons which are localized in regions much smaller than these wavelengths. Under such assumption, the electric dipole approximation [1] ($e^{i\mathbf{k}_{\text{in}}\cdot\mathbf{r}} \approx 1$) can be taken as valid [50, 49]. Moreover, since the Hartree-Fock-Slater operator $\hat{F}$ associated with Eq. (2.34) is local, we can make use of the length gauge ($[\mathbf{r}, \hat{F}] = \nabla$); which yields the expression

$$\langle\psi_a|\hat{\varepsilon}\cdot\frac{\nabla}{i}|\psi_i\rangle = i(\varepsilon_a - \varepsilon_i)\langle\psi_a|\hat{\varepsilon}\cdot\mathbf{r}|\psi_i\rangle \tag{2.52}$$

Plugging Eq. (2.40) into Eq. (2.51) and using the squared sum relation $(\sum_i a_i)^2 = \sum_i a_i^2 + 2\sum_{i<j} a_i a_j$, we obtain

$$\begin{aligned}\sigma_i^a(\omega_{\text{in}}) &= \frac{4\pi^2}{\omega_{\text{in}}}\alpha\cdot(\varepsilon_a - \varepsilon_i)^2\delta(\varepsilon_a - \varepsilon_i - \omega_{\text{in}}) \\ &\times \Bigg[\sum_\mu C_{\mu i}^2|\langle\psi_a|\hat{\varepsilon}\cdot\mathbf{r}|\varphi_\mu\rangle|^2 \\ &+ 2\sum_{\mu<\nu} C_{\mu i}C_{\nu i}\langle\psi_a|\hat{\varepsilon}\cdot\mathbf{r}|\varphi_\mu\rangle\langle\psi_a|\hat{\varepsilon}\cdot\mathbf{r}|\varphi_\nu\rangle\Bigg],\end{aligned} \tag{2.53}$$

Given the fact that inner shell photoelectrons are supposed to be well-localized; we adopt the *independent atom approximation* [68, 69]. Here, a molecular continuum state has to be an atomic continuum state of the Ath atom from where it was stripped out,i.e.,$|\psi_a\rangle = |\varphi_a^A\rangle$. In this way, σ_i^a is the contribution of each atomic cross section $(\sigma_i^a)^A$. Performing the average over all the possible molecular orientations (assuming that the incoming pulse has an arbitrary but predetermined polarization with respect to the molecule) the contribution to the cross section of the Ath atom is given by

[1] For this work we use the electric dipole approximation, however in the hard X-ray range it is not longer valid.

$$
\begin{aligned}
(\sigma_i^a(\omega_{\text{in}}))^A &= \frac{4\pi^2}{3\omega_{\text{in}}}\alpha\cdot(\varepsilon_a-\varepsilon_i)^2\delta(\varepsilon_a-\varepsilon_i-\omega_{\text{in}}) \\
&\times \sum_{\beta=1}^{3}\Bigg[\sum_{\mu\in A} C_{\mu i}^2|\langle\varphi_a^A|x_\beta|\varphi_\mu\rangle|^2 \\
&+ 2\sum_{\substack{\mu<\nu\\ \in A}} C_{\mu i}C_{\nu i}\langle\varphi_{a,lm}^A|x_\beta|\varphi_\mu\rangle\langle\varphi_{a,lm}^A|x_\beta|\varphi_\nu\rangle\Bigg],
\end{aligned}
\tag{2.54}
$$

where x_β, with β from 1 to 3, refers to the three-dimensional space coordinates $\{x,y,z\}$, respectively; and the sums over μ and ν only run over the atom A.

At this point, it is useful to sum over all the possible continuum channels, which yields

$$
\begin{aligned}
\sigma_i^A(\omega_{\text{in}}) = \sum_a(\sigma_i^a(\omega_{\text{in}}))^A &= \frac{4\pi^2}{3}\alpha\omega_{\text{in}}\sum_{l,m}\sum_{\beta=1}^{3}\Bigg[\sum_{\mu\in A} C_{\mu i}^2|\langle\varphi_{\varepsilon_{\mathbf{k}},lm}^A|x_\beta|\varphi_\mu\rangle|^2 \\
&+ 2\sum_{\substack{\mu<\nu\\ \in A}} C_{\mu i}C_{\nu i}\langle\varphi_{\varepsilon_{\mathbf{k}},lm}^A|x_\beta|\varphi_\mu\rangle\langle\varphi_{\varepsilon_{\mathbf{k}},lm}^A|x_\beta|\varphi_\nu\rangle\Bigg],
\end{aligned}
\tag{2.55}
$$

where $|\varphi_{\varepsilon_{\mathbf{k}}}^A\rangle$ is the energy normalized wave function of a photoelectron from the atom A with wave vector $\mathbf{k}$ and energy

$$
\varepsilon_{\mathbf{k}} = \varepsilon_i + \omega_{\text{in}} \tag{2.56}
$$

Hence, the rate for photoionizing an electron from the ith-MO is

$$
\Gamma_i = j_{\text{EM}}\cdot\sigma_i(\omega_{\text{in}}) \quad \text{with} \quad \sigma_i(\omega_{\text{in}}) = \sum_A \sigma_i^A(\omega_{\text{in}}) \tag{2.57}
$$

2.6.2 Fluorescence

Fluorescence is the emission of a photon due to the existence of a hole in an inner-shell. Let initially the ith MO to have a hole. After a fluorescence

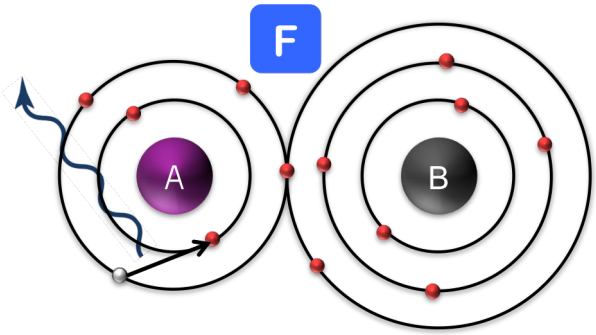

Figure 2.2: Fluorescence. The molecule-radiation system is initially defined by the state $|I\rangle = \hat{c}_i|\Psi_0^{N_{el}}\rangle|0\rangle$,i.e. there is a hole situated in the ith-MO. After a decay lifetime an electron from the upper i'th MO falls onto the lower orbital i. In the process a photon is emitted and the final state is $|F\rangle = \hat{c}_{i'}^{\dagger}|\Psi_0^{N_{el}}\rangle\hat{a}_{\mathbf{k}_F,\lambda_F}^{\dagger}|0\rangle$.

decay time, an electron from the upper i'th MO jumps down to the ith MO, emitting a photon in the process with an energy given by the orbital energy difference [5], i.e.,

$$\omega_F = \varepsilon_{i'} - \varepsilon_i \tag{2.58}$$

The initial state $|I\rangle$ and final state $|F\rangle$ that determines the transition rate $\Gamma_{i\to i'}$ from a hole in the ith MO into the i'th MO are

$$|I\rangle = \hat{c}_i|\Psi_0^{N_{el}}\rangle|0\rangle \tag{2.59}$$
$$|F\rangle = \hat{c}_{i'}|\Psi_0^{N_{el}}\rangle\hat{a}_{\mathbf{k}F,\lambda_F}^{\dagger}|0\rangle \tag{2.60}$$

where $(\mathbf{k}_F, \lambda_F)$ is the x-ray fluorescence mode of interest. The calculation of the rate is analogous as how it was with photoionization. So, by making use of the electric dipole approximation, the length gauge and by integrating over all the possible fluorescence photon energies, the transition rate is given by

$$\begin{aligned}\Gamma_{i\to i'} &= \sum_{\lambda_F}\frac{V}{2\pi^3}\int d\Omega_F\int_0^{\infty} dk_F k_F^2\Gamma_{fi}\\ &= \frac{\alpha^3}{2\pi}\omega_F^3\sum_{\lambda_f}\int d\Omega_F|\langle\psi_i|\hat{\varepsilon}^*_{\mathbf{k}_F,\lambda_F}\cdot\mathbf{r}|\psi_{i'}\rangle|^2\end{aligned} \tag{2.61}$$

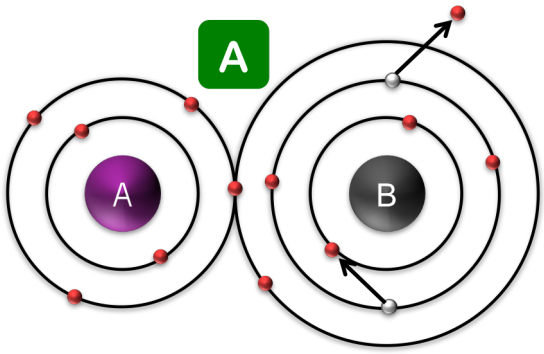

Figure 2.3: Auger decay. The molecule is characterized by the single-hole state $|I\rangle = \hat{c}_i|\Psi_0^{N_{\text{el}}}\rangle$. After a decay lifetime, an electron from an upper orbital j refills the hole and is accompanied by the ejection of an electron from the orbital j'. The final state is $|F\rangle = \hat{c}_a^\dagger \hat{c}_{j'} \hat{c}_j |\Psi_0^{N_{\text{el}}}\rangle$.

Employing the LCAO scheme and averaging over all possible molecular orientations with respect to the polarization of the EM field, the fluorescence rate is found to be

$$\Gamma_{i\to i'} = \frac{4(\alpha\omega_{\text{F}})^3}{3} \sum_{\beta=1}^{3} |\langle \psi_i | x_\beta | \psi_{i'} \rangle|^2 \tag{2.62}$$

2.6.3 Auger decay

The derivation of the Auger decay rate differs from the derivation of the photoionization and fluorescence decay rates. Whereas photoionization and fluorescence are processes induced by H_{int}, Auger decay happens due to interaction between charges. In fact, the original electronic Hamiltonian $\hat{H}_{\text{el}}$ can be splitted up in two terms: a bound and an unbound electronic part. The bound term corresponds to the single-particle operator $\hat{F}$ from the Hartree-Fock Theory (sec. 2.4.2) and the unbounded (usually treated as a perturbation) term is a two-body operator:

$$\hat{H}_{\text{el-int}} = \frac{1}{2} \sum_{pqrs} v_{pqrs} \hat{c}_p^\dagger \hat{q}^\dagger \hat{c}_s \hat{c}_r - \sum_{pq} \sum_i \{v_{piqi} - v_{piiq}\} \hat{c}_p^\dagger \hat{c}_q, \tag{2.63}$$

The Hamiltonian $\hat{H}_{\text{el-int}}$ mediates the Coulomb interaction between two particles and Auger decay is one of its induced processes.

Auger decay involves two electrons that are removed from occupied MOs jth and j'th. One of them fills a lower energetic hole orbital ith, and the other

is ejected into the continuum $|\psi_a\rangle$. Thus, the initial state and final state that drive this process are

$$|I\rangle = \hat{c}_i|\Psi_0^{N_{\text{el}}}\rangle \tag{2.64}$$
$$|F\rangle = \hat{c}_a^\dagger \hat{c}_{j'} \hat{c}_j|\Psi_0^{N_{\text{el}}}\rangle \tag{2.65}$$

Substitution of the initial and final states into $\Gamma_{I\to F} = 2\pi\delta(E_F - E_I)|\langle F|\hat{H}_{\text{el-int}}|I\rangle|^2$ yields [5]

$$\Gamma_{i\to jj'} = \pi \sum_a \left|\langle\psi_a\psi_i|\psi_j\psi_{j'}\rangle + \langle\psi_a\psi_i|\psi_{j'}\psi_j\rangle\right|^2 \delta(\varepsilon_a - \varepsilon_j - \varepsilon_{j'} + \varepsilon_i), \tag{2.66}$$

is the decay rate for the singlet final states with $j \neq j'$.

We base the calculation of this rate on the so-called *one-center approximation* [70, 71, 72]. Within this approximation, the Auger decay can be largely understood as an intra-atomic process that only associates electronic wave functions close to the atom A where initially the hole was. Because the Auger decay rate requires an effortful evaluation of two electron integrals given by

$$\langle\psi_p\psi_q|\psi_r\psi_s\rangle \equiv \int d\mathbf{x} \int d\mathbf{x}' \psi_p(\mathbf{x})\psi_q(\mathbf{x}') \frac{1}{|\mathbf{x} - \mathbf{x}'|} \psi_r(\mathbf{x})\psi_s(\mathbf{x}'), \tag{2.67}$$

the continuum molecular states are approximated as atomic continuum states of atom A and the two-electron integrals go over into

$$\langle\psi_p\psi_q|\psi_r\psi_s\rangle \approx \sum_{\substack{\mu,\nu,\lambda \\ \in A}} C_{\mu q} C_{\nu r} C_{\lambda s} \langle\varphi_p\varphi_q|\varphi_r\varphi_s\rangle \tag{2.68}$$

Substitution of this last expression into Eq.(2.69) and upon summation over all the different transition channels (cf. Eq.(2.55)), it follows that the Auger decay rate reads as

$$\Gamma_{i\to jj'} = \pi \sum_{l,m} \left| \sum_{\substack{\mu,\nu,\lambda \\ \in A}} C_{\mu i} C_{\nu j} C_{\lambda j'} \left(\langle \varphi^A_{\varepsilon_{\mathbf{k}},lm} \varphi_i | \varphi_j \varphi_{j'} \rangle + \langle \varphi^A_{\varepsilon_{\mathbf{k}},lm} \varphi_i | \varphi_{j'} \varphi_j \rangle \right) \right|^2 , \tag{2.69}$$

where

$$\varepsilon_{\mathbf{k}} = \varepsilon_j + \varepsilon_{j'} - \varepsilon_i, \tag{2.70}$$

is the Auger-electron energy.

The calculation of the AOs is carried out numerically by `XATOM` toolkit [73], whose methodology and results have been widely explained and tested in multiple-hole configuration formed during x-ray multiphoton ionization dynamics [39, 35]. After having obtained the set of AOs, `XMOLECULE` toolkit [45] calculates the coefficients $C_{\mu j}$ through the Roothaan-Hall equation [64] (see section 2.4.2) and therewith the transition rates given in the current section.

For this work, calculated rates and cross sections were taken from a table generated with the `XMOLECULE` toolkit. The calculations of the rates were performed by L. Inhester.

2.7 Summary

In this chapter we reviewed the theory that describes the interaction of x-rays with matter. First we presented the total Hamiltonian, which is a contribution of the radiation Hamiltonian, the molecular Hamiltonian and the interaction Hamiltonian.

We assumed that the eigenstates of the radiation Hamiltonian are photon Fock states. The molecular Hamiltonian was splitted into a nuclear Hamiltonian and an electronic Hamiltonian, with the latter being approximated by the Hartree-Fock-Slater (HFS) operator. The solutions to the HFS operator are molecular orbitals, which at the same time are assumed to be a linear combination of atomic orbitals.

The approximate solutions to the molecular and radiation Hamiltonians are calculated by `XMOLECULE` toolkit [45], with which a time-dependent theory approach can be adopted to derive the transition rates for photoionization,fluorescence and Auger decay.

The transitions rates introduced in this chapter are important to understand the set of equations that are capable of temporally tracking the electronic

damage dynamics -so called rate equations- that the molecule experiences during the interaction with the XFEL pulse.

Chapter 3

Absorption model for diatomic molecules

3.1 Introduction

We know that a molecule can experience photoionization, Auger decay, and fluorescence decay. A molecule under the influence of a XFEL beam typically interacts several times with the x-ray pulse, by a sequence of multiple photoionization events [34, 33, 74]. But at the same time the x-ray pulse is being absorbed, since it propagates along the medium. So the absorption of the pulse will be influenced by the electronic dynamics and vice versa. In order to account for both we solve a system of rate equations -which is a multi-step mechanism able to track x-ray induced dynamics- coupled to the evolution of the photon flux.

In this chapter an absorption model for describing the interaction of a focused XFEL beam with a molecular gas-phase target is presented. It is organized as follows: In section 3.2 we construct a rate equation model, which simulates the ionization dynamics induced by the radiation-matter interaction. Then, in section 3.3 we derive the equation that accounts for the absorption of the pulse. At the end of the chapter, section 3.4, numerical details used for simulations are pointed out.

3.2 Rate Equations for ionization and relaxation dynamics

Let us recall that the molecular system under consideration consists of N_{N} nuclei and N_{el} electrons. Let the Ath nuclear charge be denoted as Z_A. Then the molecular charge state $+q$ is given by $q = \sum_A Z_A - N_{\mathrm{el}}$. Furthermore, let us assume a gas of density n_0 contained in a medium of length L.

We suppose that the incoming XFEL beam has a flat, cylindrical focus profile, with an uniform intensity distribution inside the circular transverse section. What is more, unfocused x-ray pulses provided by FELs have angular beam divergences of the order 10^{-5} radians [26]. This implies that for our purposes the incoming x-ray pulse propagates in a single direction, which is chosen as positive $\hat{z}$ direction.

The probability to find the molecule in the state $|\Psi_r^{+q}\rangle$ is given by $P_r^{+q} \equiv \langle\Psi_r^{+q}|\Psi_r^{+q}\rangle$. The number r denotes the electronic configuration of the charge state $+q$, and is a composite index standing for the quantum numbers (see section 2.4.2). In order to calculate $P_r^{+q}(z,t)$ for $z \in [0,L]$ and $t > 0$ we need to keep track of all the possible pathways that can bring the molecule up to the state $|\Psi_r^{+q}\rangle$, in terms of gain transitions and loss transitions. This can be done by means of coupled rate equations [34, 39, 35, 75, 38, 44] which determine the occupation probability distribution at any time $t > 0$. By labeling the molecular electronic state $|\Psi_r^{+q}\rangle$ simply as $|n\rangle$ with $n = 0, 1, 2, ..., N_{\text{config}}$ ($|n = 0\rangle$ denotes the ground state), the rate of change of the populations can be formulated as:

$$\dot{P}_n(z,t) = \sum_{n' \neq n}^{N_{\text{config}}} \left[P_{n'}(z,t)\Gamma_{n' \to n} - \Gamma_{n \to n'} P_n(z,t) \right] \tag{3.1}$$

Before the pulse interacts with the molecular gas, each molecule of the gas is assumed to be in its neutral ground state. In addition, we assume that the total number of molecules along the medium is always conserved. Therefore, to solve Eq. (3.1) the following conditions must be satisfied:

$$P_n(t \to -\infty, z) = \delta_{n0} \qquad \text{and} \qquad \sum_{n}^{N_{\text{config}}} P_n(z,t) = 1 \tag{3.2}$$

The sum of the right side goes over all the set of energetically accessible configurations N_{config} (particular of each molecule). The transition rate $\Gamma_{n \to n'}$ from an initial state $|n\rangle$ to a final state $|n'\rangle$ can be Auger decay, fluorescence decay, inner-shell or valence-shell photoinization, labeled by "A","F", "P" and "V", respectively. It is worth to say, that the only spatial-temporal-dependent rate is the photoionization rate given by $\Gamma_{n \to n'}^{\{P,V\}}(z,t) = \sigma_{n \to n'} j(z,t)$ and $j(z,t)$ stands for the photon flux.

To have a clearer idea of the physics behind Eq. (3.1) lets see how rate equations are built-up. Photoionization of the ground state $|\Psi_0\rangle$ turns the molecule into the state $|\Psi_r^{+1}\rangle$. This state can be again depleted by photoionization (cross section $\sigma_{r \to s}$), undergoing Auger decay (decay rate $\Gamma_{r \to t}^{A}$) or

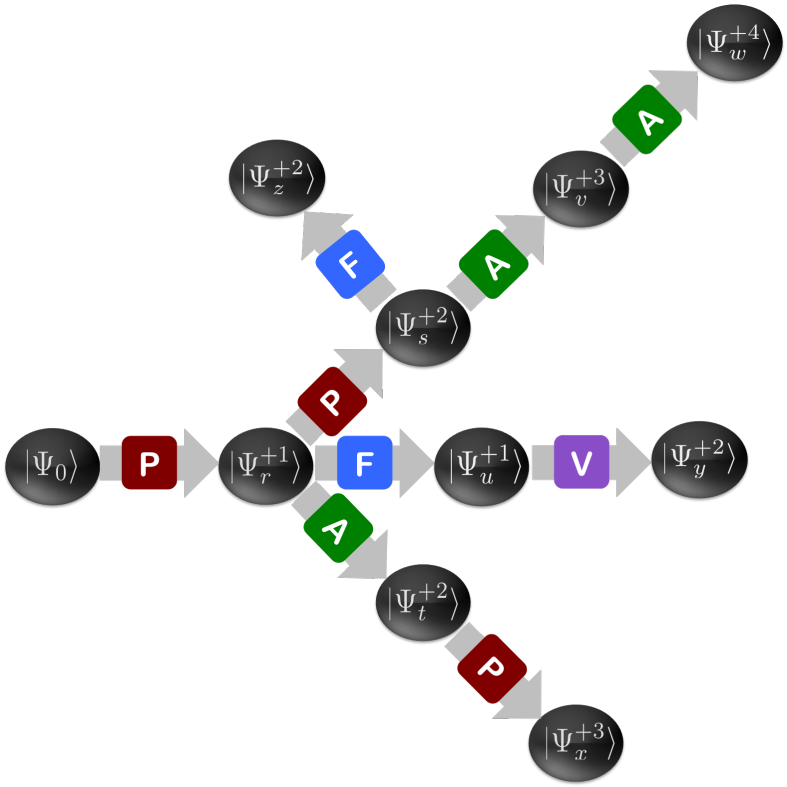

Figure 3.1: Schematic representation of the rate-equation model. The processes displayed are single inner-shell photoionization "P", valence-shell photoionization "V", fluorescence "F" and Auger "A" decay. Photoionization of the state $|\Psi_0\rangle$ leads to the state $|\Psi_r^{+1}\rangle$, which relaxes either by Auger decay ($\Gamma^A_{r\to t}$), by fluorescence decay ($\Gamma^F_{r\to t}$) or can be photoionized a second time ($\sigma_{r\to s}$). If the molecule falls into the Auger decay channel a second inner-shell photoionization event is possible ($\sigma_{t\to x}$). If fluorescence decay occurs, then it yields the same charge-state but a different configuration ($\Gamma^F_{u\to y}$), which subsequently undergoes a valence-shell ionization event ($\sigma_{u\to y}$). If photoionization of the core takes place with the state $|\Psi_r^{+1}\rangle$, in the next step the molecule can experience Auger decay ($\Gamma^A_{s\to v}$) or fluorescence decay ($\Gamma^F_{s\to z}$). In case that an Auger decay process happens, the system relaxes via ejecting another Auger electron ($\Gamma^A_{v\to w}$).

emitting a fluorescence photon (decay rate $\Gamma^F_{r\to t}$). We refer to these processes as PP, PA and PF (in case a valence electron is photoionized, V is used instead of P), respectively. The rate equation of the new created states $\{|\Psi_s^{+2}\rangle, |\Psi_t^{+2}\rangle, |\Psi_u^{+1}\rangle\}$ follows the same construction logic. Thus, according to the schematic representation depicted in Fig.(3.1), the molecular coupled rate equations would be written as:

$$\begin{aligned}
\dot{P}_0(z,t) &= -\sigma_{0\to r} j(z,t) P_0(z,t), && (3.3)\\
\dot{P}_r^{+1}(z,t) &= \sigma_{0\to r} j(z,t) P_0(z,t) - \sigma_{r\to s} j(z,t) P_r^{+1}(z,t) \\
&- \Gamma^A_{r\to t} P_r^{+1}(z,t) - \Gamma^F_{r\to u} P_r^{+1}(z,t) && (3.4)\\
\dot{P}_u^{+1}(z,t) &= \Gamma^F_{r\to u} P_r^{+1}(z,t) - \sigma_{u\to y} j(z,t) P_u^{+1}(z,t) && (3.5)\\
\dot{P}_s^{+2}(z,t) &= \sigma_{r\to s} j(z,t) P_r^{+1}(z,t) - \Gamma^A_{s\to v} P_s^{+2}(z,t) \\
&- \Gamma^F_{s\to z} P_s^{+2}(z,t) && (3.6)\\
\dot{P}_t^{+2}(z,t) &= \Gamma^A_{r\to t} P_r^{+1}(z,t) - \sigma_{t\to x} j(z,t) P_t^{+2}(z,t) && (3.7)\\
\dot{P}_v^{+3}(z,t) &= \Gamma^A_{s\to v} P_s^{+2}(z,t) - \Gamma^A_{v\to w} P_v^{+3}(z,t) && (3.8)
\end{aligned}$$

The last equations show how several states can have losses and gains by means of photoionization rates (which depend on the x-ray photon flux). The absorption of the photon flux will inevitably affect the forthcoming ionization dynamics. Therefore, the necessity on accounting for the absorption as the pulse propagates along the medium.

One should notice that, in principle, photoionized electrons and Auger electrons may further damage the rest of molecules by, for example, secondary ionization. However, in our model we can neglect electron impact ionization [38, 76] caused by free electrons (like photoelectrons or Auger electrons) created by the XFEL pulse, provided that the densities under consideration are relatively low and pulses are of a few femtoseconds long[1].

3.3 Absorption of the x-ray pulse

After the x-ray pulse enters into the gas medium it no longer propagates in free space. So under the assumption that in regions of space there are not free charges nor free currents, the wave equation in SI units reads [52, 78]

$$\nabla^2 \mathbf{E} - \frac{1}{\varepsilon_0 c^2} \frac{\partial^2 \mathbf{D}}{\partial t^2} = \mathbf{0}, \qquad (3.9)$$

[1] At 100 eV the electron-impact ionization σ_{el} cross section of neutral CO maximizes [77]. Assuming a gas density of $n_0 = 1.6e19$ cm^{-3} the mean free path $\lambda = 1/(n_0\sigma_{\text{el}})$ gets a value of roughly 1.0e-3 mm. The distance traveled by electrons at 100 eV within 50 fs is around 1.0e-4 mm, so that we do not need to take care of electron-impact ionization for pulse durations $\leq$ 500 fs.

where $\mathbf{D} = \varepsilon_0 \mathbf{E} + \mathbf{P}$, ε_0 is the vacuum permitivity, $\mathbf{P}$ is the polarization vector of the medium and c is the speed of light in free space.

Absorption is an optical linear response of the medium to the interaction with the electromagnetic field. It may be understood by recalling that, as a first approximation, the polarization vector is linked with the electric field via the relationship $\mathbf{P} = \varepsilon_0 \chi \mathbf{E}$. Here, the constant of proportionality χ is the linear electric susceptibility.

In our situation the electric field of the XFEL pulse is linearly polarized and propagates towards increasing z. Hence, using that $\mathbf{E}(\mathbf{r}, t) = E(z, t)\hat{\varepsilon}$ -with polarization direction $\hat{\varepsilon}$- Eq.(3.9) simplifies to

$$\frac{\partial^2 E}{\partial z^2} - \frac{1+\chi}{c^2}\frac{\partial^2 E}{\partial t^2} = 0. \tag{3.10}$$

The electric field with wave number k can be decomposed into a complex envelope $\tilde{E}$ and a fast oscillating exponent describing the propagation in the forward direction [79]

$$E(z, t) = \tilde{E}(z, t)e^{i(kz-\omega t)} + \text{c.c.} \tag{3.11}$$

with c.c. referring to complex conjugate. Upon substitution of this last expression into Eq. (3.10) yields

$$\frac{\partial^2 \tilde{E}}{\partial z^2} + 2ik\frac{\partial \tilde{E}}{\partial z} - \frac{1+\chi}{c^2}\left(\frac{\partial^2 \tilde{E}}{\partial t^2} + 2i\omega\frac{\partial \tilde{E}}{\partial t}\right) = \frac{\omega^2}{c^2}\chi\tilde{E} \tag{3.12}$$

where we used that $k^2 = \omega^2/c^2$ to drop out one of the appearing terms.

Typical XFEL pulses are femtoseconds long and their available photon energies -within the x-ray regime- result in carrier oscillation periods of a few attoseconds (10^{-18} s). Thus, it is permissible to neglect the second order derivatives appearing in Eq.(3.12), on the grounds that the ratio of the carrier frequency ω to the envelope temporal changes is much smaller than unity ($\sim 10^{-3}$). This approximation is known as the slowly varying envelope approximation [78] and is valid whenever

$$\left|\frac{\partial^2 \tilde{E}}{\partial z^2}\right| \ll \left|k\frac{\partial E}{\partial z}\right|; \quad \left|\frac{\partial^2 \tilde{E}}{\partial t^2}\right| \ll \left|\omega\frac{\partial E}{\partial t}\right| \tag{3.13}$$

Exploiting that the electric susceptibility in the x-ray regime has a magnitude that is small in comparison to 1, leads Eq.(3.12) to the following expression

$$\frac{\partial \tilde{E}}{\partial z} + \frac{1}{c}\frac{\partial \tilde{E}}{\partial t} = -i\frac{\omega}{2c}\chi\tilde{E} \tag{3.14}$$

The electric susceptibility is composed of a real and imaginary part, i.e., $\chi = \chi' - i\chi''$ and the imaginary part can be represented in terms of the absorption coefficient α as $\chi'' = 2\alpha c/\omega$. On the other hand, the absorption coefficient of the gaseous medium is found to be

$$\alpha = n_0 \sum_{n}^{N_{\text{config}}} \sigma_n^{\text{tot}} \cdot P_n, \tag{3.15}$$

where the total cross section σ_n^{tot} of the configuration n is given by

$$\sigma_n^{\text{tot}} = \sum_{n' \neq n}^{N_{\text{config}}} \sigma_{n \to n'}, \tag{3.16}$$

i.e., is the sum of all ionization cross sections that correspond to the initial configuration n. It runs over the set of final configurations $\{n'\}$ that are accessible by means of photoionization.

Therefore the electric field evolves in space and time according to the equation

$$\frac{\partial \tilde{E}}{\partial z} + \frac{1}{c}\frac{\partial \tilde{E}}{\partial t} = -n_0 \cdot \left(\sum_{n}^{N_{\text{config}}} \sigma_n^{\text{tot}} \cdot P_n \right) \tilde{E} \tag{3.17}$$

In a similar fashion, the evolution of the flux $j = c \cdot |\tilde{E}|^2/(8\pi\omega)$ [79] along the medium can be derived from the electric field, since

$$\frac{\partial |\tilde{E}|^2}{\partial z} + \frac{1}{c}\frac{\partial |\tilde{E}|^2}{\partial \tilde{t}} = \tilde{E} * \left(\frac{\partial \tilde{E}}{\partial z} + \frac{1}{c}\frac{\partial \tilde{E}}{\partial t} \right) + \text{c.c.} \tag{3.18}$$

After using Eq.(3.17) we deduce that the photon flux propagates as

$$\frac{\partial j}{\partial z}(z,t) + \frac{1}{c}\frac{\partial j}{\partial t}(z,t) = -n_0 \cdot \left[\sum_n^{N_{\text{config}}} \sigma_n^{\text{tot}}(\omega) \cdot P_n(z,t) \right] \cdot j(z,t), \tag{3.19}$$

which means that the photon flux will be attenuated due to the absorption by all the ions species created after the interaction of the molecule with the x-ray pulse.

The spatial-temporal evolution of the photon flux (Eq.(3.19)) is coupled to the system of rate equations (Eq. (3.1)) and both equations are solved self-consistently by XCO_REQ. The XCO_REQ code implements the rate equation system and solver of XMOLECULE toolkit and merges it with Eq. (3.19) using the numerical approaches sketched in the following section.

3.4 XCO_REQ: Numerical methods

It is often convenient to represent Eq. (3.19) in the reference frame of a moving window that travels towards increasing $\hat{z}$ with velocity c; i.e, $J(z;t') = j(z, t - z/c)$ with $t' = t - z/c$ the retarded time [46, 80, 79]. Hence, the equations to be solved that determine the time-dependent occupation probability distribution and the x-ray pulse propagation are:

$$\frac{\partial P_n}{\partial t'}(z,t') = \sum_{n' \neq n}^{N_{\text{config}}} \left[P_{n'}(z,t')\Gamma_{n' \to n} - \Gamma_{n \to n'} P_n(z,t') \right] \tag{3.20}$$

$$\frac{dJ}{dz}(z;t') = -n_0 \cdot \left[\sum_n^{\text{all config}} \sigma_n^{\text{tot}} \cdot P_n(z,t') \right] \cdot J(z;t') \tag{3.21}$$

The spiky nature of XFELs intensity profile does not play a relevant role in the present work (see section 2.3) [34], either gaussian or flat-top envelopes should reproduce a similar evolution of the created states. In this thesis, all numerical simulations were carried out using a temporal flat-top envelope. To avoid convergence problems due to the abrupt change at the flat-top envelope's ends, we introduce a smooth ramp that turns on and off the pulse (see Appendix A).

Choosing the length of the moving window as the pulse duration τ for $t' \in [0, \tau]$ Eqs. (3.20) and (3.21) are solved in a self-consistent manner. (In

case that a gaussian envelope is employed one can increase the moving window's length to cover its decaying tails). Here, discretization of the moving window is done as $N_t = \tau/\delta t$ where $\delta t = 0.02$ is the length of the time step. The medium's length is divided into $N_z = L/\delta z$ spatial steps with $\delta z = c\ \delta t$. In such a way, for an arbitrary position in the medium z_0, the initial and boundary conditions are set to $P_n(z, t' = 0) = \delta_{n0}$ and $J(z_0, t' = 0) = J(m \cdot c\ \delta t, t' = 0)$ for $m = 0, 1, 2, ..., N_z$.

`XMOLECULE` toolkit numerically solves Eq.(3.20) using the fourth-order Runge-Kutta method [81] and `XCO_REQ` uses the Two-step Adams-Bashforth method [82] for the photon flux propagation (Eq. (3.21)). Due to the cylindrical focus profile of the assumed XFEL beam, the 1D model (Eqs.(3.1) and (3.19)) is invariant to the rescaling of the density and length of the medium. Therefore, we reduce CPU time increasing the molecular density n_0 by a factor of 10^2, and downscaling the length L of the medium by the same factor, so that the optical density $n_0 L$ is kept constant.

When the pulse is over ($j(z, t) = 0$ for $t > \tau$) the molecule is further relaxed according to the Auger and fluorescence decay rates. To obtain the final (or equilibrium) population distribution $P_n^{(\mathrm{eq})} = P_n(z, \infty)$ instead of solving the rate equations using the fourth-order Runge-Kutta method, `XMOLECULE` toolkit rather relaxes the molecular system as

$$P_n^{(s+1)} = P_n^{(s)} + \frac{1}{\Gamma_n^{\mathrm{tot}}} \sum_{n' \neq n}^{N_{\mathrm{config}}} \left(P_{n'}^{(s)} \Gamma_{n' \to n} - \Gamma_{n \to n'} P_n^{(s)} \right), \tag{3.22}$$

where the total decay rate Γ_n^{tot} is given by

$$\Gamma_n^{\mathrm{tot}} = \sum_{n' \neq n}^{N_{\mathrm{config}}} \Gamma_{n' \to n}, \tag{3.23}$$

i.e., is the sum of all Auger and fluorescence rates for a given configuration n. The quantity $1/\Gamma_n^{\mathrm{tot}}$ is often called the *natural* time scale of the configuration n.

The Eq. (3.22) is iterated over s until no further relaxation happens, which occurs when $P_n \Gamma_n^{\mathrm{tot}} = 0$, i.e., when there are no configurations that can decay.

Chapter 4

Single-pulse studies

4.1 Introduction

We consider a XFEL beam that interacts with a carbon monoxide (CO) gas. Initially the molecular gas-phase target is assumed to be in its ground state, to have a molecular density fixed to $n_0 = 1.6 \times 10^{19}$ cm^{-3} (pressure of $\sim$ 452.7 Torr at room temperature [83], corresponding to typical experimental conditions [84]) and to be $L = 15$ mm long.

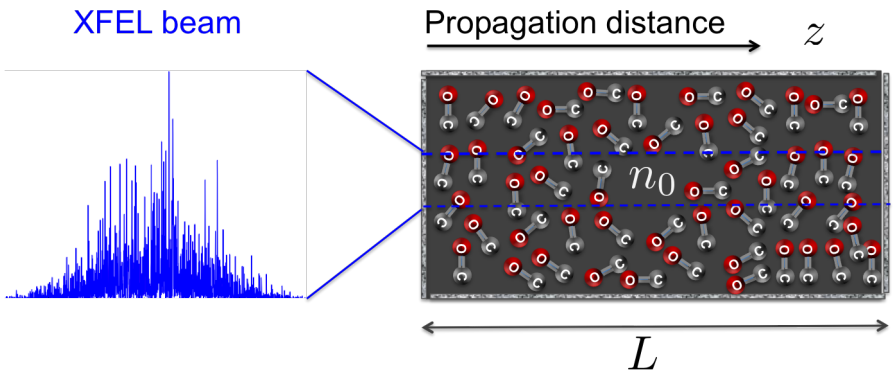

Figure 4.1: A XFEL beam interacts with a carbon monoxide (CO) gas of density n_0 and length L. Initially, it is assumed that all molecules are in their neutral ground state and are randomly oriented with respect to the polarization of the XFEL pulse.

The XFEL pulse carries an intensity given by

$$I(z,t) = j(z,t)\hbar\omega = \frac{n_{\mathrm{EM}}(z,t)\cdot\hbar\omega}{\tau}, \tag{4.1}$$

where $j(z,t)$ is the photon flux [photons·m^{-2}s^{-1}], $\hbar\omega$ the photon energy,

n_{EM} the photon fluence [photons·m^{-2}] and τ the pulse duration [s] (see Fig. (4.1)). Being N_{EM} the number of photons in the pulse, the photon fluence is defined as

$$n_{\mathrm{EM}} = \frac{N_{\mathrm{EM}}}{\pi r_0^2}, \tag{4.2}$$

i.e., the XFEL beam is assumed to have a circular transverse profile of radius r_0.

We theoretically investigate the response of electronic damage -that is, removal and rearrangement of electrons- including the absorption of the XFEL beam. Different FEL beam parameters are scanned, such as the incoming peak photon fluence n_{EM}, pulse duration τ and the photon energy $\hbar\omega$ [eV].

The present chapter is structured as follows: In section 4.2 we discuss the dependence of the calculated photoionization cross sections on the employed photon energies for different ionic configurations of CO, together with the relaxation rates of various channels. Then, having got a first glimpse on the magnitude of such quantities, in section 4.3, we concentrate on the electronic damage caused by the XFEL pulse by analyzing the charge state temporal evolution, the final populations (or ion yields) as well as the spatial distribution of the created ions along the medium. Section 4.4 is devoted to the study of the transmission of the XFEL pulse and to the explanation of the nonlinear effect known as saturable absorption. We also introduce the x-ray absorption length of the charge state $+q$, which is a measure of how deep the XFEL pulse can penetrate into a molecular gas composed of CO^{+q}.

4.2 Carbon monoxide

Carbon monoxide (CO) consists of one carbon (C) atom and one oxygen (O) atom, which together have a total of 14 electrons. The energy level diagram of CO is shown in Fig. 4.2

Accordingly, the ground state configuration of neutral CO is

$$^1\Sigma_g = (1s_O)^2(1s_C)^2(1\sigma)^2(2\sigma)^2(1\pi)^4(3\sigma)^2$$

In our simulations we employ three different photon energies ($\hbar\omega$ = 525, 540 and 740 eV). These lie above the CO K1s_C-edge (296 eV), while the latter two are above the K1s_O-edge (538 eV), as seen from Fig. 4.2. For each photon energy, we calculate cross sections and transition rates for all the accessible electronic configurations $n = 0, 1, 2, ..., N_{\mathrm{config}}$ that can be formed by removing 0,1,2,3 or 4 electrons from occupied MOs. With the assumed

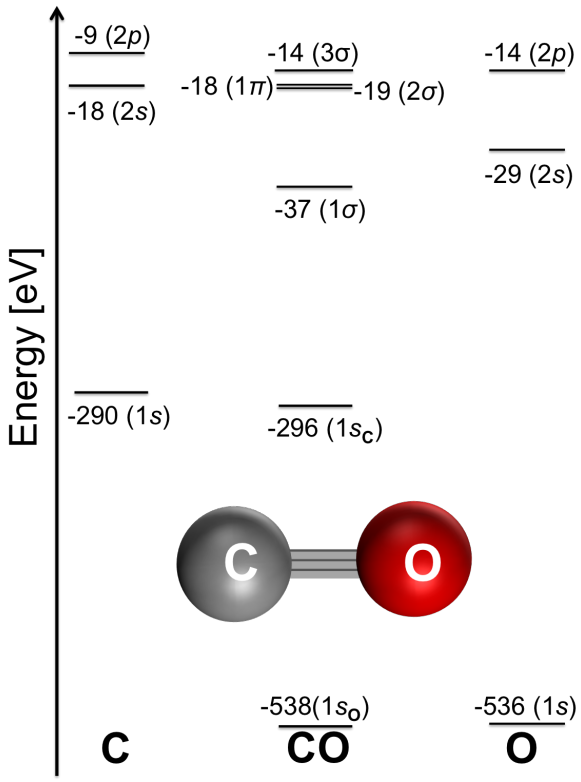

Figure 4.2: Energy level diagram of carbon (C), oxygen (O) and carbon monoxide (CO). The binding energies were calculated by the `XATOM` and `XMOLECULE` toolkits [73, 45].

photon energies there are $\geq$ 20 500 involved transition channels and therewith $N_{\text{config}} = 2187$ rate equations (each of them associated to an electronic configuration) to be solved self-consistently.

Some of the cross sections (Eq. (2.57)) and decay rates (Eqs. (2.62), (2.69)) of various configurations of CO computed by `XMOLECULE` toolkit [45] can be found in Tables B.1 - B.5 in Appendix B. For low charge states ($q \leq 7$) instead of referring to the whole configuration, the number of removed electrons in each MO is marked. In the following, since it is desirable to know the electronic configurations for which the XFEL beam has access, the next section is dedicated to the study of the calculated cross sections and decay rates. We examine their dependence on the photon energy as well as the involved initial and final states.

4.2.1 Photoionization cross sections

Figure 4.3 shows the cross sections for photoionizing the $(1s_O)$, $(1s_C)$, (1σ), (2σ), (1π) or the (3σ) MO of ground state configurations of the first eleven charge

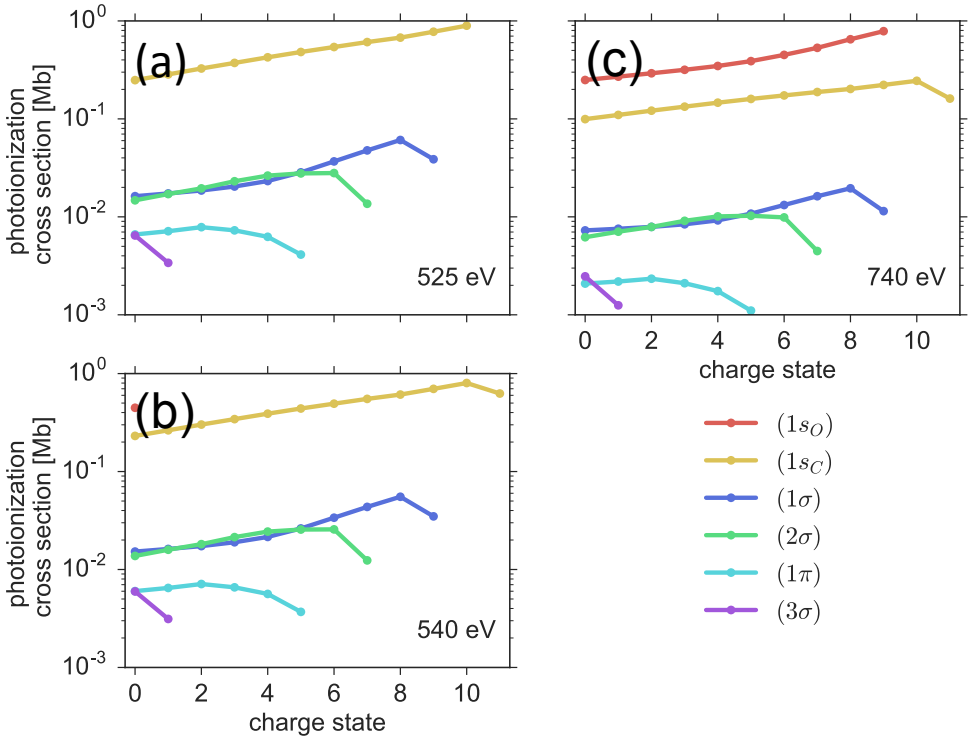

Figure 4.3: X-ray photoionization cross sections of ground state configurations for various charge states CO^{+q} at (a) 525 eV, (b) 540 eV and (c) 740 eV. Each line corresponds to a molecular orbital, which can be either the $(1s_O)$, $(1s_C)$, (1σ), (2σ), (1π) or the (3σ) MO. When lines are cut, means that the cross sections are zero.

states of CO at (a) 525, (b) 540 and (c) 740 eV.

Provided the proximity of photon energies to the ionization thresholds of MOs, cross sections of valence shells are tended to have values at least one order of magnitude smaller than ionization cross sections of inner-shells ($\sigma \approx 10^{-1}$ for $(1s_O)$ and $(1s_C)$, $\sigma \approx 10^{-2}$ Mb for (1σ) and (2σ), and $\sigma \approx 10^{-3}$ Mb for (1π) and (3σ)). Cross sections for ionizing the $(1s_C)$ MO are typically larger at 525 eV than at 540 eV and 740 eV (depending on the configuration). Figure 4.3 also shows that cross sections for ions in their ground state increase as the charge state gets higher, evidencing the impact of orbital relaxation. Likewise, it can be seen that when there is an electron left in an orbital, the cross section drops roughly by a factor of 2.0 for shells filled by two electrons and by a factor of $\sim$ 4.0 for shells filled by four electrons.

A photon at 525 eV (Fig. 4.3 (a)) cannot access to the oxygen's K-shell, because to remove a core electron from the oxygen requires at least an energy of 538 eV. However, core electrons from the carbon side can be photoionized

up to the charge state CO^{+10}, implying that the photon can even create the double core-hole state $(1s_C)^{-2}$. The K$1s_C$-edge of the ground state configuration of CO^{+11} lies at 534 eV, thus blocking the absorption of the photon and *closing* the transition channel $(1s_O)^2(1s_C)^2 \rightarrow (1s_O)^2(1s_C)^1$.

Increasing the photon energy to 540 eV (Fig. 4.3 (b)) enables photoionization of the $(1s_O)$ shell of CO only if it is in its neutral ground state. Indeed, when CO reaches the state $(1s_O)^{-1}$, the molecular shells have relaxed, such that the binding energy of the remaining electron is -602 eV. This hinders the production of a double core-hole in the $(1s_O)$ shell.

Contrariwise, a photon centered at 740 eV (Fig. 4.3 (c)) possess the sufficient energy to kick out one electron from the oxygen core until CO turns into CO^{+9}. So with this photon energy, we may saturate inner-shell photoabsorption -i.e., inner shell electrons either in the carbon or oxygen side may be removed [37, 34]-.

It should be noted that at both 540 and 740 eV the $K1s_C$-shell can be ionized for all the accessible ground state configurations.

Closed photoionization channels

As discussed in the previous section, higher-order charge states lead to relaxation of molecular orbitals, enhancing electron binding energies. For instance, according to Fig. 4.3 (c) the $(1s_O)$ shell can be photoionized until CO^{+9} is produced. For CO^{+10} the electron binding energy exceeds the photon energy and consequently an electron from the $(1s_C)$ MO cannot be taken out. In this situation, we say that the $(1s_C)$ shell *closes* for the configuration $(1s_O)^2(1s_C)^2$ or that the photoionization transition channel $(1s_O)^2(1s_C)^2 \rightarrow (1s_O)^2(1s_C)^1$ is *closed*.

For a given photon energy, there are many ionic configurations for which one or more molecular orbitals are closed. In general this happens when Eq.(2.56) is no longer valid and instead the relation

$$\hbar\omega < \varepsilon_i \tag{4.3}$$

is fulfilled. Where ε_i in Rel. 4.3 denotes the orbital energy.

Figure (4.4) shows the closed shells for different charge states. The width of each bar represents the number of configurations of a particular charge state whose transition channel via photoionization of a shell is closed. It is normalized to the total number of accessible configurations with that specific charge.

Accordingly, for the scanned photon energies, there are no closed valence shells.

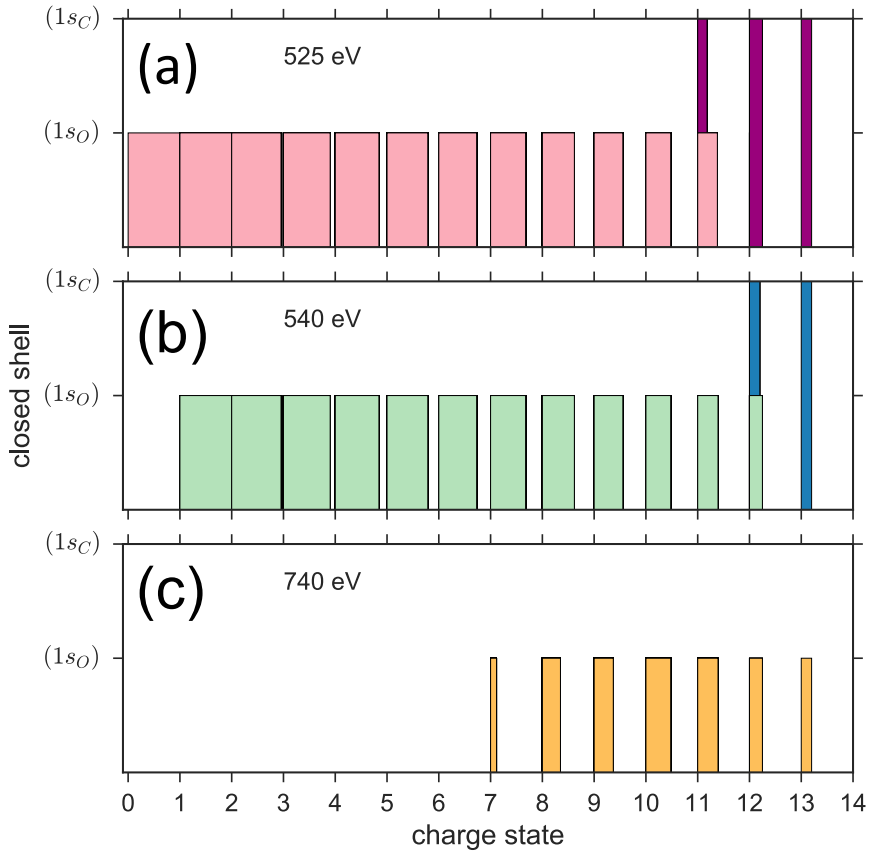

Figure 4.4: Closed shells of different CO charge states $0 \leq q \leq 14$ at (a) 525 eV, (b) 540 eV and (c) 740 eV. The bar widths of each charge state represent the number of configurations of a particular charge state that cannot be photoionized either in the $(1s_O)$ or the $(1s_C)$ inner-shell. These are normalized to the total number of accessible configuration with a specific charge.

At 525 eV, for each charge state, there is at least one electronic configuration for which the $(1s_O)$ shell is closed. This statement is equally true at 540 eV, except for neutral CO. At both photon energies, for lower charge states ($q < 3$) more than 90% of the accessible configurations have the $(1s_O)$-shell closed. For charge states lying in between $4 \leq q \leq 10$ the percentage of closing channels of the oxygen core drops from $\sim$ 80% to $\sim$ 50%, owing to the fact that more excited states start to appear. Closing of the $(1s_C)$ MO is achieved only with higher-order charge states ($10 \leq q \leq 13$), for which the number of closing channels decreases further (to around 20% of the total number of configurations). Certainly, if the photon carries an energy of 525 eV, then the $(1s_C)$ MO closes until configurations with charge $q = +11$ are created. Whereas if the photon is at 540 eV, states which cannot undergo a transition via photoionization of the $(1s_C)$ shell start to appear at $q = +12$.

The striking fact is that at 740 eV, photons can ionize carbon core electrons for every charge state. Moreover, these highly energetic photons can ionize an electron from any shell for configurations with $q < 7$. When CO has lost half of its electrons, for less than 50% of all configurations, photoinization of the K1s-shell of oxygen is blocked.

4.2.2 Fluorescence and Auger decay rates

X-ray fluorescence and Auger decay rates computed with Eq.(2.62) and Eq. (2.69) [45], respectively, are listed in Tables B.4 - B.5 for many excited states of CO^{+q}.

As can be seen, typically Auger decay rates are greater than fluorescence decay rates; characteristic that is noticeable with most of the presented configurations. For charge states $9 \leq q \leq 14$ the Auger yield $[= \Gamma^A / \sum(\Gamma^F + \Gamma^A)]$ is less than 10%, being overcome by the fluorescence yield $[= \Gamma^F / \sum(\Gamma^F + \Gamma^A)]$. This suggests that for charge states $q \leq 9$ the Auger decay is more significant than fluorescence decay. But when the molecule looses its electrons, Auger channels start to close down making the electronic screening effect to play no longer a major role, therefore the fluorescence decay yield enhances.

4.3 Multi-photoionization

The following theoretical predictions in CO are based on numerical simulations assuming a flat-top temporal pulse profile with the following range of parameters (some of them achievable at present-day XFEL facilities [26, 21]): the chosen photon energies are 525, 540 and 740 eV. Assuming a pulse of 50 fs long and a circular spot focal spot radius fixed to $r_0 = 1.5$ μm, for the set of photon fluxes [2.8×10^7,1.4×10^8,2.8×10^8,1.4×10^9] photons $\cdot$ μm^{-2}fs^{-1}, we vary the pulse duration over 10, 50, 100 and 200 fs, keeping the flux constant. The resulting photon fluences range from 2.8×10^8 to 1.4×10^{10} photons $\cdot$ μm^{-2}, from 1.4×10^9 to 7.0×10^{10} photons $\cdot$ μm^{-2}, from 2.8×10^8 to 1.4×10^{11} photons $\cdot$ μm^{-2} and 5.6×10^9 to 2.8×10^{11} photons $\cdot$ μm^{-2} for 10, 50, 100 and 200 fs, respectively.

Besides, in order to study the extreme case of highly-energetic pulses, for 740 eV, we add to above set of photon fluxes the following values for a pulse of 50 fs long: 2.8×10^9, 1.4×10^{10},2.8×10^{10}, 1.4×10^{11} and 2.8×10^{11} photons $\cdot$ μm^{-2}fs^{-1}. Such values are varied also from 0 to 200 fs maintaining the photon flux constant.

All the parameters together yield peak intensities ranging from 2.3×10^{14} to 1.1×10^{16} Wcm^{-2} for 525 eV, from 2.4×10^{14} to 1.2×10^{16} Wcm^{-2} for 540 eV, and from 3.3×10^{14} to 3.3×10^{18} Wcm^{-2} for 740 eV.

4.3.1 Time dependence

Let $N_{\mathrm{el}}(n)$ be the number of electrons of the configuration n and let S_{+q} be the set of all configurations with charge $0 \leq q \leq 14$, such that $S_{+q} = \{n \mid N_{\mathrm{el}}(n) = 14 - q\}$. The probability to find the initially neutral molecule in an ionic state CO^{+q} at position z and time $t > 0$ is therefore

$$P^{+q}(z,t) = \sum_{n \in S_{+q}} P_n(z,t), \tag{4.4}$$

namely, the sum of all configuration probabilities P_n with charge q.

The electronic dynamical evolution of CO while it interacts with the XFEL pulse, however, may not be directly revealed from the set of charge state occupation probabilities $\{P^{+q}\}$ given by Eq. (4.4). To have at least a first glance of the dynamical evolution, we need to look at the most probable transition channels and thereby the dominant configuration probabilities. For this, we define the probability $w^{+q}_{n\to n'}$ that a molecule of configuration n and charge $+q$ turns into the configuration n' within the pulse duration τ as

$$w^{+q}_{n\to n'}(z) = \int_0^\tau dt\ \Gamma_{n\to n'} P^{+q}_n(z,t), \tag{4.5}$$

where $\Gamma_{n\to n'}$ can be either the photoionization of a core or valence electron (denoted by "P" and "V, respectively), fluorescence decay ("F") or the Auger decay ("A") rate [34]. For each charge state $+q$, the integral of Eq. (4.5) is performed over the set of configurations with that particular charge. The final configuration n' with the resulting largest -most probable- value $w^{+q}_{n\to n'}$ is retrieved. Application of this scheme in every accessible configuration decodes the most likely transition pathways that can be taken by the molecule.

Figure 4.5 displays the temporal evolution of CO and its first four charge states at the beginning of the medium ($z = 0.0$ mm) during the interaction with the x-ray pulse. The peak fluence has been set to 1.4×10^{11} photons $\cdot\ \mu\mathrm{m}^{-2}$, the pulse duration to 100 fs and the photon energy to 540 eV, corresponding to a peak intensity of 1.2×10^{16} Wcm^{-2}.

Neutral CO decreases exponentially while higher charge states are produced (Fig. 4.5 (a)). At the very beginning the charge state CO^{+1} is produced and is the most likely to find. After a few femtoseconds ($\sim$ 6 fs) the production of CO^{+2} becomes more efficient and it remains as the most populated charge state until it is overtaken by CO^{+3} and CO^{+4} within a time of 40 to 60 fs. Higher-order charge states $4 \leq q \leq 12$ are then sequentially created, so that

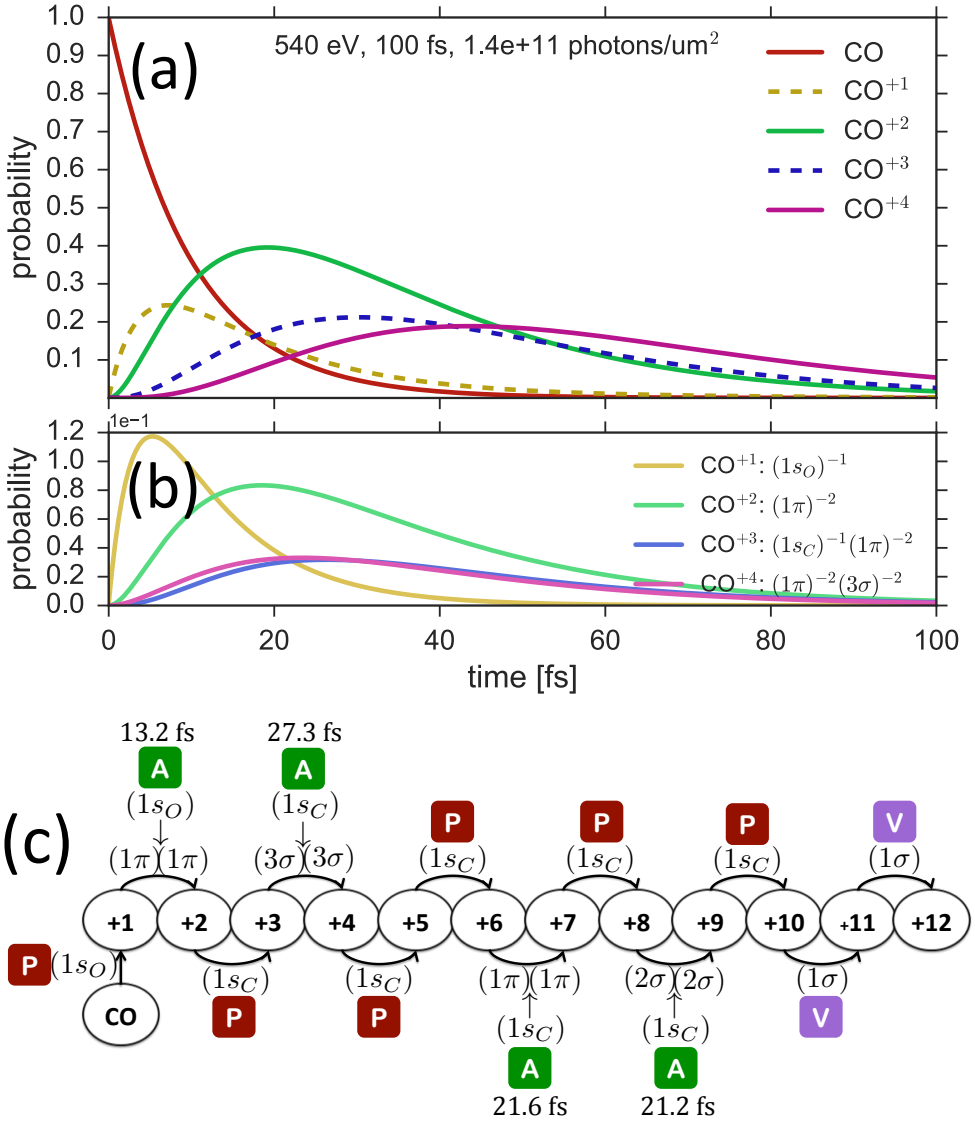

Figure 4.5: Temporal evolution within the pulse duration ($\tau = 100$ fs) at $z = 0.0$ mm of (a) charge state probabilities P^{+q} (Eq. (4.4)) and (b) configuration probabilities P_n of CO^{+1}, CO^{+2}, CO^{+3} and CO^{+4}. (c) Schematic of the most probable transition channels (Eq. 4.5) within the pulse duration. The molecular processes displayed are photoionization of a core "P" or valence "V" shell (i), and Auger decay "A" $(i) \rightarrow (j)(j')$ in which an inner-shell hole (i) is refilled by a valence electron from the shell (j) while another electron from the shell (j') is ejected out. With the given beam parameters the XFEL pulse ($\hbar\omega = 540$ eV) has a peak intensity of 1.2×10^{16} Wcm^{-2}.

at the end of pulse ($t = 100$ fs) the charge state CO^{+12} reaches the value $P^{+12} = 0.02$ and the most populated charge state is found to be CO^{+10} with $P^{+10} = 0.15$.

By employing Eq. (4.14) to derive the most probable sequence of events, it is found that the molecule will highly likely go through channels as illustrated by Fig. 4.5 (c). Since the photon energy at 540 eV lies above the CO K1s_O-edge, photoionization will most likely promote the carbon monoxide molecule to the state $(1s_O)^{-1}$. As shown in Fig. 4.5 (b) the production of this state is dominant during the first $\sim$ 13 fs. Within this time the photoionization rate is insufficient to provide a second photoionization event, therefore the molecule relaxes via ejecting one Auger electron, resulting in the state $(1\pi)^{-2}$ which starts to be more significant precisely after 13 fs. Carrying on a similar argument, if the molecule is found in the double-hole excited state $(1\pi)^{-2}$, the most probable way to get a higher charge state is through photoionization of an electron from the $(1s_C)$ MO, which dominantly is followed again by an Auger decay within $\sim$ 27 fs leading to the state $(1\pi)^{-2}(3\sigma)^{-2}$. After the CO molecule goes through all the multi-photoionization and Auger decay steps following the pattern PAPAPPAPAPVV it falls into the charge state $q = +12$ with configuration $(1s_O)^2$. At 540 eV further photoionization is not possible (cf. Fig.4.3) and hence, the molecule remains in this state.

If the value of XFEL pulse parameters are changed such that the photon energy is now decreased to 525 eV, the pulse duration is 200 fs and photon fluence is set to 2.8×10^{11} photonsμm^{-2}, the evolution of $P^{+q}(z = 0, t)$ seems to be pretty similar to the case at 540 eV (Fig. 4.5 (a)) as detailed by Fig. 4.6 (a). Nonetheless, a key aspect must be emphasized: since the photon energy is between the K1s_O and K1s_C-ionization threshold, photoionization of neutral CO in its ground state promotes the molecule instead to the state $(1s_C)^{-1}$. Such state has an Auger lifetime of $\sim$ 35 fs and relaxes into the state $(3\sigma)^{-2}$ (Fig. 4.6 (c)). Afterwards, the molecule experiences two sequential photoionization events and the double core-hole state $(1s_C)^{-2}(3\sigma)^{-2}$ is produced. At this point, the Coulomb interaction between electrons is so strong that $(1s_C)^{-2}(3\sigma)^{-2}$ relaxes in $\sim$ 5 fs. The following x-ray induced processes that take the molecule to the charge state CO^{+12} turn out to be the same as with 540 eV. Utilizing these beam parameters, the molecule will follow most likely the multi-photoionization sequence PAPPAPAPAPVV.

The temporal evolution of charge states changes drastically by increasing the photon energy and the XFEL pulse peak intensity. Figure 4.7 shows charge states and configuration probabilities as a function of time during the interaction with a XFEL pulse that has a photon energy of 740 eV, is 10 fs long, and has a peak fluence of 2.8×10^{11} photons$\cdot\mu$m^{-2}. These parameters yield a peak intensity of 3.3×10^{17} Wcm^{-2}.

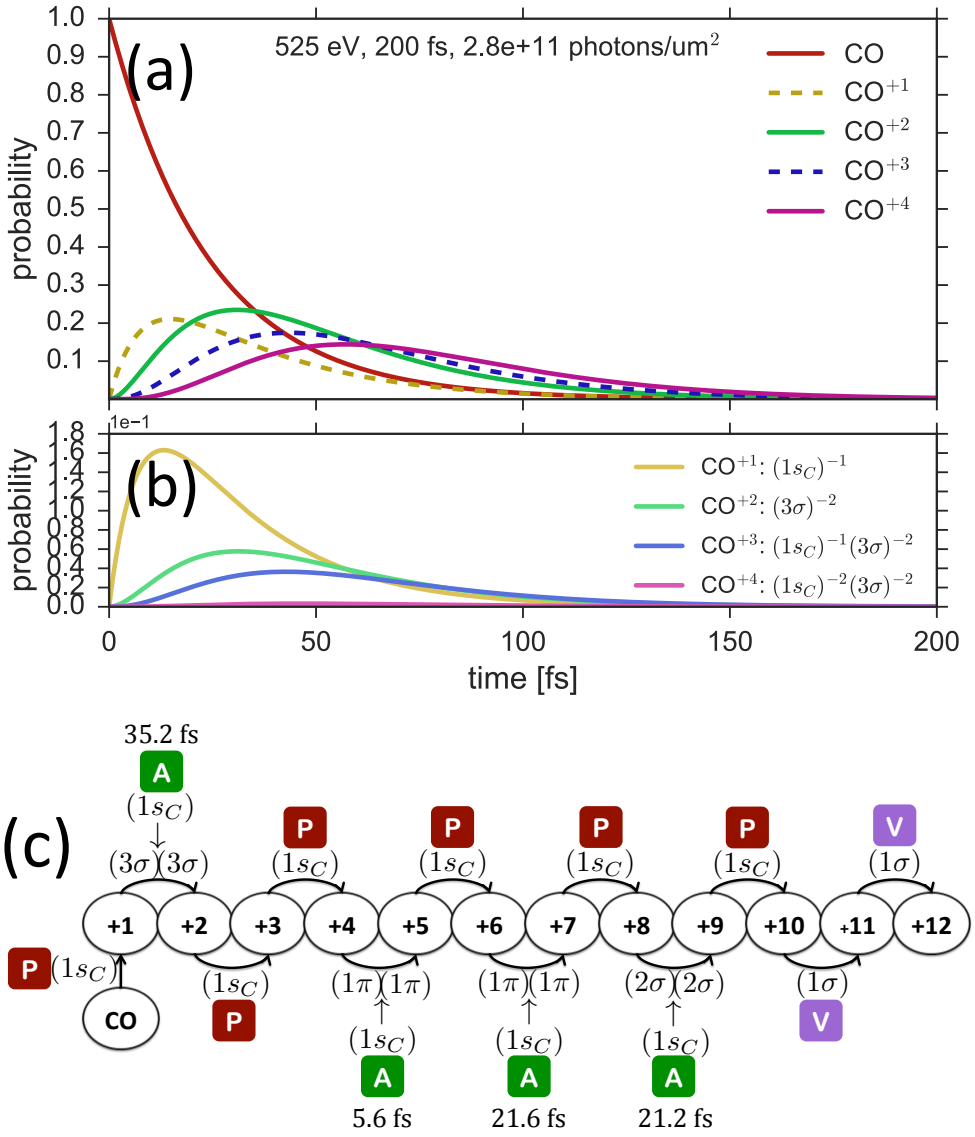

Figure 4.6: Temporal evolution within the pulse duration ($\tau = 200$ fs) at $z = 0.0$ mm of (a) charge state probabilities P^{+q} and (b) configuration probabilities P_n (Eq. (4.4)) of CO^{+1}, CO^{+2}, CO^{+3} and CO^{+4}. (c) Schematic of the most probable transition channels (Eq. 4.5) within the pulse duration. The molecular processes displayed are photoionization of a core "P" or valence "V" shell (i), and Auger decay "A" $(i) \rightarrow (j)(j')$ in which an inner-shell hole (i) is refilled by a valence electron from the shell (j) while another electron from the shell (j') is ejected out. With the given beam parameters the XFEL pulse ($\hbar\omega = 525$ eV) has a peak intensity of 1.1×10^{16} Wcm^{-2}.

In Fig. 4.7 (a), the fact that within $\sim$ 6 fs we can reach CO^{+7} ($P^{+7} = 0.09$) is striking. Actually, within this pulse duration ($\tau = 10$ fs) we may be able to produce CO^{+13} (as compared to 525 and 540 eV for which it was almost impossible). Moreover, it can be seen from Fig. 4.7 (b) that, as with 540 eV, the first most probable created excited state is $(1s_O)^{-1}$. But contrastingly, the available photon flux and photon energy enable a much more efficient production of $(1s_O)^{-2}$ than of $(1\pi)^{-2}$, as the maximum of the former ($\approx$ 0.52) is about one order of magnitude greater than the maximum of the latter ($\approx 5.5 \times 10^{-2}$). So, at these beam parameters we are able to beat the Auger decay and produce a double core-hole in oxygen [42]. Just after the molecule reaches the highly-excited double core-hole state $(1s_O)^{-2}$ it relaxes in a record time of $\sim$ 3 fs. When the pulse ends ($t = 200$ fs) there is a strong likelihood that the path taken by the molecule for turning into CO^{+13} goes according to PPAPPPAPAVVVV (note in Fig. 4.7 (c) that we have suppressed an Auger decay event).

If we further increase the peak fluence of the x-ray beam (see Fig 4.8 (a)) we are able to completely destroy the molecule by stripping it of all its electrons within $\sim$ 15 fs, encountering already $P^{+14} = 0.06$ at 30 fs. At these ultra-high intensities we can even produce the state $(1s_O)^{-2}(1s_C)^2$, i.e., a double core-hole both in the oxygen and in the carbon atom. With this x-ray pulse parameters most probable transition pathway is PPPPVAPVVVVVVV (see Fig. 4.8 (b)). There is only one Auger decay and thus, the molecule has absorbed 13 photons.

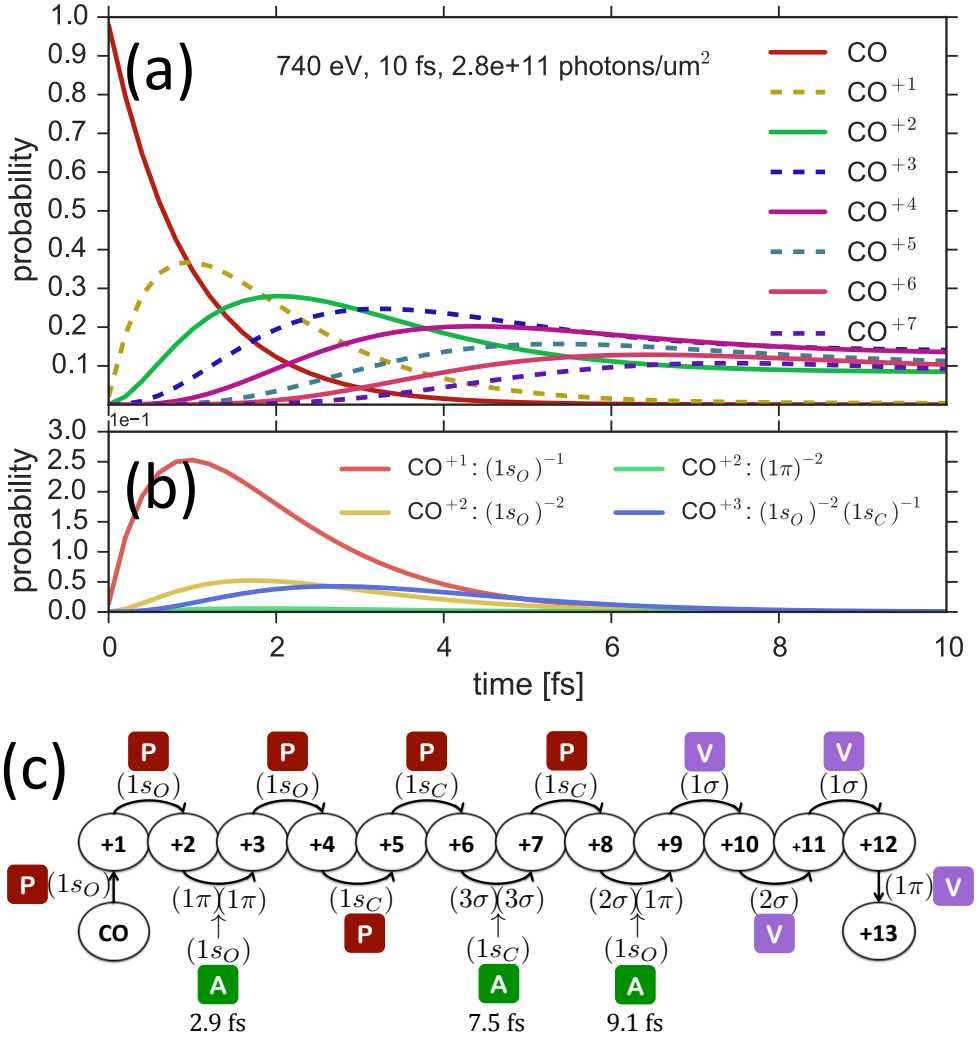

Figure 4.7: Temporal evolution within the pulse duration ($\tau = 10$ fs) at $z = 0.0$ mm of (a) charge state probabilities P^{+q} and (b) configuration probabilities P_n (Eq. (4.4)) for $0 \leq q \leq 7$. (c) Schematic of the most probable transition channels (Eq. 4.5) within the pulse duration. The molecular processes displayed are photoionization of a core "P" or valence "V" shell (i), and Auger decay "A" $(i) \rightarrow (j)(j')$ in which an inner-shell hole (i) is refilled by a valence electron from the shell (j) while another electron from the shell (j') is ejected out. With the given beam parameters the XFEL pulse ($\hbar\omega = 740$ eV) has a peak intensity of 3.3×10^{17} Wcm^{-2}.

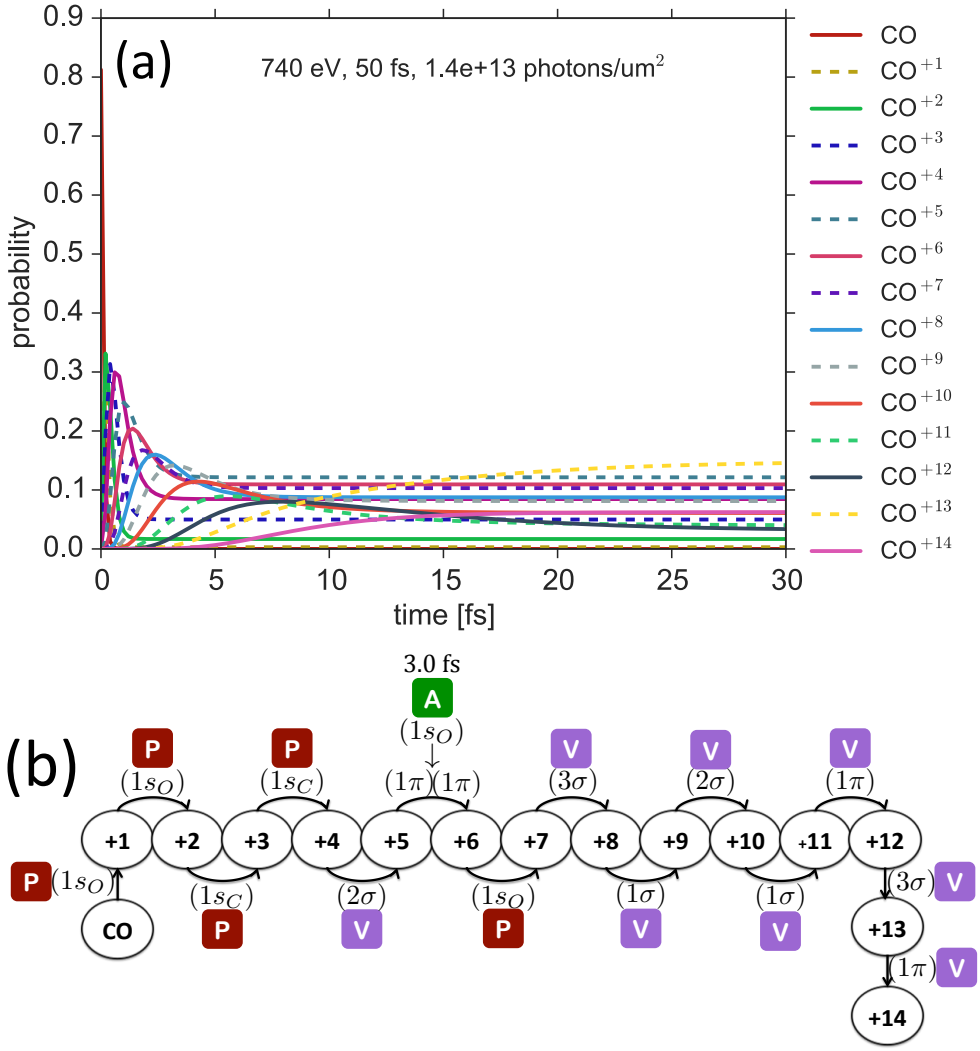

Figure 4.8: Temporal evolution within 30 fs at $z = 0.0$ mm of (a) charge state probabilities P^{+q} (Eq. (4.4)) for $0 \leq q \leq 14$. (b) Schematic of the most probable transition channels (Eq. 4.5) within the pulse duration ($\tau = 50$ fs). The molecular processes displayed are photoionization of a core "P" or valence "V" shell (i), and Auger decay "A" $(i) \rightarrow (j)(j')$ in which an inner-shell hole (i) is refilled by a valence electron from the shell (j) while another electron from the shell (j') is ejected out. The XFEL pulse ($\hbar\omega = 740$ eV) is 50 fs and has a peak intensity of 3.3×10^{18} Wcm^{-2}

4.3.2 Ion yields

After the pulse has passed and the molecules have suffered a sequence of multiple ionization events, the only thing that can happen is relaxation according to Auger and fluorescence decay rates. The molecular ion yields are the probabilities to find the molecule in the charge state $+q$ after the x-ray pulse is over ($t \to \infty$), we define them as

$$Y^{+q}(z) = \lim_{t\to\infty} P^{+q}(z,t) \tag{4.6}$$

where P^{+q} is the charge state probability defined in Eq. (4.4). Ion yields are experimentally accessible and provide a good observable that allows quantitative comparison [33, 44, 40].

Charge state distribution

Figure 4.9 shows the ion yields $Y^{+q}(z = 0.0 \text{ mm})$ with $0 \leq q \leq 14$ for different XFEL beam parameters.

Let us see first what happens with Y^{+q} at 540 eV (Fig. 4.9 (b)). With the lowest photon fluence (peak intensity of 2.4×10^{14} Wcm^{-2}) we can just photoionize around a 20% of the neutral CO molecules and to hardly remove four electrons from each them ($Y^{+4} \approx 10^{-3}$). At this fluence the ion CO^{+2} is the most populated, owing to the decay of most of the produced CO^{+1} (note that almost all the photoionized neutral molecules end in the charge state $q = 2$ with $Y^{+2} \approx 0.2$) and to the lack of photon flux to produce higher charge states. The use of 1.4×10^{10} and 2.8×10^{10} photonsμm^{-2} (or peak intensities 1.2×10^{15} and 2.4×10^{15} Wcm^{-2}, respectively) empowers the production of ions up to the charge states CO^{+6} and CO^{+8}. But, still, the ion yield of CO^{+2} dominates ($Y^{+2} \approx 0.5$). With 1.4×10^{11} photons$\cdot\mu$m^{-2} (1.2×10^{16} Wcm^{-2}), the ion yield Y^{+2} decreases abruptly in addition to the complete depletion of neutral CO and a larger probability of finding high-order charge states. For instance, CO^{+12} becomes accessible and CO^{+11} turns to be the most probable ion to find ($Y^{+11} \approx 0.2$). In section 4.4.1 with Fig. 4.17 we demonstrate that in 100 fs and with a peak intensity of 1.2×10^{16} Wcm^{-2}, there is a probability of 1.0 to photoionize neutral CO. Such an effect elucidates why Y^{+0} is essentially zero and, equivalently, why is that the photoionization probability of the rest of the MOs enlarges, enhancing thus the yield of higher charge states.

When decreasing the photon energy down to 525 eV (Fig. 4.9 (a)) over the range of the employed peak intensities, despite the fact that the pulse duration is two times longer less neutral CO molecules are depleted compared to 540 eV. This happens on the grounds that photoionization cross sections

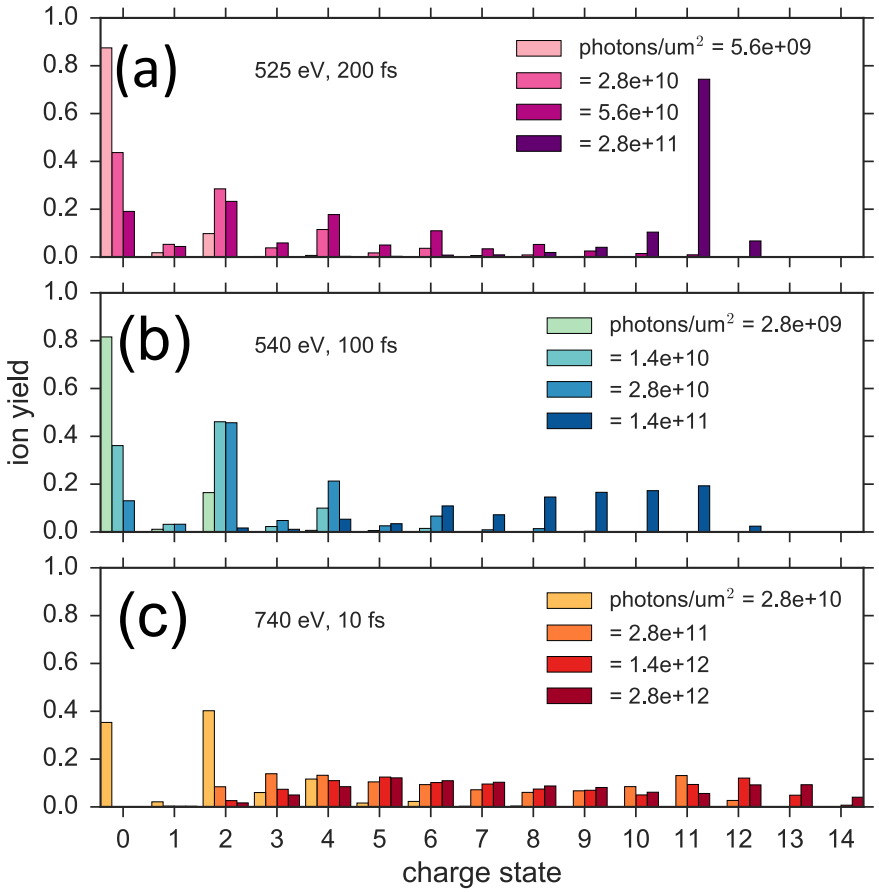

Figure 4.9: CO charge state yields Y^{+q} (Eq.(4.6)) at $z = 0.0$ mm for XFEL pulses at (a) $\hbar\omega = 525$ eV and duration $\tau = 200$ fs; (b) 540 eV and 100 fs (c) 740 eV and 10 fs. These parameters together with the photon fluences [photons·μm^{-2}] yield peak intensities ranging from (a) 2.3×10^{14} to 1.1×10^{16} Wcm^{-2}, (b) from 2.4×10^{14} to 1.2×10^{16} Wcm^{-2} and (c) from 3.3×10^{16} to 3.3×10^{18} Wcm^{-2}.

of neutral CO at 525 eV are smaller by roughly a factor of two than at 540 eV, as discussed in section 4.2.1 and section 4.3.1. Contrastingly, with the highest photon fluence (peak intensity of 1.1×10^{16} Wcm^{-2}) when $t \to \infty$ almost 80% of the molecules have turned into CO^{+11}, while at $t = \tau = 200$ fs there was only about a 60% (see Fig. 4.6). This clearly indicates that most of the excited states have relaxed into CO^{+11}.

Charge-state distribution rearranges if we increment the photon energy to 740 eV and simultaneously the range of peak intensities. In Fig. 4.9 (c), it turns out that (apart from depleting once again neutral CO molecules with the highest intensities and reaching a non-zero yield of CO^{+14}) charge-states with $0 \leq q \leq 4$ appear to distribute nearly in an uniform way, lying below

≈ 0.1.

Figures 4.10 and 4.12 display CO ion yieldsY^{+q} for different pulse durations (τ = 10, 50, 100 and 200 fs) and similar photon fluxes (the photon flux is kept constant while the pulse duration is varied). The corresponding peak intensities are 1.1×10^{15} Wcm^{-2} and 1.1×10^{16} Wcm-2 for 525 eV, 1.2×10^{15} Wcm^{-2} and 1.2×10^{16} Wcm-2 for 540 eV, and 1.6×10^{15} and 1.6×10^{16} Wcm-2 for 740 eV

From Figs. 4.10 and 4.12 we can see that CO ion yields either at 525, 540 or 740 eV decrease monotonically from 200 fs to 10 fs for pulses with similar photon flux as shown by Fig 4.12. This exhibits that CO and its ions cannot absorb photons as efficiently for short pulses as for longer pulses. What is more, as we tune the photon energy from 525 to 740 eV, the probability of producing higher-order charge states is also found to be higher.

To sum up, either by increasing or reducing the intensity or/and the photon energy, we can modulate the impact on the electronic damage (i.e., the charge of the achieved ions and their probability at $t \to \infty$). Over the range of parameters investigated, pulses with comparable peak intensity but increasing duration give rise to the observation of the highest charge states whereas pulses with decreasing pulse duration leads to almost lower charge states.

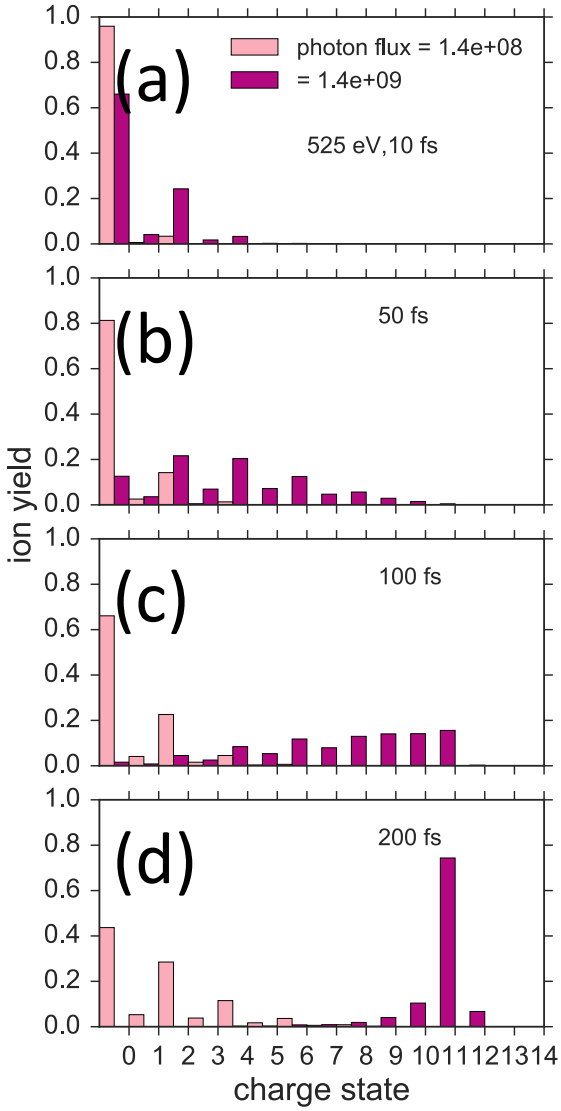

Figure 4.10: CO charge state yields Y^{+q} (Eq.(4.6)) at $z = 0.0$ mm for XFEL pulses ($\hbar\omega = 525$ eV) of different duration ((a) $\tau = 10$ fs; (b) 50 fs (c) 100 fs and (d) 200 fs). The photon flux [photons·μm^{2}fs^{-1}] is kept constant for all pulse durations, resulting in peak intensities of (pink) 1.1×10^{15} Wcm^{-2} and (magenta) 1.1×10^{16} Wcm^{-2}.

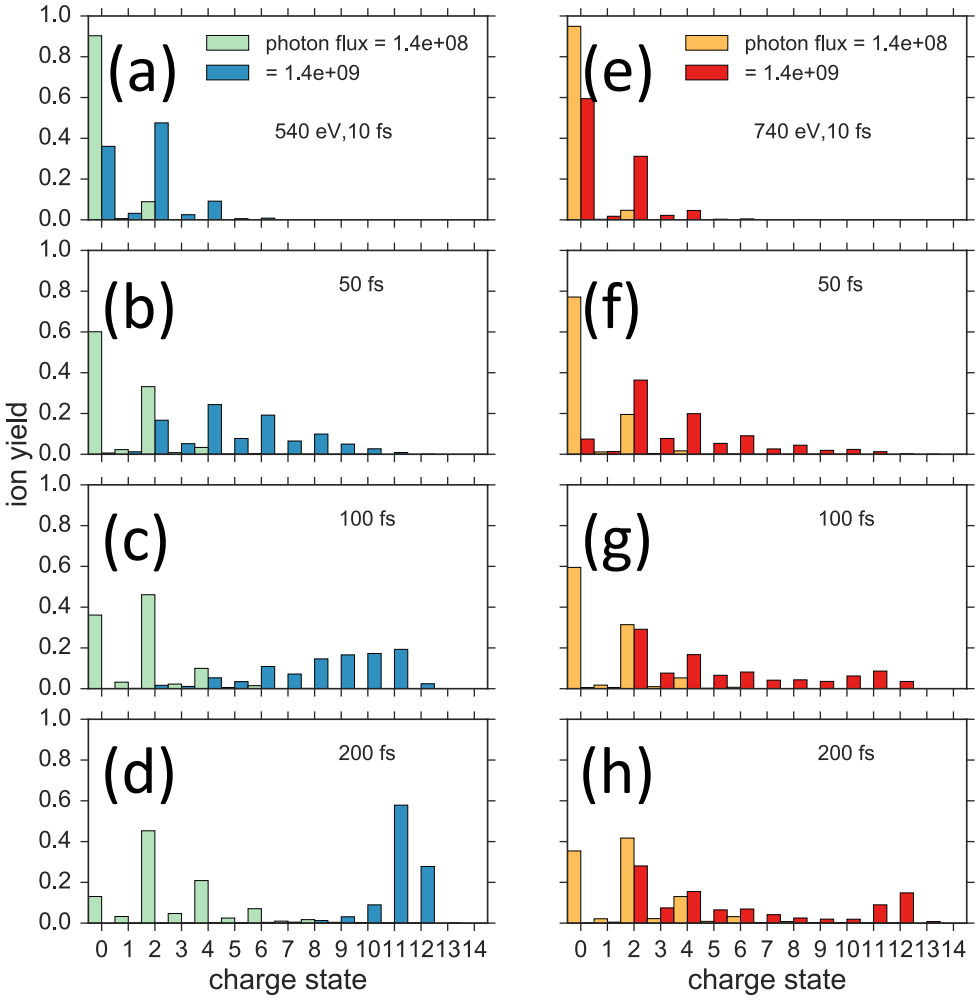

Figure 4.11: CO charge state yields Y^{+q} (Eq.(4.6)) at $z = 0.0$ mm for XFEL pulses ((a)-(d)$\hbar\omega = 540$ eV and (e)-(h) 740 eV) of different duration ((a),(e) $\tau = 10$ fs; (b),(f) 50 fs (c),(g) 100 fs and (d),(h) 200 fs). The photon flux [photons$\cdot\mu$m^{2}fs^{-1}] is kept constant for all pulse durations, resulting in peak intensities of (green) 1.2×10^{15} Wcm^{-2} and (blue) 1.2×10^{16} Wcm-2 for 540 eV, and (orange) 1.6×10^{15} and (red) 1.6×10^{16} Wcm^{-2} for 740 eV.

Multi-photoionization sequence

We have analyzed the time dependence of the created charge states during the interaction with the XFEL pulse together with their population long after the pulse has passed. Actually, in the examples displayed in Figs. 4.12 and 4.10, one can notice that most of times charge states with even charge are more populated than charge states with odd charge, as long as the peak intensity is maintained relatively low. This reveals that the sequence of x-ray induced processes should follow the pattern PAPAPA..., provided that for small peak intensities -or for intensities within the perturbative regime- the ionization rate is typically smaller than the Auger decay rate. This last statement rises the question of whether it is possible to determine the most probable sequence of ionization and relaxation events from the ion yields.

In the perturbative regime neutral CO is hardly depleted, meaning that the ground state population is approximately constant with $P_0 \approx 1$. In this regime, the charge state yields follow a power-law dependence with the XFEL pulse peak intensity I as

$$Y^{+q} \approx \frac{\sigma_{+q}^{(n_p)}}{(\hbar\omega)^{n_p}} I^{n_p}, \tag{4.7}$$

where n_p is the number of necessary photons to achieve a given charge state and $\sigma_{+q}^{(n_p)}$ is the effective n_p-photon cross section for a given charge state $+q$. Its units are $\mathrm{Mb}^{n_p}\mathrm{s}^{n_p}$ [85, 34].

In Fig. 4.12 we show the charge state yields as a function of the incoming pulse peak intensity at (a) 525 eV, (b) 540 eV and (c) 740 eV. The pulse duration is set to 10 fs. From Fig. 4.12 (a)-(b), it is found that neutral CO is barely depopulated ($<$ 20% of neutral molecules are depleted) for intensities below $\sim 2.4 \times 10^{15}$ Wcm^{-2} (2.8×10^{9}photons$\cdot\mu\mathrm{m}^{-2}$), implying that the intensity region is within the perturbative limit.

In the same fashion, at 740 eV (Fig. 4.12 (c)) the flattening of the curves for $1 \leq q \leq 13$ and the depletion of neutral CO after 1.6×10^{16} Wcm^{-2} (2.8×10^{9} photons$\cdot\mu\mathrm{m}^{-2}$) mark the limit of the perturbative intensity region. It is astonishing how after the perturbative limit neutral CO is rapidly depleted as the pulse peak intensity increases, being essentially zero at $\sim 10^{18}$ Wcm^{-2}. Likewise, we see that at these very high intensities, ion yields tend to a value, which is approximately 0.1 for $1 \leq q \leq 13$.

From the power-law dependence (Tab. 4.1) it follows that CO^{+1} is a one-photon process, just as CO^{+2}. In section 3.2 we denoted the process of photoionization followed by an Auger decay as PA. In a similar fashion, it

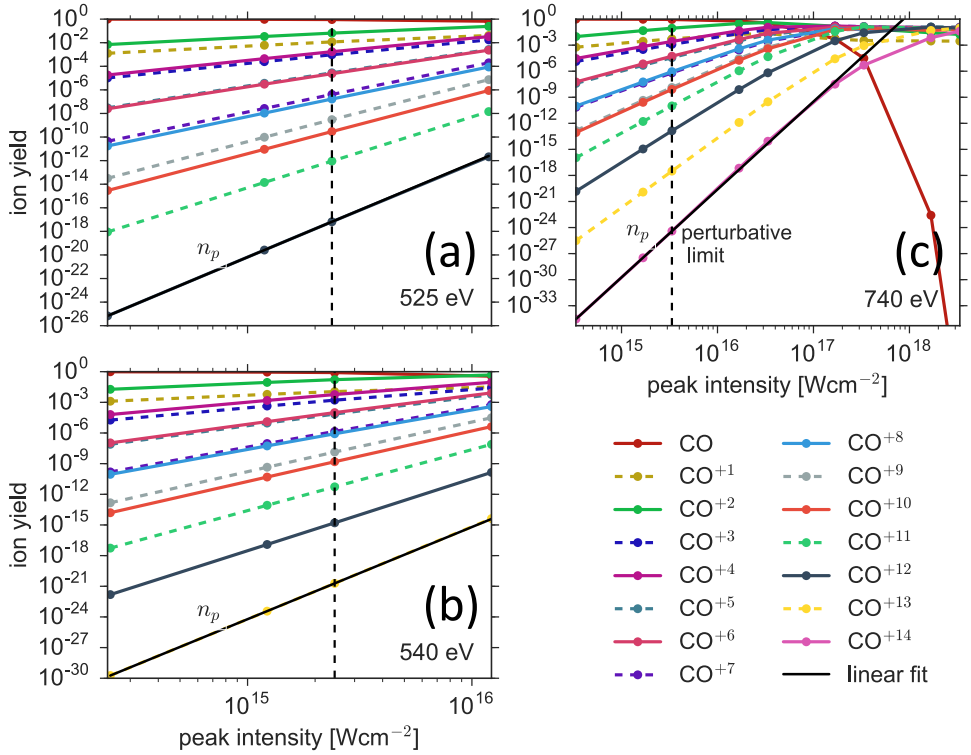

Figure 4.12: Charge state yields Y^{+q} (Eq. (4.6)) at $z = 0.0$ mm as a function of x-ray pulse peak intensity employing photon energy of (a) 525 eV, (b) 540 eV and (c) 740 eV. The pulse duration is 10 fs. The range of covered intensities corresponds to peak fluences $n_{\text{EM}} \in [2.8 \times 10^8, 1.4 \times 10^1]$ photons·μm^{-2} for 525 eV and 540 eV, and $n_{\text{EM}} \in [2.0 \times 10^8, 2.0 \times 10^{12}]$ photons·μm^{-2} for 740 eV. The number n_p is the exponent of a power-law fit and is a measure of the number of photons needed to achieve a given charge state. The black vertical line defines the limit of the perturbative regime.

is found that CO^{+3} and CO^{+5} are two- and three-photon processes, respectively. Following this reasoning, we find that CO^{+11} is a six-photon process. Valence ionization occurs only rarely before the closure of a core-ionization channel, because the associated cross section are typically -at least- one order of magnitude smaller than cross sections of core electrons (cf. Figs.4.3 and 4.4). Thus, at 525 eV, the sequence of multi-photoionization events should go as PAPAPAPAPAP.

According to Tab. 4.1 at 540 eV production of CO^{+12} is a seven-photon process. The creation of such charge state does not involve the closing of the $(1s_C)$-shell for any electronic configuration (cf. 4.4), hence, it will most probably be achieved through the sequence PAPAPAPAPAPP. With a similar argument, since at 740 eV the ion yield Y^{+13} is proportional to the eight power of the intensity, it should be an eight-photon process. Moreover, at

Table 4.1: Generalized cross sections $\sigma_{+q}^{(n_p)}$ and number of absorbed photons n_p by the charge state $+q$ at different photon energies (525, 540 and 740 eV) . The values result from the power law fit of charge state yields Y^{+q} vs. x-ray pulse peak intensity in Fig. 4.12.

	at 525 eV		at 540 eV		at 740 eV	
Charge	$\sigma[\mathrm{Mb}^{n_p}\mathrm{s}^{n_p}]$	n_p	$\sigma[\mathrm{Mb}^{n_p}\mathrm{s}^{n_p}]$	n_p	$\sigma[\mathrm{Mb}^{n_p}\mathrm{s}^{n_p}]$	n_p
+1	1.1×10^{-15}	0.9	2.0×10^{-15}	0.9	6.0×10^{-16}	0.9
+2	5.3×10^{-15}	0.9	2.9×10^{-14}	0.9	9.0×10^{-15}	0.9
+3	2.9×10^{-30}	1.9	8.4×10^{-30}	1.9	3.8×10^{-30}	1.9
+4	4.6×10^{-30}	1.9	2.7×10^{-29}	1.9	9.8×10^{-30}	1.9
+5	2.8×10^{-45}	2.9	1.0×10^{-44}	2.9	4.5×10^{-45}	2.9
+6	2.0×10^{-45}	2.9	1.3×10^{-44}	2.9	7.0×10^{-45}	2.9
+7	1.3×10^{-60}	3.9	6.7×10^{-60}	3.9	3.0×10^{-60}	3.9
+8	4.3×10^{-61}	3.9	3.1×10^{-60}	3.9	4.1×10^{-60}	3.9
+9	3.2×10^{-76}	4.9	1.9×10^{-75}	4.9	2.2×10^{-75}	4.9
+10	1.5×10^{-77}	5.0	1.1×10^{-76}	4.9	1.1×10^{-75}	4.9
+11	1.4×10^{-93}	6.0	1.1×10^{-92}	5.9	5.2×10^{-91}	5.9
+12	-	-	5.9×10^{-110}	7.0	2.4×10^{-107}	6.9
+13	-	-	-	-	5.7×10^{-126}	8.0

740 eV carbon's inner-shell is open for all charge states, which means that the most probable way to produce CO^{+13} is according to the pattern PAPA-PAPAPAPPP.

Table 4.1 also shows that as higher-order charge states are created $\sigma_{+q}^{(n_p)}$ tends to smaller values, thus, revealing the low probability of producing such highly-charged ions.

4.3.3 Spatial dependence

So far we have a picture of how exposing a single CO molecule to the XFEL pulse can strip CO of all its 14 electrons by a sequence of inner-shell photoionization and Auger decays. Yet, we address the question of how the created ions are distributed along the medium. To do this, we need to track, at the same time, the evolution of the XFEL's photon flux as it propagates through the molecular gas.

Within the perturbative regime, as previously said, the depletion rate of molecules in their ground state is nearly zero, meaning that most of the CO molecules are such that $P_0 \approx 1$ within the interaction region. For pulses in this intensity regime, we can approximate the absorption length of the medium as

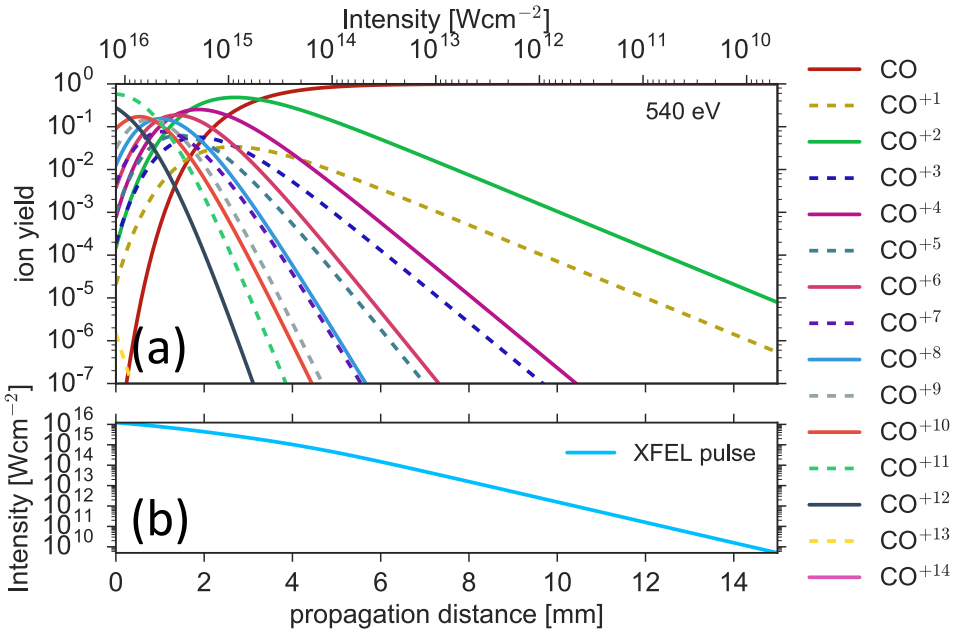

Figure 4.13: Spatial distribution of different charge state yields (a) $Y^{+q}(z)$ (Eq.(4.6)) and (b) spatial dependence of the XFEL pulse intensity along the gas medium. The pulse duration is set to 200 fs and the pulse carries a photon fluence of 2.0×10^{12} photons·μm^{-2}. These parameters result in a peak intensity of (a)-(b) 1.2×10^{16} Wcm^{-2}.

$$\lambda(\omega) \approx \frac{1}{n_0 \cdot \sigma^{\text{tot}}_{^1\Sigma_g}(\omega)} \tag{4.8}$$

where $n_0 = 1.6 \times 10^{19}$ cm^{-3} is the density of the medium, $\sigma^{\text{tot}}_{^1\Sigma_g}(\omega)$ (Eq. 3.16) is the total cross section of CO in its neutral ground state for a certain photon energy $\hbar\omega$. In Tab. 4.2 absorption lengths of CO for photon energies at 525, 540 and 740 eV are contained, assumming a gas density of $n_0 = 1.6 \times 10^{19}$ cm^{-3} (pressure of $\sim$ 452.7 Torr at room temperature).

Figure 4.13 shows the charge state spatial distribution $Y^{+q}(z)$ arising from the interaction with a XFEL pulse at 540 eV long after the pulse passed through the medium ($t \to \infty$). Fig. 4.13 also depicts the spatial dependence of the x-ray beam intensity given by

$$I(z) = \frac{\hbar\omega}{\tau} \int_{-\infty}^{\infty} dt\; j(z,t) \tag{4.9}$$

Table 4.2: Absorption length λ (Eq. (4.8)) for a gas composed of neutral CO molecules in their ground state for different photon energies. The gas density is $n_0 = 1.6 \times 10^{19}$ cm^{-3}.

Photon energy [eV]	λ [mm]
525	2.13
540	0.86
740	1.70

The pulse is $\tau = 200$ fs long and has a photon fluence of 2.0×10^{12} photons$\cdot\mu$m^{-2}, which corresponds to a peak intensity of 1.2×10^{16} Wcm^{-2}.

Based upon $\lambda(\omega)$ at 540 eV, we can notice from Fig. 4.13 that within 6 times this value ($\approx$ 5 mm) single-photoionization gets saturated and there is a sizeable probability to find higher charge states. As already discussed in section 4.3.2, higher charge states need at least two ionization events to be produced. Hence, probability maxima of each of the created ions are shifted towards increasing intensity (low z values). Starting at 7 times the absorption length ($\approx$ 6 mm) the x-ray pulse intensity decreases down to $\sim 10^{15}$ Wcm^{-2} (Fig. 4.13 (b)) and one sees clearly a perturbative regime. The upper axis of Fig. 4.13 (a) and Fig. 4.13 (b) show that within the medium's length the intensity reduces about six orders of magnitude, underlying the comparatively high probability of absorbing a photon centered at 540 eV.

On the other hand, when using a photon at 525 eV (Fig. 4.15 (a)), one main difference we can pinpoint is that higher-order charge states may be distributed through a longer propagation distance ($\sim$ 8 mm) compared to the case of 540 eV. This happens largely because Auger decay channels typically last more at 525 eV than at 540 (cf. sec. 4.3.1). But also, one can notice that the pulse is absorbed only four orders of magnitude ($I(L)/I(0) = 7.0 \times 10^{-4}$).

An estimation of the absorption length at 740 eV is $\approx$ 1.70 mm (see Tab. 4.2), which is almost twice the value of the absorption length at 540 eV. By looking at Fig. 4.15 (c) we notice that the perturbative regime begins at 10 mm (almost 6 times the absorption length). Thus, the ion yield curves remain flat for a longer propagation distance and even CO^{+13} can be produced (at 525 and 540 eV, CO^{+12} is the highest-order charge state that can be created). A good reason for this is that when using photons at 740 eV together with high intensities (see sec. 4.3.1) it is possible to suppress Auger decay events and instead sequentially photoionizing the sample, thereby getting the higher-charge states. However, according to Fig. 4.15 (d), the pulse intensity decreases almost four orders of magnitude ($I(L)/I(0) = 7.3 \times 10^{-4}$). This suggests that the x-ray pulse is producing high-order charge states in the medium while being poorly absorbed. Furthermore, we see that, although the absorption length at 525 eV is longer than at 740 eV, in the latter

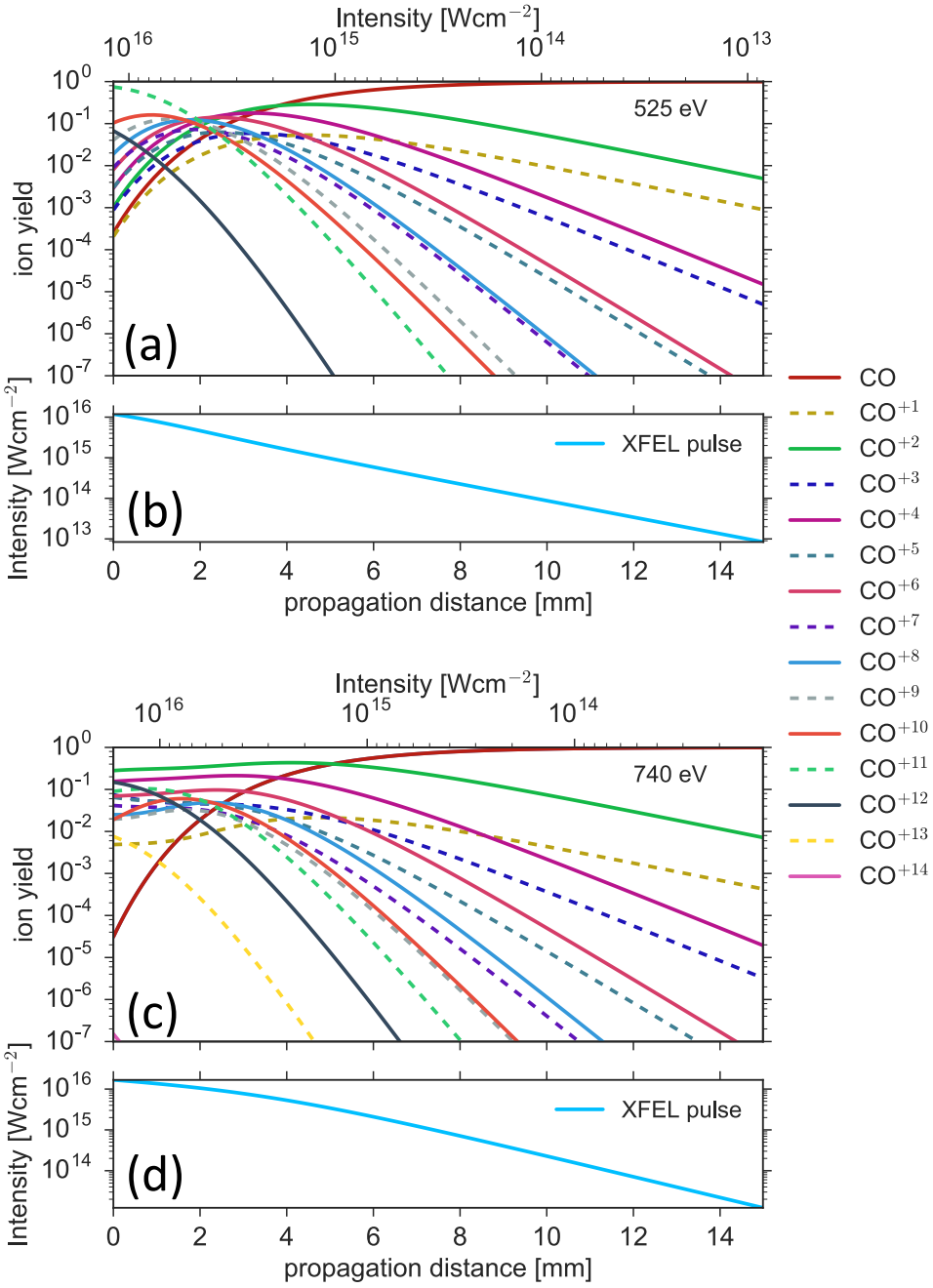

Figure 4.14: Spatial distribution of different charge state yields (a),(c) $Y^{+q}(z)$ (Eq.(4.6)) and (b),(d) spatial dependence of the XFEL pulse intensity along the gas medium. The pulse duration is set to 200 fs and the pulse carries a photon fluence of 2.0×10^{12} photons$\cdot\mu$m^{-2}. These parameters result in a peak intensity of (a)-(b) 1.1×10^{16} Wcm^{-2} for 525 eV and of (c)-(d) 1.6×10^{16} Wcm^{-2} for 740 eV.

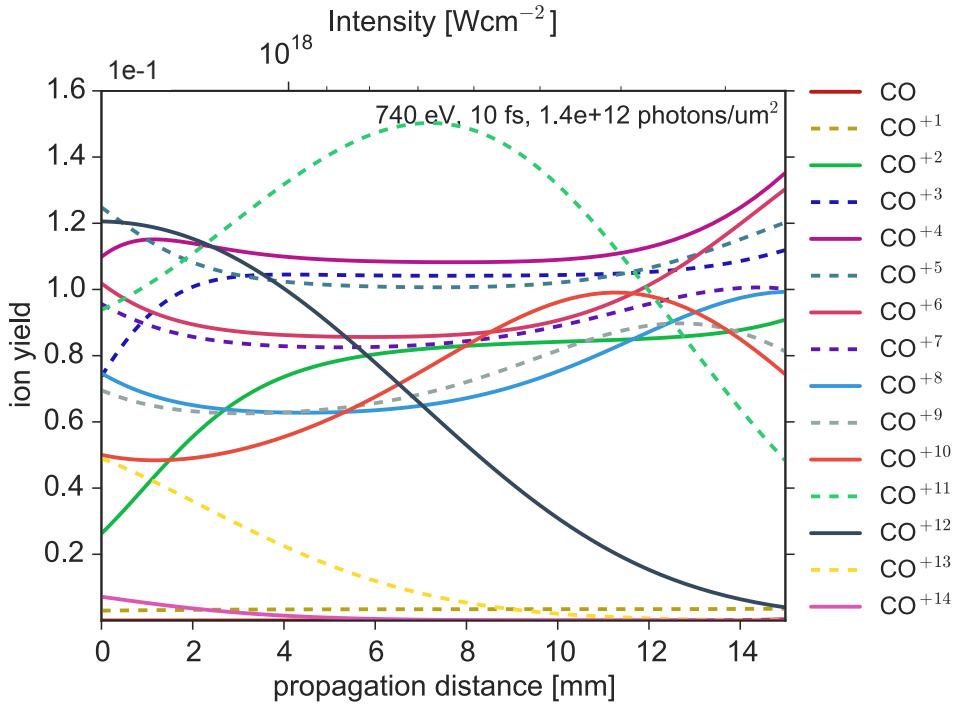

Figure 4.15: Spatial distribution of different charge state yields $Y^{+q}(z)$ (Eq.(4.6)) along the gas medium. According to the shown parameters, the incoming pulse has a peak intensity of 1.6×10^{18} Wcm^{-2}.

case the pulse is slightly more transmitted, reflecting the invalidity of Eq. (4.8) when employing ultra-intense pulses.

To finish off, we can analogously focus on the extreme case where higher intensities are used. In Figure 4.15 we consider a pulse with 740 eV as photon energy, a peak fluence of 1.4×10^{12} photons$\cdot\mu$m^{-2} and a temporal length of 10 fs, which results in a peak intensity of 1.6×10^{18} Wcm^{-2}. With such parameters, we see that the whole medium's length is a non-perturbative regime, due to the essentially null probability of finding CO in its neutral form. The effect that happens when the x-ray laser depletes all CO molecules is called *bleaching* or *saturable absorption* [86, 39, 33]. It will be discussed with more detail in the next section. The plot shows that the some charge state yields reach a plateau within a range of the propagation distance (e.g. CO^{+3},CO^{+5}, CO^{+7}), whereas other charge states are relatively more sensitive to the propagation distance, or in other words, to the attenuation of the pulse. Among the created charge states is CO^{+11}, which presents a maximum at 4 mm (two times the absorption length) with $Y^{+11} = 0.89$. Again, the counterintuitive fact is that, although the x-ray pulse causes too much electronic damage destroying all the molecules in its way, it is scarcely ab-

sorbed, since the intensity remains basically unaltered being $\sim 10^{18}$ Wcm^{-2} along the gas medium.

4.4 High-intensity absorption

The continuous attenuation of the pulse as it propagates along the medium is reflected on the charge state distribution, as we learned from the previous section. Since charge states are created in different amounts at each propagation distance z, the pulse will be absorbed differently too. In this section we study the transmission of the pulse together with the amount of absorbed photons by each of the created molecular ions by means of the absorption length (also referred to as optical depth).

The results presented in this section use the same parameters of last section 4.3.

4.4.1 X-ray beam transmission

Another observable that is experimentally accessible is the pulse transmission, which is defined as

$$T = \int_{-\infty}^{\infty} dt\; j(L,t) \Big/ \int_{-\infty}^{\infty} dt\; j(0,t) \tag{4.10}$$

Certainly, to compute this quantity the solutions to the coupled rate equations as well as to the evolution of the pulse as it propagates through the medium (Eq. (3.20)) are required. Still, one can have an idea with much less effort by approximating Eq. 4.10 by the Beer-Lambert law as

$$T(\omega) \approx \exp\left(-L/\lambda\right), \tag{4.11}$$

valid within the perturbative regime. In Eq. (4.11) λ is the absorption length (Eq. (4.8)) of neutral CO molecules in their ground state and $L = 15$ mm is the medium's length. The transmission for a x-ray pulse centered at 525, 540 and 740 eV calculated by Eq. (4.11) is displayed in Tab. 4.3

Figure 4.16 shows the transmission as a function of the peak intensity of the incident pulse for different pulse durations ($\tau = 10, 50, 100$ and 200 fs) and photon energies ($\hbar\omega = 525$, 540 and 740 eV). A first characteristic we should remark is that independently of the pulse duration and photon energy, the transmission has a minimum value which closely matches the transmission calculated by the Beer-Lambert law (cf. Tab. 4.3).

Table 4.3: Transmission of the x-ray beam according to Beer-Lambert law (Eq.4.11) for different photon energies. The density of the medium is $n_0 = 1.6 \times 10^{19}$ cm^{-3} and its length $L = 15$ mm.

Photon energy [eV]	Transmission (Beer-Lambert law)
525	8.8×10^{-4}
540	3.1×10^{-8}
740	1.4×10^{-4}

Let us analize Figs. 4.16 (a)-(b). We see that the transmission, for all the pulse durations, increases monotonically as the peak intensity grows. This is a fingerprint of the effect known as *intensity-induced transparency*, *saturable absorption* or *bleaching* [86, 39, 33]. In the present case, we observe saturable absorption as soon as all the neutral CO molecules are depleted, which happens primarily due to the absorption by $1s_O$ electrons. When electrons from the $(1s_O)$-shell are photo-ejected, the total cross section of the state $(1s_O)^{-1}$ decreases— until the inner-hole is replaced by a valence electron (within $\sim$ 13 fs) by means of an Auger decay (see section 4.3.1). Within the lifetime of the state $(1s_O)^{-1}$, photoionization probability is reduced and leads to saturable absorption for x-rays [39, 44, 40, 16, 33].

The dependence that transmission has upon the pulse duration is likewise evident. Figure 4.16 (a)-(b) shows that saturable absorption is less pronounced as shorter pulse durations are used. To understand such behavior, let us define the probability $\varrho_{n\to n'}$ that a molecule of configuration n is photoionized to produce the state n' within a time interval t as

$$\varrho_{n\to n'}(z,t;\omega) = \sigma_{n\to n'}(\omega) \int_0^t P_n(z,t')j(z,t')\, dt' \tag{4.12}$$

Likewise, the total the photoionization probability of a given configuration n equals

$$\varrho_n^{\text{tot}}(z,t;\omega) = \sigma_n^{\text{tot}}(\omega) \int_0^t P_n(z,t')j(z,t')\, dt' \tag{4.13}$$

Figure 4.17 shows the neutral CO photoabsorption probability (Eq. (4.13)) at position $z = 0.0$ mm using different peak intensities for a photon energy at 540 eV.

Saturable absorption sets in when the photoionization probability ϱ_n^{tot} reaches one; the time when all neutral CO turns into higher charge states. As the peak intensity increases, saturation is achieved faster. A peak intensity of 1.2×10^{16} Wcm^{-2} (dark red curve) allows saturable absorption to happen

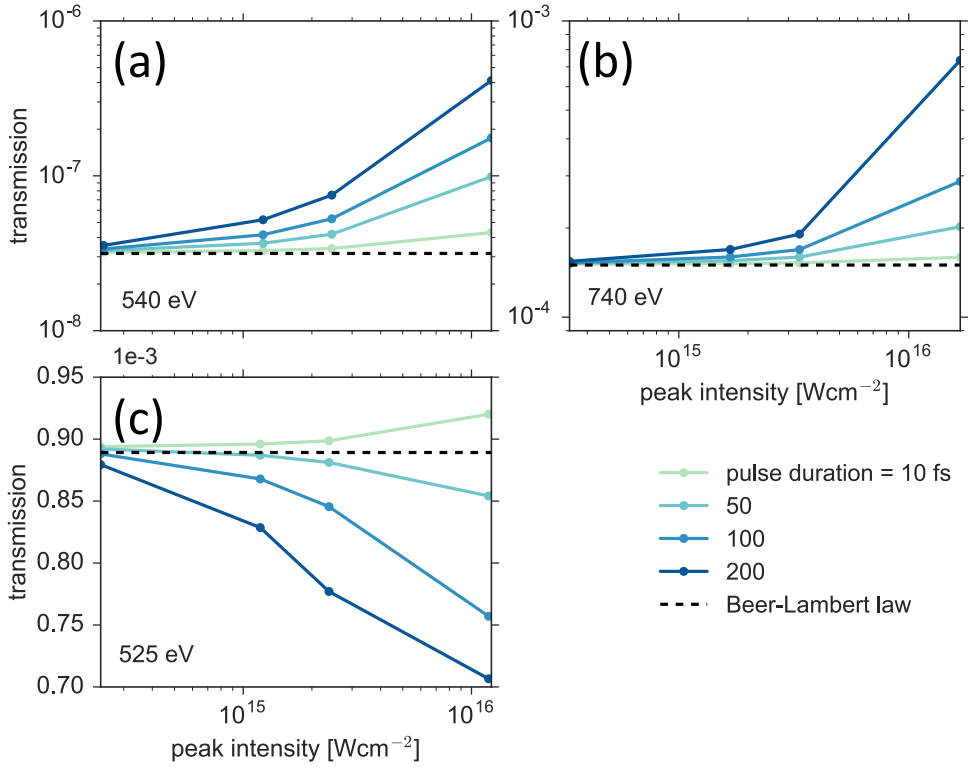

Figure 4.16: Transmission of incident pulse at (a) 540 eV, (b) 740 eV and (c) 525 eV for different pulse durations. The range of covered intensities corresponds to peak fluences ranging from 2.0×10^8 to 1.4×10^{10} photons·μm^{-2} for 10 fs, from 1.4×10^9 to 7.0×10^{10} photons·μm^{-2} for 50 fs, from 2.8×10^9 to 1.4×10^{11} photons·μm^{-2} for 100 fs, and from 5.6×10^9 to 2.8×10^{11} photons·μm^{-2} for 200 fs. The dotted line represents the transmission estimated using the Beer-Lambert law (Eq. 4.11).

within $\sim$ 75 fs. With the lowest intensity, which corresponds to 2.4×10^{14} Wcm^{-2} (yellow curve), even in a time of 200 fs saturation, i.e., flattening of the curves is not obtained. So, what Fig. 4.17 suggests is that for very short pulse durations, highest peak intensities are not going to give rise to saturable absorption whereas longer pulse durations (as discussed in section 4.3.2) permit a more efficient absorption of the pulse, enabling to trigger transparency. A similar argument holds for pulses at 740 eV.

At 525 eV is a completely different story. For instance, Fig. 4.16 shows that by increasing the pulse duration the x-ray pulse gets more absorbed. The effect is, however, very small ($\sim 10^{-5}$). One possible explanation for this may rely on the fact that lifetimes of the created ions are longer than ion lifetimes at 540 or 740 eV and that cross sections are typically larger at 525 eV (except for the $(1s_O)$ MO). So within the relatively long lifetimes, if sufficient photon flux is provided, the photoionization probability may reach the value of one

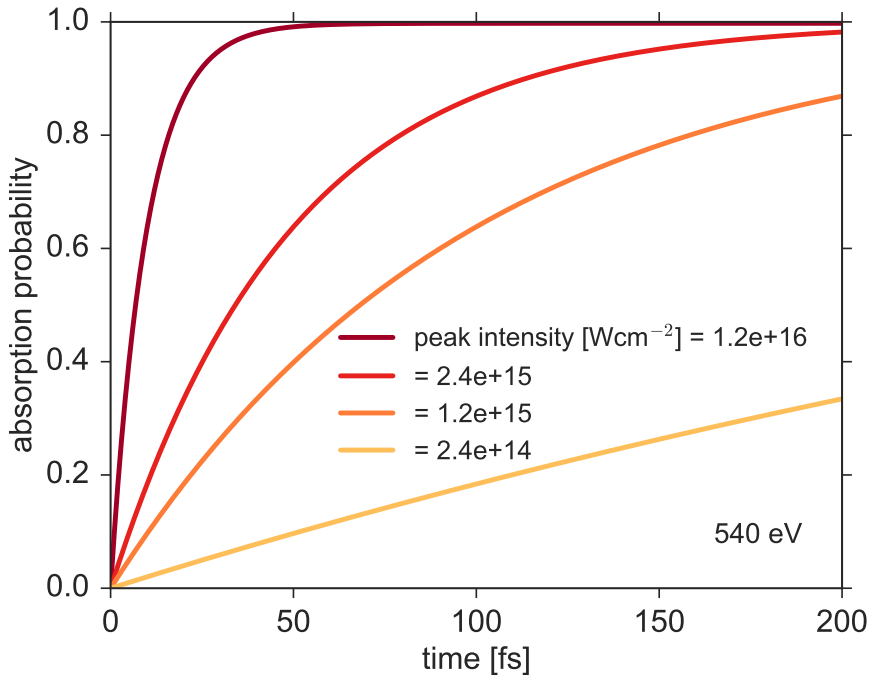

Figure 4.17: Photoionization probability ($\hbar\omega = 540$ eV) at $z = 0.0$ mm (Eq. (4.13)) of neutral CO in its ground state for different peak intensities corresponding to peak fluences ranging from 5.6×10^9 to 2.8×10^{11} photons$\cdot\mu$m^{-2}.

and thus overcome Auger decay and rather induce another photoionization event.

4.4.2 X-ray absorption length

The effect of saturable absorption is mostly dictated by the absorption of the XFEL pulse by neutral CO molecules. But the presence of the created charge states may eventually become important so that their effect on the attenuation of the pulse starts to be significant.

In order to account for the contribution of each of the produced charge states on the absorption of the pulse as it propagates, we would like to know the absorption length λ^{+q} of a given charge state $+q$. To do so, we first concentrate on the spatial-temporal average of the occupation probability of a certain configuration n given as

$$X_n = \frac{1}{\tau \cdot L} \int_0^L dz \int_0^\tau dt \; P_n(z,t) \tag{4.14}$$

This quantity tells what are the important configurations that transiently - meaning within the pulse duration τ- appear and might disappear again

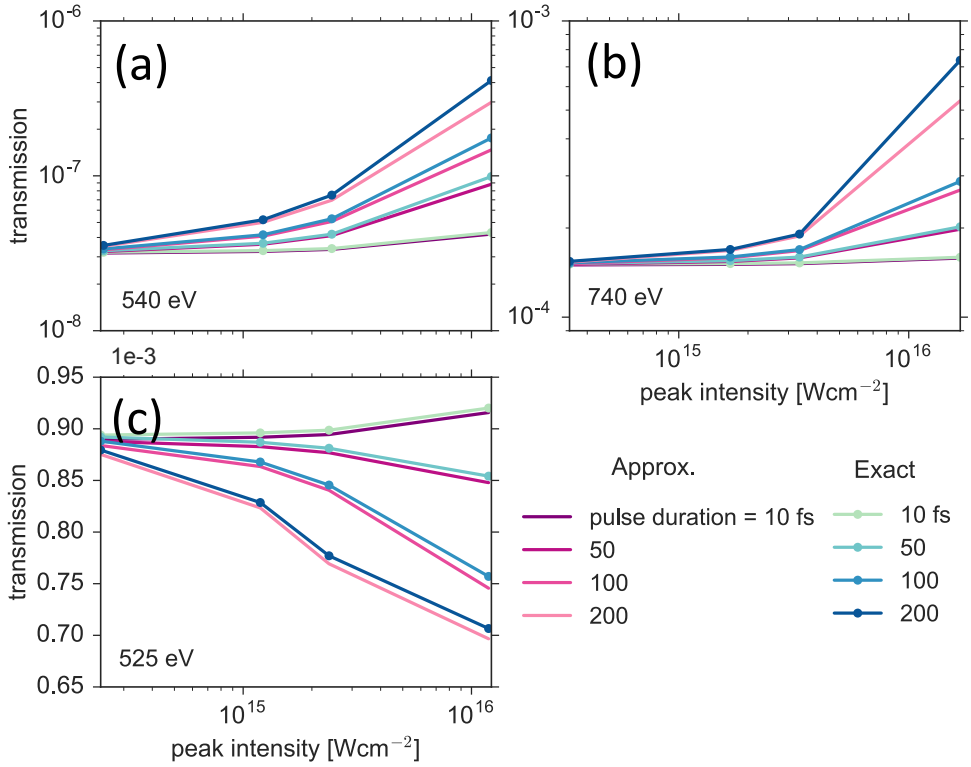

Figure 4.18: Comparion between the transmission calculated by Eq. 4.16) (Approx.) and by the exact formula Eq. (4.10) (Exact) at (a) 540 eV, (b) 740 eV and (c) 525 eV for different pulse durations. The range of covered intensities corresponds to peak fluences ranging from 2.0×10^8 to 1.4×10^{10} photons·μm^{-2} for 10 fs, from 1.4×10^9 to 7.0×10^{10} photons·μm^{-2} for 50 fs, from 2.8×10^9 to 1.4×10^{11} photons·μm^{-2} for 100 fs, and from 5.6×10^9 to 2.8×10^{11} photons·μm^{-2} for 200 fs.

in the interaction region of length L. Therewith, we define the effective absorption length of the charge state $+q$ as

$$\lambda^{+q}(\omega) = 1 \Big/ \left[n_0 \cdot \sum_{n \in S_{+q}} \sigma_n^{\text{tot}}(\omega) \cdot X_n \right] \tag{4.15}$$

where S_{+q} is the set of configurations with charge $+q$.

Let us see how this quantity (Eq. (4.15)) can actually provide information about the absorbtion of x-rays by each state. Since the medium consists -transiently- of a mixture of the created charge states, an estimate of the resulting transmission would be

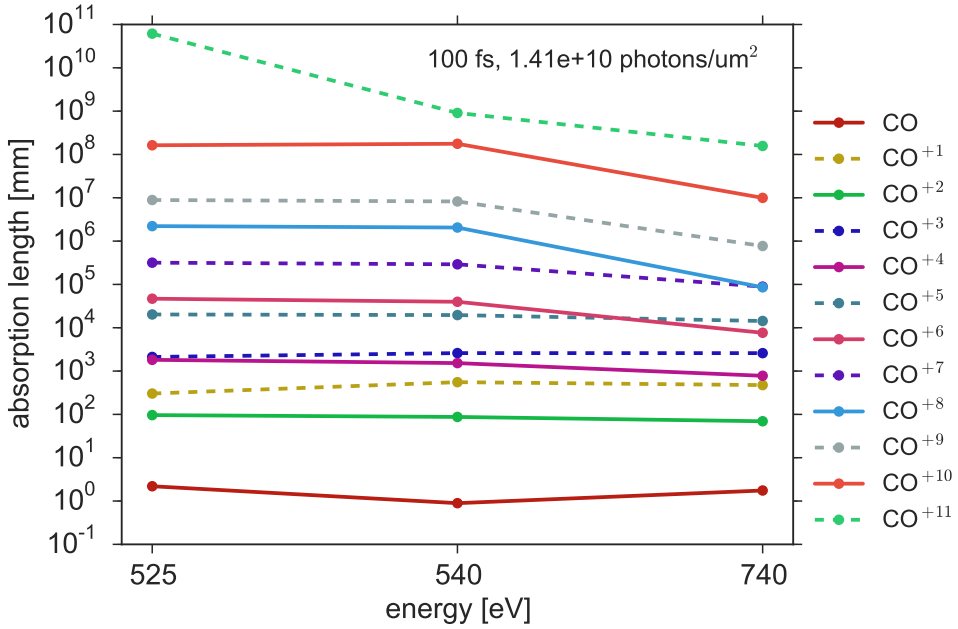

Figure 4.19: Absorption depth (Eq.(4.15)) of different charge states $0 \leq q \leq 14$ at various photon energies ($\hbar\omega = 525, 540$ and 740 eV). The employed peak intensities (within the perturbative regime) are 1.18×10^{15} Wcm^{-2} at 525 eV, 1.2×10^{15} Wcm^{-2} at 540 eV, and 1.67×10^{15} Wcm^{-2} at 740 eV. The density of the medium is set to $n_0 = 1.6 \times 10^{19}$ cm^{-3} and its length to $L = 15$ mm.

$$T(\omega) \approx \prod_q e^{-L/\lambda^{+q}(\omega)} \tag{4.16}$$

for $0 \leq q \leq 14$. Figure 4.18 shows the transmission calculated by Eq. (4.16) and by the full propagation Eq. (4.10) at 525, 540 and 740 eV for different pulse durations (τ = 10, 50, 100 and 200 fs). We find that such approximation gives a reasonable agreement with the transmission calculated by Eq.(4.10), having a relative error less than a 10% for peak intensities around 10^{15} Wcm^{-2} whereas less than 30% for peak intensities around 10^{16} Wcm^{-2} with respect to the original value. Similar relative errors are found with 525 eV and 740 eV.

Figure 4.19 shows the absorption depth λ^{+q} (Eq.(4.15)) using peak fluence of 1.4×10^{10} photons$\cdot\mu$m^{-2} and a pulse duration of 100. With the three different photon energies of 525, 540 and 740 eV, peak intensities are 1.18×10^{15}, 1.2×10^{15}, and 1.67×10^{15} Wcm^{-2}, respectively.

It should be remarked that the shortest absorption length corresponds to neutral CO at 540 eV and $\lambda^{+0}(525) > \lambda^{+0}(740)$. This is consistent with the fact that neutral CO absorbs more efficiently photons at 540 eV, than at 525

eV or at 740 eV. Moreover, in most of the created charge states absorption length at 525 eV and 540 eV appear to be almost of the same order of magnitude (except for CO^{+1}, where λ^{+1} slightly increases from 525 eV to 540 eV). This means that molecular ions absorb roughly the same amount of photons at these two photon energies.

On the other hand, one can see that at 740 eV absorption lengths are smaller for 525 eV and 540 eV. This reduction of ionic absorption lengths -meaning for $q \geq 1$- answers the question concerning why pulses centered at 740 eV cause more electronic damage, although they are less absorbed. What is found in all photon energies is that the longest absorption lengths correspond to the highest order charge states (since X_n gets smaller for high charge states).

The same plot shows that λ^{+2} remains barely unchanged under variation of the photon energy, and also is found to be the shortest ionic absorption length. The fact that λ^{+1} is larger than λ^{+2} (and by more than two orders of magnitude with respect to λ^{+0}) for all photon energies affects that $q = +1$ configurations are typically short-lived due to the Auger decay.

4.5 Conclusion

In section 4.3 the evolution in time of neutral CO and the created ions as they interact with the XFEL pulse was discussed. Looking at the temporal dependence of charge state and configuration probabilities one obtains an insight on the most probable ionization and relaxation channels, and thereby a picture of the predominant sequence of events during the pulse duration. At 540 eV, ionization of neutral CO involves mostly the ejection of electrons from the $1s_O$ MO, unlike at 525 eV, where electrons from $1s_C$ MO are most likely to be removed. In both cases the excited ion relaxes via the rapid Auger decay of valence electrons. Further ionization occurs through absorption by electrons from the $1s_C$ MO. Using 740 eV as photon energy and sufficient intensities $\sim 10^{17}$ Wcm^{-2} we are able to beat the relaxation time of CO^{+1} and a double core-hole on the oxygen side may be created in the process. On top of that, the ultra-intense pulse can lead to the destruction of the molecule by the expulsion of all its electrons before the pulse is over.

Ion yields, which represent the charge state population distribution long after the pulse has passed and which pave the path for comparison with experiments, provide information of the nonlinear interaction with the XFEL pulse. It is found that either by decreasing the pulse duration or reducing the peak fluence, production of lower-order charge states is favored, which implies a lower impact on the electronic structure. Whereas pulses with

increasing duration or higher peak fluences enable a much more efficient absorption, and thus electronic damage is more severe.

Then the attention is focused on the dominant mechanisms that drive such ionization-cascade and to the sequence of events that bring the neutral CO molecule up to a particular charge state. Either by looking into the temporal evolution of occupation probabilities or by implementing a power-law fit on the ion yields as a function of the pulse peak intensity, we deduce that ions are created by sequential inner-shell single-photon absorption followed by Auger decays. The consequence of this is that multi-photon absorption by ionic states of CO occurs within a single pulse. For instance, using a pulse with a 10 fs duration, production of CO^{+12} requires just the absorption of seven x-ray photons.

After examining the response of a single molecule to the XFEL radiation, the influence of the attenuation of the pulse as it propagates along the medium on the charge state spatial distribution, is a matter of concern. Simulations reveal that pulses with comparable durations and peak fluences but increasing photon energy induce more electronic damage and are poorly absorbed. The non-perturbative regime at 740 eV is found to be twice as long as at 540 eV, being the charge state CO^{+14} reachable with the former energy (at 525 eV the non-perturbative regime is the longest, but electronic damage is not too different as at 540 eV).

Motivated by this last observation, in section 4.4, the transmission of the incoming XFEL pulse is analyzed. Employing a gas density of 1.6×10^{19} cm^{-2} and a medium length of 15 mm, a transmission of $\sim 10^{-8}$ is obtained at 540 eV, whereas at 525 eV and 740 eV of $\sim 10^{-4}$. The effect of x-ray saturable absorption is introduced, which appears at the moment when neutral CO is severely depleted and leads ions that do not absorb as efficiently as the neutral molecule. In addition, the pulse transmission also gives an insight on the electronic damage caused on the sample, since for longer pulse durations a more pronounced reduction of the pulse absorption can be observed, meaning that there is sufficient time to ionize all neutral CO and thereby to achieve higher charge states.

At the end, we present an analysis on the contribution to the absorption of the pulse by some of the created ions, through the introduction of the absorption length of a specific charge state. It is found that CO^{+2} is the ion that most efficiently absorbs lying just after neutral CO. Absorption length shortens for the highest charge states, so they contribute less to the absorption of the pulse. The longer ionic absorption lengths correspond to photon energies at 540 and 525 eV.

Chapter 5

Pump-probe studies

5.1 Introduction

Understanding the electron motion in molecules following light-matter interaction plays a key role to unravel fundamental events in chemical reactions and many biological processes, such as energy transport in plants and DNA damage. Such ultrafast electronic motion typically takes place on femtosecond (10^{-15} s) to attosecond (10^{-18} s) timescales [87, 88]. Having experimental techniques able to temporally and spatially resolve the elementary steps of chemical reactions, may let us to understand under which conditions they occur and to access to their control [89].

Pump-probe methods, such as time-resolved spectroscopy, have been widely applied to study the ultrafast electron motion in atoms and molecules in the optical, infrared (IR), terahertz (THz), and most recently in the x-ray domain [90, 91, 92, 93, 94]. In this technique, typically an ultra-short laser pulse is split into two portions: a stronger beam (the pump), which excites the sample and induces structural changes, and a weaker beam (the probe), which monitors the dynamical evolution of the pump-induced changes. The electronic dynamical evolution is encoded in the optically induced changes of the electron density as a function of time, which can be measured, as for example by means of optical parameters (such as reflectivity or transmission [95]), photoelectron [96] or Auger electron energies [97] while varying the time delay between the arrival of pump and probe pulses.

The advancement of X-ray Free-Electrons Lasers (XFELs) and the achievable intensities open avenues to extend spectroscopic -and thereby pump-probe- techniques to the nonlinear regime and to study elementary excitations in matter. One of the simplest techniques is resonant inelastic x-ray scattering (RIXS), also referred to as resonant x-ray Raman scattering. RIXS is an element specific spectroscopic tool that is sensitive to electronic excitations. It has been applied on solids [98], liquids [99], gases [100] and even on stud-

ies of charge migration [101]. However, the recorded x-ray emission spectra usually offer a low-quality resolution. Such a problem can be overcome by stimulating the resonant x-ray Raman scattering and, consequently, coherently amplifying the outgoing signal [60].

Here, we briefly review an approach for stimulated RIXS suggested by V. Kimberg and N. Rohringer, 2016 [47] based on stochastic spectroscopy, that uses the full bandwidth of the incoming XFEL pulses by employing a combination of x-ray self-seeding [102, 103] and split undulator two-color schemes [104, 84]. Moreover, since stimulated RIXS (sRIXS) couples to the ionization continuum -intermediate levels in the process are core-excited autoionizing states- we study the background signal due to the absorption of molecular ions that are unavoidable produced during x-ray interaction. To this end, we extend the absorption model developed in chapter 3 to the present two-color scheme and study the transmission of pump and probe pulses together with the absorption length of the created charge states as a function of x-ray pulse peak intensity.

This chapter is organized as follows: section 5.2 is devoted to the introduction of the concept of RIXS and the two-color scheme for sRIXS. Then in section 5.3 the theoretical model for the absorption of the pump and probe pulses by the created molecular (CO) ions is outlined. Results are discussed in section 5.4. And, lastly, conclusions are presented in section 5.5.

5.2 Stimulated Resonant Inelastic X-ray Scattering

X-ray Raman scattering is a photon-in photon-out technique, where the incoming photon is inelastically scattered off the sample. The outgoing photon carries an energy ω_{out} equal to the difference between the incoming photon energy ω_{in} and the transition energy between the final and ground state ω_{f0} [78]

$$\omega_{\text{out}} = \omega_{\text{in}} - \omega_{\text{f0}} \tag{5.1}$$

In RIXS process core-electrons are resonantly excited to unoccupied valence orbitals. The core-excited intermediate state can either be subject to Auger decay or to an emission of a scattered red-shifted x-ray photon. The energy difference between the incoming photon energy and the outgoing photon energy is left in the system as an excitation -therefore probing unoccupied and occupied electronic states-, which for instance gives information on vibrational, electronic and elementary excitations in condensed matter systems [105, 106, 107]. Analogously to the amplification process of a laser beam [13], RIXS signal can be amplified several orders of magnitude by stimulating the scattering process at the beginning of an elongated medium.

One way to drive resonant Raman scattering is by using the impulsive Raman scheme, which consist on using a single pulse with a spectral bandwidth that covers the intermediate and final transitions. Such scheme was successfully applied on demonstrating stimulated Raman scattering in atomic neon [60] by stimulating the inelastic scattering process with the spectral tails of the relatively broad SASE pulses. Another more sophisticated scheme relies on providing a pump pulse that resonantly excites the system and a probe pulse centered at the specific electronic inelastic transition. The probe pulse then serves as seed in the stimulated scattering process. This last technique is often called the two-color stimulated RIXS (sRIXS) scheme.

The experimental demonstration of sRIXS in molecules would be a first step to assess the feasibility of high-resolution nonlinear spectroscopy at XFEL sources, thus, expanding the application of coherent pump-probe techniques to the x-ray domain.

5.2.1 Two-color stimulated RIXS scheme in CO

The usage of a two-color x-ray pulse scheme was proposed in CO in order to demonstrate sRIXS in molecular complexes. The concept of the experiment is schematically represented in Fig. 5.1. A pair of temporally overlapped SASE pulses within the usual SASE gain bandwidth (up to $\sigma_\omega \approx 0.1 - 1\%$) is used to stimulate resonant Raman scattering. The first pulse is centered at 534 eV and is intense enough $\sim 10^{16}$ Wcm^{-2} to efficiently pump CO on the $^1\Sigma_g \rightarrow^1 \Pi$ transition. The probe pulse, with peak intensities around 10^{14} Wcm^{-2}, has a central photon energy of 525 eV so that it overlaps with the inelastic transition $^1\Pi \rightarrow^1 \Sigma_u$ thereby serving as seed for the resonant x-ray scattering process. The experiment aims for pulse durations (FWHM) from 50 to 100 fs and to pulses focused to a spot size of a few μm. Typical experimental conditions allow to have sufficient molecular densities $\sim 10^{19}$ cm^{-3} in the interaction region which is about a few mm long.

The two-color pulses can be generated by a split-undulator currently supplied at XFEL facilities [104, 84]. The maximum color separation is limited to 2% of photon energy by the undulator strength parameter range; therefore enough energy separation can be achieved to provide photons at 534 eV and 525 eV. Resonant excitation of ground state CO to the $^1\Pi$ core-excited state requires a pump pulse with a very narrow bandwidth and wavelength stability. This issue can be solved by self-seeding the pump pulse [102, 103]. After a pulse is self-seeded it presents a narrower spectral bandwidth and a higher peak intensity.

An estimation of the output sRIXS signal is carried out by solving the equation of motion (Liouville-von Neumann equation) for the electronic and vibrational degrees of freedom taking into account the propagation of the pump-probe electric field. The calculated signal can then be compared with

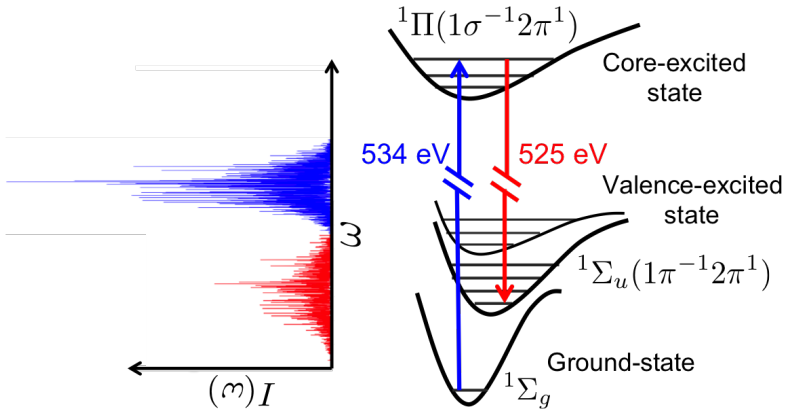

Figure 5.1: Level scheme of CO and two-color stimulated RIXS scheme driven by a pair of SASE pulses overlapped in time and separated by 9 eV. The pump field ($\omega = 534$ eV, blue color) is resonant to the intermediate core-excited state $^1\Pi$, the probe field ($\omega = 525$ eV, red color) stimulates the inelastic x-ray Raman scattering from the core-excited to the valence excited state $^1\Sigma_u$.

the standard 2D map -after a covariance analysis [60, 80]-, which displays the sRIXS spectrum as a function of the pump photon energy. However, typically the absorption bands of molecular ions produced by resonant Auger decay -the dominant decay process in the system- have a spectral overlap with regions, where stimulated Raman emission is expected. Molecular ions can therefore absorb the probe pulse and introduce absorption features in the transmitted spectra. This results in background that can mask the sRIXS.

5.3 Pump-probe absorption model

In order to study the background signal, we consider that the pump and probe pulses have central photon energies of $\omega_{\mathrm{d}} = 540$ eV and $\omega_{\mathrm{d}} = 525$ eV, respectively. Assuming equivalent XFEL beam characteristics as in chapter 3, we consider that the SASE pump-probe field propagates in the z-direction and is linearly polarized. Due to the relatively large energy separation of the two SASE components, the total electric field $E(z,t) = E_{\mathrm{p}}(z,t) + E_{\mathrm{d}}(z,t)$ is written as the contribution of the pump pulse electric field E_{p} and the probe pulse electric field E_{d}. Again, in a similar fashion as it was done in section 3.3, the electric field components are expanded in plane waves as (for $\mu = \mathrm{p}, \mathrm{d}$)

$$E_\mu(z,t) = \tilde{E}_\mu(z,t)e^{i(k_\mu z - \omega_\mu t)} + \mathrm{c.c}, \tag{5.2}$$

where c.c. refers to the complex conjugate and k_μ is the magnitude of the wave vector. Additionally, electric field components are treated in the slow-

varying envelope approximation. In such a way, the system of equations that describes the evolution of the molecular gas together with the propagation of the pump and probe photon fluxes j_μ is given by

$$\frac{\partial P_n}{\partial t} = \sum_{\mu} \sum_{n' \neq n}^{\text{all config.}} [P_{n'} \Gamma_{n \to n'}(\omega_\mu) - \Gamma_{n' \to n}(\omega_\mu) P_n] \tag{5.3}$$

$$\frac{\partial j_\text{p}}{\partial z} + \frac{1}{c} \frac{\partial j_\text{p}}{\partial t} = -n_0 \cdot \left[\sum_{n}^{\text{all config}} \sigma_n^{\text{tot}}(\omega_\text{p}) \cdot P_n \right] \cdot j_\text{p} \tag{5.4}$$

$$\frac{\partial j_\text{d}}{\partial z} + \frac{1}{c} \frac{\partial j_\text{d}}{\partial t} = -n_0 \cdot \left[\sum_{n}^{\text{all config}} \sigma_n^{\text{tot}}(\omega_\text{d}) \cdot P_n \right] \cdot j_\text{d} \tag{5.5}$$

where c is the speed of light in vacuum, P_n is the occupation probability of the molecule having the electronic configuration n, $\Gamma_{n \to n'}$ is the transition rate from the configuration n to the configuration n'. Transition rates can either be from a photoionization $\Gamma^P_{n \to n'}(z, t; \omega_\mu) = \sigma_{n \to n'}(\omega_\mu) j_\mu(z, t)$, Auger decay or fluorescent decay process. The quantity $\sigma_n^{\text{tot}}(\omega_\mu)$ stems for the total cross section (Eq. 3.16) for photoionizing a molecule with electronic configuration n with a photon of energy $\hbar\omega_\mu$. All together Eqs. (5.3)-(5.5) need to be solved in a self-consistent way.

5.4 Results and discussion

In this study, we assume that pump ($\omega_\text{p} = 540$ eV) and probe ($\omega_\text{d} = 525$ eV) pulses are temporally overlapping, have a flat-top temporal shape and the same pulse duration of $\tau = 50$ fs. Both pulses are focused to a circular spot radius of $r_0 = 1.5$ μm, which has an uniform intensity distribution and is constant as the pulses propagate along the medium. We vary the photon peak fluence from 1.4×10^9 to 3.3×10^{11} photons$\cdot\mu\text{m}^{-2}$ for the pump pulse and from 1.4×10^6 to 3.3×10^{10} photons$\cdot\mu\text{m}^{-2}$ for the probe pulse, which result in peak intensities ranging from 2.4×10^{14} to 5.7×10^{16} Wcm^{-2} and from 2.3×10^{11} to 5.5×10^{15} Wcm^{-2}, respectively. The molecular density is fixed to $n_0 = 1.6 \times 10^{19}$ cm^{-3} and the length of the interaction region to $L = 15$ mm.

5.4.1 X-ray transmission

Within the pump-probe scheme, the system is described by the Eqs. (5.3)-(5.5).

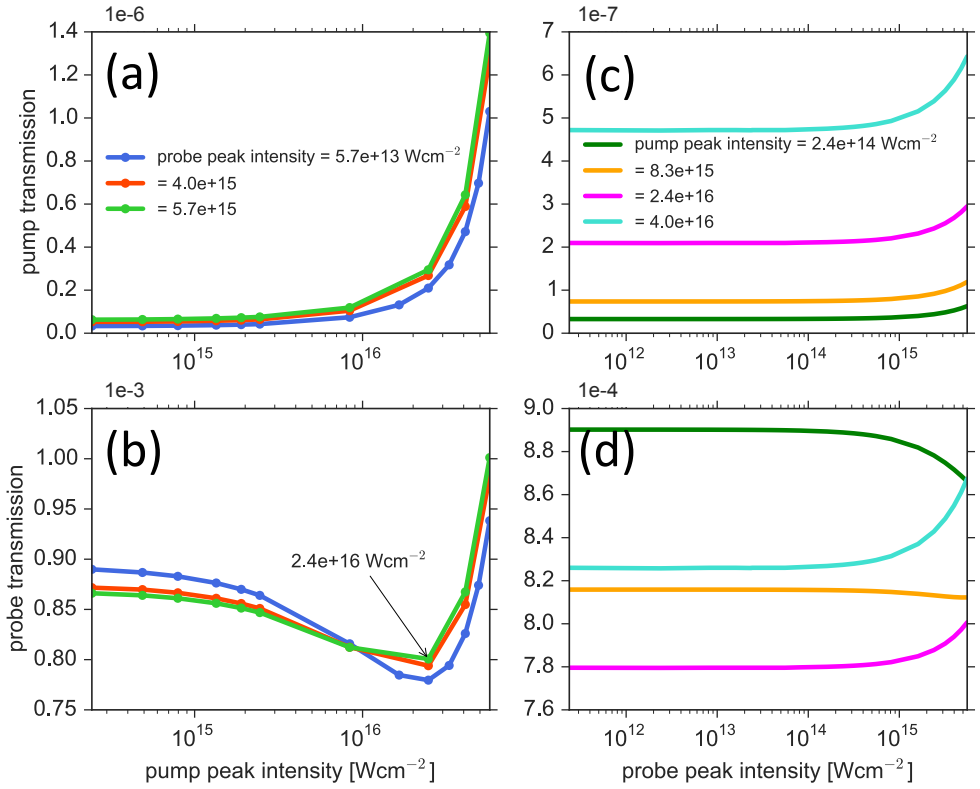

Figure 5.2: Transmission of pump pulse ($\omega_p = 540$ eV) and probe pulse ($\omega_d = 525$ eV) as a function of the (a)-(b) incoming pump peak intensity and (c)-(d) probe peak intensity. The pulse duration of both pulses is 50 fs. The range of covered intensities corresponds to peak fluences ranging from 1.4×10^9 to 3.3×10^{11} photons$\cdot\mu$m^{-2} for the pump pulse and from 1.4×10^6 to 3.3×10^{10} photons$\cdot\mu$m^{-2} for the probe pulse. The value 2.4×10^{16} Wcm^{-2} is the pump intensity for which the probe pulse is more absorbed.

In section 4.4 the dependence of the pulse transmission on the peak intensity was pointed out, which led to the effect of saturable absorption. In the current case, the transmission T_μ of the pump and probe pulses reads as $T_\mu = T_\mu(I_p, I_d)$, i.e., it is function of the pump peak intensity I_p and probe peak intensity I_d.

Figure 5.2 displays the transmission of the pump and probe pulses as a function of the pump peak intensity I_p and probe peak intensity I_d. In Fig. 5.2 (a) the pump transmission increases with growing pump peak intensities, which means that the pump pulse is subject to saturable absorption -regardless of the probe peak intensity- (see section 4.4). Contrastingly, Fig. 5.2 (b) shows that for pump peak intensities lower than a pump intensity of 2.4×10^{16} Wcm^{-2} the probe transmission decreases monotonically, suggesting that the pump field induces absorption of the probe field. This effect is,

however, quite small (about a 10% effect). At 2.4×10^{16} Wcm^{-2} the probe transmission reaches a minimum, and after this lowest value it suddenly rises and increases monotonically just as the pump transmission.

The transmission of the pump and probe pulses appears to be insensitive to probe peak intensity within the range $2.3 \times 10^{11} - 8.1 \times 10^{13}$ Wcm^{-2}, since it remains almost constant (Figs. 5.2 (c)-(d)) for these intensities. Within this regime, the Beer-Lambert law is valid for the probe field and, thus, the probe pulse does not make significant electronic damage on the sample. But with $I_{\mathrm{d}} > 8.1 \times 10^{13}$ Wcm^{-2} the pump transmission (Fig 5.2 (c)) gets off its constant value and increases, starting to deplete molecules of the medium. Note that the abruptness of such an increase relies on the pump peak intensity, being smoother for the lowest values. On the other way around, the dependence of the probe transmission upon the probe peak intensity for $I_{\mathrm{d}} > 8.1 \times 10^{13}$ Wcm^{-2} is even more complicated, as depicted by Fig 5.2 (d). For $I_{\mathrm{p}} \leq 2.4 \times 10^{16}$ Wcm^{-2} the probe transmission decreases with the highest probe peak intensities (green curve). If we increase the pump peak intensity, the probe transmission tends to straighten (orange curve) towards a constant value up to the point (for $I_{\mathrm{p}} > 2.4 \times 10^{16}$ Wcm^{-2}) where it shows saturable absorption with the highest probe peak intensities (violet and cyan curves). Such variable dependence therefore suggests that a balance between the peak intensity of the two colors can be tuned, so that the pump pulse induces an efficient absorption of the probe pulse while keeping the probe pulse to follow a Beer-Lambert's law exponential absorption within the whole probe peak intensity range.

Since the effective cross section $\sigma^{\mathrm{tot}}_{^1\Sigma_g}$ (Eq.(3.16)) of neutral CO in its ground state at 540 eV is about two times larger than at 525 eV, depletion of neutral CO molecules is achieved twice as fast with the pump pulse as with the probe pulse. Furthermore, as discussed in section 4.4.2, typically ions are more likely to absorb photons at 525 eV than photons at 540 eV (cf. Fig. 4.19). Thus, the reduction of the probe transmission for peak intensities $\leq 2.4 \times 10^{16}$ Wcm^{-2} (Fig. 5.2 (b)), may be due to the absorption of probe photons by long-lived charge states that were produced by the pump photons and which are efficiently populated as the pump peak intensity increases -as long as they are lower than 2.4×10^{16} Wcm-. Surpassing the pump intensity value of 2.4×10^{16} Wcm, charge states that most strongly absorbed photons at 525 eV are as well depleted leading to the increase in the probe transmission.

5.4.2 Background signal

In this section, we address the question of what are the molecular ions that could strongly contribute to the background signal in a sRIXS exposure. Our analysis is based on the absorption lengths (see section 4.4.2) of the different ions of CO produced during the interaction with the XFEL . The absorption

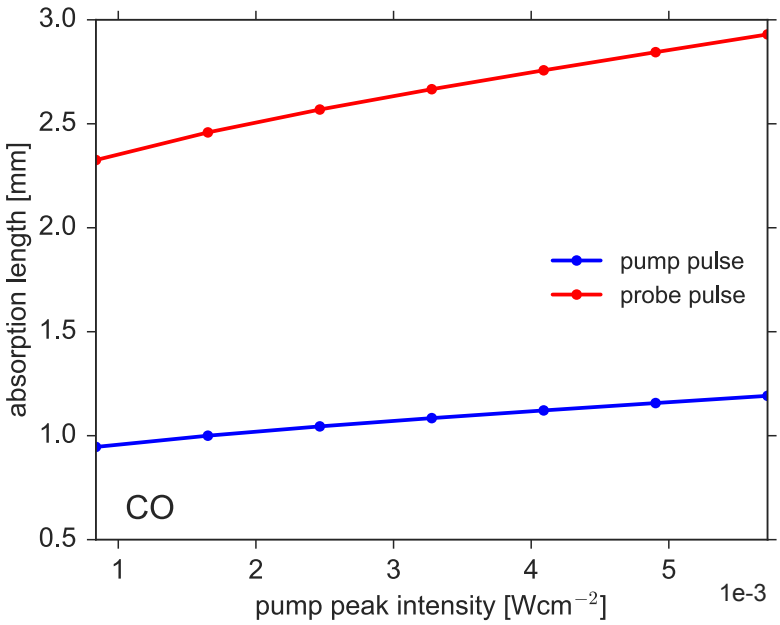

Figure 5.3: Absorption length (Eq.(5.6)) of CO by the pump ($\omega_p = 540$ eV; blue) and the probe ($\omega_d = 525$ eV; red) pulses for a medium of density $n_0 = 1.6 \times 10^{19}$ cm^{-3} and length $L = 15$ mm. The pulse duration for both pulses is 50 fs. The range of covered pump peak intensities (8.3×10^{15} to 5.7×10^{16} Wcm^{-2}) corresponds to peak fluences from 4.8×10^{10} to to 3.3×10^{11} photons·μm^{-2}. The probe peak fluence is fixed to 1.8×10^{9} photons·μm^{-2} (3.1×10^{11} Wcm^{-2}).

length $\lambda^{+q}(\omega_\mu)$ of the charge state CO^{+q} created with a photon of central energy ω_μ is defined as

$$\lambda^{+q}(\omega) = 1 \Big/ \left[n_0 \cdot \sum_{n \in S_{+q}} \sigma_n^{\text{tot}}(\omega) \cdot X_n \right] \tag{5.6}$$

where X_n is the spatio-temporal average of the occupation probability P_n and S_{+q} is the set of configurations with charge $+q$.

Figures 5.3-5.5 show the absorption lengths as a function the pump peak intensity of various molecular charge states $0 \leq q \leq 14$ created during the interaction with the two-color field. The photon fluence of the probe pulse is fixed to 1.8×10^{9} photons·μm^{-2} which results in a peak intensity of 3.1×10^{11} Wcm^{-2}. The photon fluence of the pump field runs from 4.8×10^{10} to to 3.3×10^{11} photons·μm^{-2} which yields peak intensities ranging from 8.3×10^{15} to 5.7×10^{16} Wcm^{-2}. One must notice that, according to Figs. 5.2 (c)-(d), similar absorption lengths should be obtained with different probe peak intensities as long as they lie within the range $\sim 10^{11}$ to 10^{15} Wcm^{-2} (where Beer-Lambert law is valid).

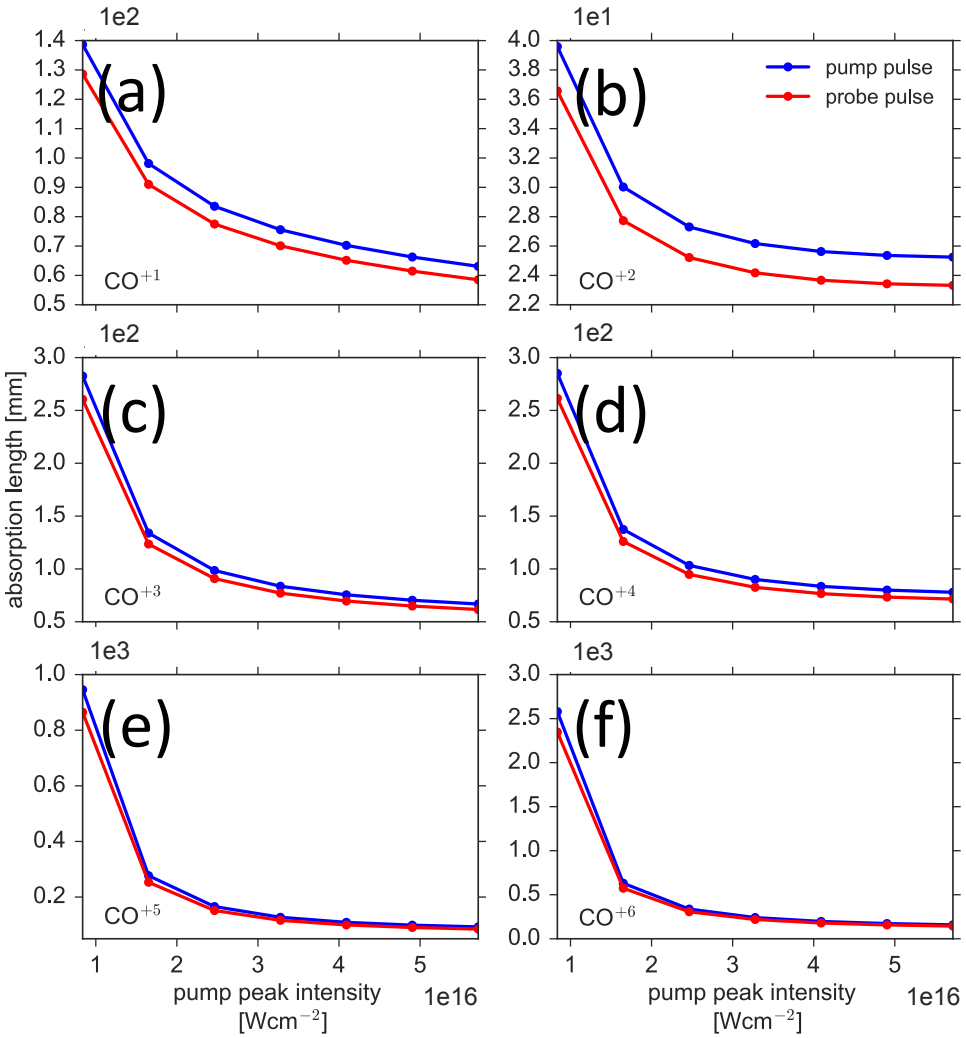

Figure 5.4: Absorption length (Eq.(5.6)) of different charge states $1 \leq q \leq 6$ created by the pump ($\omega_{\mathrm{p}} = 540$ eV; blue) and the probe ($\omega_{\mathrm{d}} = 525$ eV; red) pulses for a medium of density $n_0 = 1.6 \times 10^{19}$ cm^{-3} and length $L = 15$ mm. The pulse duration for both pulses is 50 fs. The range of covered pump peak intensities corresponds to peak fluences from 4.8×10^{10} to to 3.3×10^{11} photons·μm^{-2}. The probe peak fluence is fixed to 1.8×10^{9} photons·μm^{-2}.

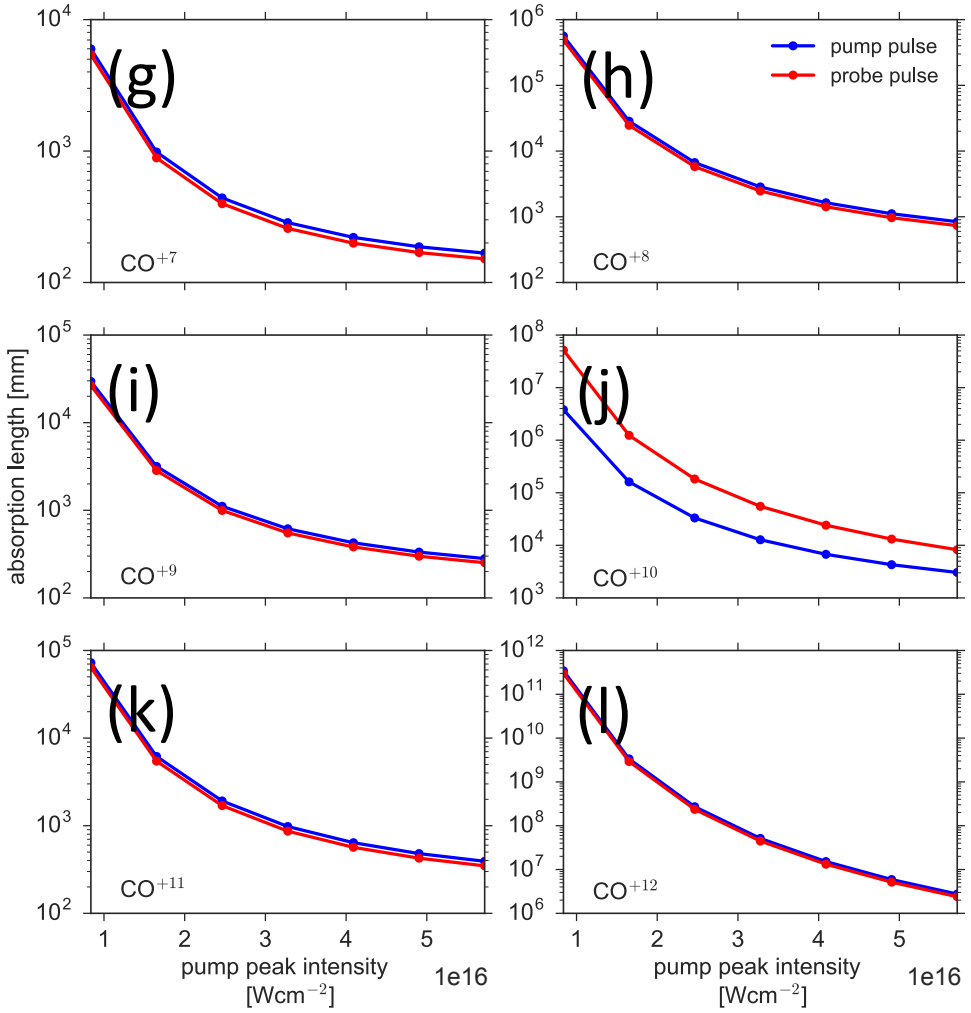

Figure 5.5: Absorption length (Eq.(5.6)) of different charge states $7 \leq q \leq 12$ created by (blue) the pump ($\omega_\mathrm{p} = 540$ eV) and (red) the probe ($\omega_\mathrm{d} = 525$ eV) pulses for a medium of density $n_0 = 1.6 \times 10^{19}$ cm^{-3} and length $L = 15$ mm. The pulse duration for both pulses is 50 fs. The range of covered pump peak intensities corresponds to peak fluences from 4.8×10^{10} to to 3.3×10^{11} photons$\cdot\mu$m^{-2}. The probe peak fluence is fixed to 1.8×10^{9} photons$\cdot\mu$m^{-2}.

It can be seen that neutral CO (Fig. 5.3) has the lowest absorption length when compared with the created ions for both the pump and probe pulses. The absorption length of the neutral molecule smoothly enlarges with increasing pump peak intensities -due to saturable absorption-. For higher-order ions, on the other hand, the absorption length drops monotically as the pump peak intensity rises. Starting at 1.6×10^{16} Wcm^{-2}, charge state production saturates and curves of most of the created ions merge and bend towards constant minimum values between $\sim 10^2 - 10^5$ mm. So at very high intensities all ions tend to strongly absorb the pump-probe field.

Within the scanned pump intensities, the ion CO^{+2} still remains as the one with the shortest absorption length-, so that this would be the ion that more contribute to the formation of the background signal. Furthermore, for lower-order charge states the absorption length of the probe field appears to be smaller, thus implying that the absorption features in the sRIXS spectra may mainly result from the interaction with the probe pulse.

5.5 Conclusion

We presented a model for non-resonant absorption by CO of two (pump-probe) temporally overlapped XFEL pulses centered at different photon energies. The aim is to study the background signal that could bias the detection of stimulated resonant Raman scattering (sRIXS) employing a recent proposed approach based on a two-color x-ray pulse scheme.

For this, in section 5.4.1, we concentrate on the transmission of the pump-probe field. The photon energy of the pump and probe pulses are assumed to be 540 and 525, respectively. Our theoretical model implies that the pump and probe transmissions are dependent on both pump and probe incoming peak intensities, I_p and I_d. Using pump peak intensities ranging from $\sim 10^{14}$ to 10^{16} Wcm^{-2} and probe intensities from 10^{11} to 10^{15} Wcm^{-2}, we find a transmission of the pump pulse of $\sim 10^{-7}$ and of the probe pulse of $\sim 10^{-4}$ for a medium of density $n_0 = 1.6 \times 10^{19}$ cm^{-3} and length $L = 15$ mm. The pump peak intensity shows x-ray saturable absorption over the range of probe peak intensities. Furthermore, there is a relatively large intensity regime of the probe pulse (from $I_d \approx 10^{12}$ to $\approx 10^{15}$ Wcm^{-2}) where the pump and probe transmissions remain basically constant. The impressive fact is that a pump intensity of 2.4×10^{16} Wcm^{-2} is found to determine the transmission of the probe pulse, i.e., for $I_p \leq 2.4 \times 10^{16}$ Wcm^{-2} the probe pulse gets more absorbed (reduction of transmission) whereas for $I_p > 2.4 \times 10^{16}$ Wcm^{-2} it gets more transmitted. This suggests that by tuning the pump peak intensity, the molecular gas can become either transparent or opaque to the probe pulse, although the latter effect is very small (around a 10% with respect to the transmission resulting from the lowest pump intensities). So,

since for sRIXS non-resonant absorption is not desired, either pump peak intensities far below or far above 2.4×10^{16} Wcm^{-2} should be used to avoid electronic damage on the sample.

Lastly, in section 5.4.2, we investigated the absorption length induced by the pump and probe pulses for the different created ions varying the pump peak intensity. Here, we find that CO^{+2} is the strongest absorber for all pump intensities. But also that for lower-order charge states the probe field is in fact the one that is more absorbed. Therefore, it may be the major contributor to the formation of the background signal in a sRIXS spectrum.

Chapter 6

Conclusions and Outlook

A detailed study of the interaction of ultra-intense and ultrafast x-rays with diatomic molecules is presented. Our theoretical approach is based on a molecular rate-equation model [34, 39, 35, 75, 38, 44]. The rate equations determine the time-dependent probabilities of all the energetically accessible involved electronic states by keeping track of the x-ray induced processes, such as photoionization, fluorescence decay and Auger decay. An extension of the model is implemented to molecular gases and the rate equations are coupled to the evolution of the XFEL photon flux, to account for the attenuation of the pulse as it propagates along the optically dense medium.

Carbon monoxide (CO) is chosen as the prototypical molecule. We numerically investigate the induced electronic structure response and high-intensity absorption in the molecular gas-phase target under the influence of a pulse delivered by an x-ray Free-Electron Laser (XFEL). The numerical simulations are carried out varying the XFEL pulse parameters, such as, photon energy, peak photon fluence and pulse duration. These stand on realistic experimental conditions, in principle available at current and future XFEL facilities.

It is found that CO under the influence of a focused XFEL beam interacts several times with a single x-ray pulse, by a sequence of inner-shell photoionization events followed by electronic Auger decay. Thereby high molecular charge states can be achieved. Within a few femtoseconds, the initially neutral gas of molecules evolves into plasma of molecular ions of a specific charge state and valence-excited state distribution. Our numerical calculations allow determining the charge state distribution and the occupation probabilities of the most dominant electronic states of the molecular ions, which can be then compared with the corresponding experimental quantities. Pulses with comparable energy but with decreasing duration show to increase the production of molecular ions with low charge, whereas with increasing duration leads to an efficient depletion of neutral CO molecules producing higher-order charge-states. Thus, variation of pulse duration and/or

peak photon fluence modulates the electronic damage caused on the sample. In the same fashion, we find that pulses with larger photon energies can also induce more electronic damage on the molecule.

At high x-ray intensities CO becomes quasi-transparent, owing to core-hole formation and to a reduction of the probability for further x-ray absorption. Such phenomenon is called saturable absorption, and is more pronounced for longer pulses. The contribution to the attenuation of the pulse by each of the created ions is also examined by means of the absorption length of a particular charge-state. The absorption length of molecular ions tends to shorten at photon energies far above the oxygen core-ionization threshold in comparison to absorption lengths at energies close to the threshold. By selectively choosing the photon energy, one can cause severe electronic damage and simultaneously induce a weak absorption of the x-ray pulse.

A simple model of non-resonant absorption for pump-probe experiments is introduced. It is assumed that the pump and probe pulses have photon energies centered slightly above and below the oxygen core-ionization threshold, respectively. Tuning the intensity of the pump pulse can significantly affect the transmission of the probe pulse. The probe transmission shows "induced opacity" in the low pump peak intensity regime and saturable absorption in the high intensity regime. The medium becomes opaque to the probe pulse, due to production of long-lived ions (by the pump pulse) that efficiently absorb probe photons.

We would like to point out that, although our molecular rate equation model may work very well for the chosen x-ray FEL pulses, more x-ray induced processes should be considered. For instance, simulations predict that for sufficient XFEL intensities all the electrons can be stripped out from the molecule without undergoing dissociation in the process, which certainly is an unrealistic situation. Shake-up and shake-off processes [108, 109], which happen due to the sudden contraction of molecular orbitals could play also an important role on electronic damage. Rate-equation models in atoms [33] implementing this effect have demonstrated to be more accurate to experimental observations. Secondary ionization in molecules (electron impact ionization) induced by photoelectrons and/or Auger electrons in the present approach is neglected [77, 38, 110], but may become crucial if the sample becomes dense and/or the molecular size becomes large. Nuclear dynamics, relativistic effects for heavy atoms, resonant excitation when photon energies approach to ionization edges are some other physical processes that are not being considered in our model.

On the other hand, our pump-probe studies were exclusively designed in order to figure out the optimal parameters of the pump-probe field, to record a good-quality spectrum for demonstrating stimulated resonant inelastic scattering in CO. The pump and probe pulses were overlapped in time. How-

ever, typical pump-probe experiments use a time delay between the pump and the probe pulse, so our model must be upgraded to consider this issue.

Appendix A

Numerical approaches to simulate XFEL pulse temporal envelopes

Listing A.1: Simulation of different temporal envelopes (gaussian, flat-top, SASE) for the xFEL pulse. The employed programming language is Python.

```
import numpy as np
import atomic_convert as au
from numpy.fft import fft, ifft, fftshift, ifftshift,
    fftfreq #libraries for fourier transform

#input parameters in: #photons, microns, fs, fs, eV
def pulse(ipulse,no_photons,focal_radius,
   pulse_duration,time_step,laser_bandwidth):

    nph = no_photons
    rfocus_au =au.space_au(focal_radius)/1.0e6
    #in micron to a.u.
    taup_au = au.time_au(pulse_duration)/1.0e15
    #in fs to a.u.
    dt_au = au.time_au(time_step)/1.0e15
    #in fs. to a.u.
    bandwidth_au = au.energy_au(laser_bandwidth)
     #in eV to a.u.
    tcut_au = 4.0*au.time_au(pulse_duration)/1.0e15
     #in fs to a.u.

     #temporal frame for moving window
    ncut = int(4.0*pulse_duration/time_step)        #
       temporal steps in moving window
    t = np.linspace(0.0,tcut_au,ncut)
```

```
    if ipulse == 'gaussian':
        mean = 2.0*taup_au
        sigma = taup_au/(2.0*np.sqrt(2.0*np.log(2.0))
           )
        fluxfactor = nph/(rfocus_au**2*np.pi*sigma*np
           .sqrt(2.0*np.pi))
        pp = np.exp(-(t-mean)**2/(2.0*sigma**2))*
           fluxfactor

    elif ipulse == 'flattop':
        tramp_au = au.time_au(3.0)/1.0e15  #3 fs ramp
            on/off for flattop pulse
        shiftin = tramp_au
        shiftout = tramp_au+taup_au
        sigma = (0.50/2.42e-2)/(2.0*np.sqrt(2.0*np.
           log(2.0)))
        fluxfactor = nph/(rfocus_au**2*np.pi)
        pp = []
        for it in t:
            if it <= shiftin:
                pp.append(np.exp(-(it-shiftin)
                   **2/(2.0*sigma**2)))
            elif it >= shiftout:
                pp.append(np.exp(-(it-shiftout)
                   **2/(2.0*sigma**2)))
            else:
                pp.append(1.0)
        intpulse = np.trapz(pp,dx=dt_au,axis=0)
        pp = np.array(pp)*fluxfactor/intpulse

    elif ipulse == 'SASE':
        mean = 2.0*taup_au
        freq = fftfreq(ncut, dt_au)*2.0*np.pi  #
           Fourier transform to frequency domain
        sigma = np.exp(-freq**2/(2.0*bandwidth_au**2)
           )
        fluxfactor = nph / (rfocus_au**2*np.pi)
        ak = np.sqrt(sigma)*(np.random.normal(size=
           ncut) +
        1j*np.random.normal(size=ncut))  # complex
           Fourier coefficients Ak modeled by
           Gaussian random numbers
        at = fftshift(ifft(ak))  #Fourier transfrom
           to time domain
```

```
        mask = np.exp(-(t-mean)**2 / (2.0*taup_au**2)
           ) #Gaussian mask
        pp = at*mask
        pp = np.abs(pp)**2
        intpulse = np.sum(pp*dt_au)
        pp *= fluxfactor / intpulse

    return pp
```

Appendix B

Calculated x-ray photoionization cross sections and rates of CO

All the values shown in this appendix were calculated by `XMOLECULE` *toolkit using the equations displayed in section 2.6. For a more detailed discussion on* `XMOLECULE` *toolkit, refer to the following publication:*

Yajiang Hao, Ludger Inhester, Kota Hanasaki, Sang-Kil Son and Robin Santra.

"Efficient electronic structure calculation for molecular ionization dynamics at high x-ray intensity",

Structural Dynamics, **2**, *041707 (2015)*

Table B.1: X-ray absorption cross section (σ) for various configurations of CO at 525, 540 and 740 eV.

		σ [10^{-4} a.u.] at 525 eV			σ [10^{-4} a.u.] at 540 eV			σ [10^{-4} a.u.] at 740 eV		
Charge	Configuration	$1s_O$	$1s_C$	1σ	$1s_O$	$1s_C$	1σ	$1s_O$	$1s_C$	1σ
+ 0	$^1\Sigma_g$	-	88.79	5.80	159.85	82.51	5.44	89.07	35.51	2.59
+1	$(1s_O)^{-1}$	-	98.82	7.04	-	91.59	7.04	46.72	38.40	7.04
	$(1s_C)^{-1}$	-	49.55	5.97	-	46.06	5.57	98.03	19.85	2.58
	$(3\sigma)^{-1}$	-	101.63	6.14	-	94.12	5.78	96.36	39.19	2.69
+2	$(1\pi)^{-2}$	-	111.91	7.60	-	103.40	7.08	106.79	42.04	3.18
	$(3\sigma)^{-2}$	-	116.73	6.63	-	107.72	6.18	104.33	43.32	2.82
	$(1\pi)^{-1}(3\sigma)^{-1}$	-	115.16	6.84	-	106.31	6.38	104.73	42.91	2.89
	$(2\sigma)^{-1}(1\pi)^{-1}$	-	112.21	7.75	-	103.67	7.23	106.93	42.12	3.26
	$(1\sigma)^{-1}(2\sigma)^{-1}$	-	115.14	3.70	-	106.30	3.45	107.44	42.91	1.54
+3	$(1s_C)^{-1}(3\sigma)^{-2}$	-	66.24	7.04	-	61.10	7.04	118.63	24.49	2.87
	$(1s_C)^{-1}(1\pi)^{-2}$	-	65.05	7.34	-	60.04	6.81	120.30	24.19	2.96
	$(1\pi)^{-1}(3\sigma)^{-2}$	-	133.12	7.28	-	122.42	6.77	113.21	47.60	2.99
	$(1s_O)^{-1}(1\pi)^{-2}$	-	124.70	10.36	-	114.89	9.64	58.85	45.45	4.28
	$(1s_O)^{-1}(1\sigma)^{-1}(2\sigma)^{-1}$	-	127.47	4.88	-	117.38	4.54	57.74	46.17	2.02
+4	$(1\pi)^{-2}(3\sigma)^{-2}$	-	151.84	8.28	-	139.14	7.67	123.85	52.27	3.28
	$(1\pi)^{-3}(3\sigma)^{-1}$	-	145.94	9.72	-	133.90	8.99	129.02	50.85	3.79
	$(1\sigma)^{-1}(1\pi)^{-2}(3\sigma)^{-1}$	-	149.98	4.72	-	137.50	4.36	129.35	51.85	1.82
	$(2\sigma)^{-1}(1\pi)^{-2}(3\sigma)^{-1}$	-	146.66	9.73	-	134.53	9.01	128.78	51.02	3.82
	$(1\sigma)^{-1}(2\sigma)^{-1}(1\pi)^{-2}$	-	141.26	5.68	-	129.74	5.25	136.05	49.71	2.17

Table B.2: X-ray absorption cross section (σ) for various configurations of CO at 525, 540 and 740 eV.

		σ [10^{-4} a.u.] at 525 eV			σ [10^{-4} a.u.] at 540 eV			σ [10^{-4} a.u.] at 740 eV		
Charge	Configuration	$1s_O$	$1s_C$	1σ	$1s_O$	$1s_C$	1σ	$1s_O$	$1s_C$	1σ
+ 5	$(1\pi)^{-3}(3\sigma)^{-2}$	-	172.06	10.15	-	157.11	9.36	138.81	57.09	3.89
	$(1s_C)^{-1}(1\pi)^{-2}(3\sigma)^{-2}$	-	89.82	8.43	-	82.08	7.78	145.55	30.35	3.19
	$(1\sigma)^{-1}(2\sigma)^{-2}(3\sigma)^{-2}$	-	180.25	4.78	-	85.75	4.40	71.21	31.32	1.81
	$(1s_O)^{-1}(1s_C)^{-1}(1\sigma)^{-1}(3\sigma)^{-2}$	-	93.96	4.77	-	85.75	4.40	71.21	31.32	1.81
+6	$(1\pi)^{-4}(3\sigma)^{-2}$	-	193.42	13.14	-	176.03	12.06	160.73	61.97	4.71
	$(2\sigma)^{-2}(1\pi)^{-2}(3\sigma)^{-2}$	-	195.25	12.98	-	177.62	11.93	158.94	62.34	4.73
	$(1\sigma)^{-2}(1\pi)^{-2}(3\sigma)^{-2}$	-	203.31	-	-	184.79	-	162.41	64.19	-
	$(1\sigma)^{-1}(1\pi)^{-3}(3\sigma)^{-2}$	-	198.72	6.48	-	180.72	5.94	161.14	63.16	2.30
	$(1\sigma)^{-1}(2\sigma)^{-1}(1\pi)^{-2}(3\sigma)^{-2}$	-	201.10	6.33	-	182.80	5.81	159.39	63.66	2.27
+7	$(2\sigma)^{-1}(1\pi)^{-4}(3\sigma)^{-2}$	-	217.20	17.02	-	196.98	15.55	189.72	67.15	5.79
	$(1\sigma)^{-1}(2\sigma)^{-1}(1\pi)^{-4}$	-	168.55	8.97	-	154.07	8.21	187.46	56.38	3.10
	$(1s_C)^{-1}(2\sigma)^{-1}(1\pi)^{-3}(3\sigma)^{-2}$	-	125.62	10.97	-	113.27	10.03	185.17	37.99	3.81
	$(1s_O)^{-1}(2\sigma)^{-1}(1\pi)^{-3}(3\sigma)^{-2}$	-	219.66	19.67	-	199.14	18.00	100.82	67.67	6.84
+8	$(1s_O)^2(1s_C)^2(1\sigma)^1(1\pi)^1$	-	-	11.65	-	-	10.58	223.77	-	3.80
	$(1s_O)^2(1s_C)^2(1\sigma)^2$	-	149.96	6.76	-	133.98	6.14	217.98	42.57	2.20
	$(1s_O)^2(1\sigma)^2(2\sigma)^1(1\pi)^1$	-	249.42	10.98	-	225.23	9.96	232.16	73.85	3.49
	$(1s_O)^2(1s_C)^1(1\sigma)^1(2\sigma)^1(1\pi)^1$	-	241.22	21.73	-	218.05	19.73	232.06	72.18	6.98
+9	$(1s_O)^2(1s_C)^2(1\sigma)^1$	-	277.01	13.82	-	249.31	12.44	280.63	79.35	4.08
	$(1s_O)^2(1s_C)^1(1\sigma)^2$	-	171.79	17.50	-	151.92	15.82	262.11	46.01	5.41
	$(1s_O)^2(1\sigma)^1(2\sigma)^1(1\pi)^1$	-	-	6.92	-	-	6.25	263.37	-	2.11
	$(1s_O)^2(1s_C)^1(1\sigma)^1(1\pi)^1$	-	181.86	8.63	-	160.03	7.79	258.84	47.61	2.64
	$(1s_O)^2(1s_C)^1(1\sigma)^1(2\sigma)^1$	-	173.89	8.82	-	153.76	7.96	263.03	46.56	2.68

Table B.3: X-ray absorption cross section (σ) for various configurations of CO at 525, 540 and 740 eV.

		σ [10^{-4} a.u.] at 525 eV			σ [10^{-4} a.u.] at 540 eV			σ [10^{-4} a.u.] at 740 eV		
Charge	Configuration	$1s_O$	$1s_C$	1σ	$1s_O$	$1s_C$	1σ	$1s_O$	$1s_C$	1σ
+ 10	$(1s_O)^2(1s_C)^2$	-	319.45	-	-	286.46	-	-	87.40	-
	$(1s_O)^2(1\sigma)^2$	-	-	14.70	-	-	13.19	-	-	4.26
	$(1s_O)^2(1s_C)^1(1\sigma)^1$	-	210.82	11.32	-	182.31	10.14	-	51.57	3.22
	$(1s_O)^1(1s_C)^1(1\sigma)^2$	-	203.98	30.99	-	177.30	27.78	-	50.73	8.80
+11	$(1s_O)^2(1\sigma)^1$	-	-	9.02	-	-	8.02	-	-	2.42
	$(1s_O)^2(1s_C)^1$	-	-	-	-	223.46	-	-	57.56	-
+12	$(1s_O)^2$	-	-	-	-	-	-	-	-	-
	$(1s_C)^2$	-	410.01	-	-	360.08	-	-	102.94	-
	$(1s_O)^1(1s_C)^1$	-	-	-	-	-	-	-	62.59	-
+13	$(1s_O)^1$	-	-	-	-	-	-	-	-	-
	$(1s_C)^1$	-	-	-	-	-	-	-	682.22	-

Table B.4: Auger rates (Γ^A) and fluorescence rates (Γ^F) for various configurations of carbon monoxide (CO).

		Γ^A [10^{-3} a.u.]		Γ^F [10^{-6} a.u.]	
Charge	Configuration	$(1s_O) \rightarrow (1\pi)(1\pi)$	$(1s_C) \rightarrow (3\sigma)(3\sigma)$	$(1s_C) \rightarrow (3\sigma)$	$(1s_O) \rightarrow (3\sigma)$
+ 1	$(1s_O)^{-1}$	1.82	-	-	3.76
	$(1s_C)^{-1}$	0.21	0.68	3.01	-
+2	$(1s_O)^{-2}$	8.29	-	-	7.24
	$(1s_C)^{-2}$	-	2.40	-	9.92
	$(1s_O)^{-1}(1s_C)^{-1}$	1.55	0.72	3.32	2.29
+3	$(1s_C)^{-1}(1\pi)^{-2}$	-	0.88	2.16	-
	$(1s_O)^{-2}(1\pi)^{-1}$	-	2.50	9.21	-
	$(1s_O)^{-2}(1s_C)^{-1}$	7.44	0.80	8.16	1.48
	$(1s_O)^{-1}(1s_C)^{-1}(1\pi)^{-1}$	-	0.83	3.35	1.74
+4	$(1s_O)^{-2}(1s_C)^{-2}$	6.23	2.45	5.54	6.94
	$(1s_C)^{-2}(1\pi)^{-2}$	-	2.61	8.37	-
	$(1s_O)^{-1}(1s_C)^{-1}(1\pi)^{-1}(3\sigma)^{-1}$	-	-	1.22	1.50
+5	$(1s_O)^{-2}(1s_C)^{-2}(1\sigma)^{-1}$	6.76	2.52	2.59	14.64
	$(1s_O)^{-1}(1s_C)^{-1}(1\pi)^{-2}(3\sigma)^{-1}$	0.38	-	0.74	1.72
+6	$(1s_O)^{-2}(1s_C)^{-2}(1\sigma)^{-2}$	7.12	2.00	0.52	30.84
	$(1s_O)^{-2}(1s_C)^{-2}(1\sigma)^{-1}(2\sigma)^{-1}$	8.07	3.10	0.46	16.86
+7	$(1s_O)^{-2}(1s_C)^{-2}(1\sigma)^{-2}(2\sigma)^{-1}$	7.39	2.04	0.63	44.29

Table B.5: Auger rates (Γ^A) and fluorescence rates (Γ^F) for various configurations of carbon monoxide (CO).

		Γ^A [10^{-3} a.u.]		Γ^F [10^{-6} a.u.]	
Charge	Configuration	$(1s_O) \rightarrow (1\pi)(1\pi)$	$(1s_C) \rightarrow (3\sigma)(3\sigma)$	$(1s_C) \rightarrow (3\sigma)$	$(1s_O) \rightarrow (3\sigma)$
+ 8	$(1\pi)^4(3\sigma)^2$	9.38	2.76	8.95	40.59
+9	$(1\pi)^3(3\sigma)^2$	5.40	4.04	16.12	20.06
	$(1s_C)^1(1\pi)^3(3\sigma)^1$	5.48	-	2.50	7.08
+10	$(1s_O)^2(3\sigma)^2$	-	1.68	1.44	-
	$(1s_O)^1(1s_C)^1(3\sigma)^2$	-	1.96	5.15	4.34
+11	$(1s_C)^1(3\sigma)^2$	-	5.34	17.56	6.28
+12	$(3\sigma)^2$	-	4.36	17.34	7.76
	$(1s_O)^1(3\sigma)^1$	-	-	9.41	4.27
+13	$(3\sigma)^1$	-	-	9.42	4.43

Bibliography

[1] S. E, *From X-Rays to Quarks*. New York: Dover, 2007.

[2] D. W. Turner and M. I. A. Jobory, "Determination of ionization potentials by photoelectron energy measurement," *The Journal of Chemical Physics*, vol. 37, no. 12, 1962.

[3] T. Carlson, *Photoelectron and Auger Spectroscopy*. New York: Plenum Press, 1975.

[4] P. G. Harris and R. Jenkins, "X-ray fluorescence spectroscopy," *Applied Organometallic Chemistry*, vol. 14, no. 1, pp. 76–76, 2000.

[5] R. Santra, "Phd tutorial: Concepts in x-ray physics," *J. Phys. B:At.Mol.Opt.Phys.*, vol. 42, no. 023001, p. 16, 2009.

[6] E. F. Garman, "Developments in x-ray crystallographic structure determination of biological macromolecules," *Science*, vol. 343, no. 6175, pp. 1102–1108, 2014.

[7] D. Attwood, *Soft X-Rays and Extreme Ultraviolet Radiation: Principles and Applications*. Cambridge University Press, 2007.

[8] B. W. J. McNeil and N. R. Thompson, "X-ray free-electron lasers," *Nat Photon*, vol. 4, pp. 814–821, 12 2010.

[9] C. Pellegrini, "The history of x-ray free-electron lasers," *The European Physical Journal H*, vol. 37, no. 5, pp. 659–708, 2012.

[10] K. J. Gaffney and H. N. Chapman, "Imaging atomic structure and dynamics with ultrafast x-ray scattering," *Science*, vol. 316, no. 5830, pp. 1444–1448, 2007.

[11] R. Neutze, R. Wouts, D. van der Spoel, E. Weckert, and J. Hajdu, "Potential for biomolecular imaging with femtosecond x-ray pulses," *Nature*, vol. 406, pp. 752–757, 08 2000.

[12] M. M. Seibert *et al.*, "Single mimivirus particles intercepted and imaged with an x-ray laser," *Nature*, vol. 470, pp. 78–81, 02 2011.

[13] N. Rohringer, D. Ryan, R. A. London, M. Purvis, F. Albert, J. Dunn, J. D. Bozek, C. Bostedt, A. Graf, R. Hill, S. P. Hau-Riege, and J. J. Rocca, "Atomic inner-shell x-ray laser at 1.46 nanometres pumped by an x-ray free-electron laser," *Nature*, vol. 481, pp. 488–491, 01 2012.

[14] S. M. Vinko *et al.*, "Creation and diagnosis of a solid-density plasma with an x-ray free-electron laser," *Nature*, vol. 482, pp. 59–62, 02 2012.

[15] R. W. Lee *et al.*, "Finite temperature dense matter studies on next-generation light sources," *J. Opt. Soc. Am. B*, vol. 20, pp. 770–778, Apr 2003.

[16] B. Nagler *et al.*, "Turning solid aluminium transparent by intense soft x-ray photoionization," *Nat Phys*, vol. 5, pp. 693–696, 09 2009.

[17] G. B. Stephenson, A. Robert, and G. Grubel, "X-ray spectroscopy: Revealing the atomic dance," *Nat Mater*, vol. 8, pp. 702–703, 09 2009.

[18] D. Fausti, R. I. Tobey, N. Dean, S. Kaiser, A. Dienst, M. C. Hoffmann, S. Pyon, T. Takayama, H. Takagi, and A. Cavalleri, "Light-induced superconductivity in a stripe-ordered cuprate," *Science*, vol. 331, no. 6014, pp. 189–191, 2011.

[19] A. W. *et al.*, "Operation of a free-electron laser from the extreme ultraviolet to the water window," *Nat Photon*, vol. 1, pp. 336–342, 06 2007.

[20] EmmaP. *et al.*, "First lasing and operation of an angstrom-wavelength free-electron laser," *Nat Photon*, vol. 4, pp. 641–647, 09 2010.

[21] M. Altarelli *et al.*, "Xfel: The european x-ray free-electron laser technical design report," tech. rep., Deutsches Elektronen-Synchrotron (DESY), 2007.

[22] B. D. Patterson *et al.*, "Coherent science at the swissfel x-ray laser," *New Journal of Physics*, vol. 12, no. 3, p. 035012, 2010.

[23] A. Zholents, "Next-generation x-ray free-electron lasers," *Selected Topics in Quantum Electronics, IEEE Journal of*, vol. 18, pp. 248–257, Jan 2012.

[24] G. Margaritondo and P. Rebernik Ribic, "A simplified description of X-ray free-electron lasers," *Journal of Synchrotron Radiation*, vol. 18, pp. 101–108, Mar 2011.

[25] Z. Huang and K.-J. Kim, "Review of x-ray free-electron laser theory," *Phys. Rev. ST Accel. Beams*, vol. 10, p. 034801, Mar 2007.

[26] S. N. A. Laboratory, "LCLS parameters." https://portal.slac.stanford.edu/sites/lclscore_public/Accelerator_Physics_Published_Documents/LCLS-parameters.pdf, 2014. [Online; accessed December-2015].

[27] R. Bonifacio, C. Pellegrini, and L. M. Narducci, "Collective instabilities and high-gain regime in a free electron laser," *Optics Communications*, vol. 50, pp. 373–378, July 1984.

[28] S. Krinsky and R. L. Gluckstern, "Analysis of statistical correlations and intensity spiking in the self-amplified spontaneous-emission free-electron laser," *Phys. Rev. ST Accel. Beams*, vol. 6, p. 050701, May 2003.

[29] E. Saldin, E. Schneidmiller, and M. Yurkov, "Statistical properties of radiation from {VUV} and x-ray free electron laser," *Optics Communications*, vol. 148, no. 4–6, pp. 383 – 403, 1998.

[30] E. Saldin, E. Schneidmiller, and M. Yurkov, "Coherence properties of the radiation from x-ray free electron laser," *Optics Communications*, vol. 281, no. 5, pp. 1179 – 1188, 2008.

[31] G. Vannucci and M. C. Teich, "Computer simulation of superposed coherent and chaotic radiation," *Appl. Opt.*, vol. 19, pp. 548–553, Feb 1980.

[32] S. P. Hau-Riege, "X-ray atomic scattering factors of low-z ions with a core hole," *Phys. Rev. A*, vol. 76, p. 042511, Oct 2007.

[33] L. Young *et al.*, "Femtosecond electronic response of atoms to ultra-intense x-rays," *Nature*, vol. 466, pp. 56–61, 07 2010.

[34] N. Rohringer and R. Santra, "X-ray nonlinear optical processes using a self-amplified spontaneous emission free-electron laser," *Phys. Rev. A*, vol. 76, no. 3, p. 033416, 2007.

[35] B. Rudek *et al. Nature Photon.*, vol. 6, pp. 858–865, 2012.

[36] P. L. M.G. Makris and A.Mihelič, "Theory of multiphoton multielectron ionization of xenon under strong 93-ev radiation," *Phys. Rev. Lett.*, 2009.

[37] K. Moribayashi, A. Sasaki, and T. Tajima, "Ultrafast x-ray processes with hollow atoms," *Phys. Rev. A*, vol. 58, pp. 2007–2015, Sep 1998.

[38] T. Kai, "Single-differential and integral cross section for electron-impact ionization for the damage of carbon clusters irradiated with x-ray free-electron lasers," *Phys. Rev. A*, vol. 81, no. 023201, 2010.

[39] S.-K. Son, L. Young, and R. Santra, "Impact of hollow-atom formation on coherent x-ray scattering at high intensity," *Phys. Rev. A*, vol. 83, p. 033402, 2011.

[40] M. Hoener *et al.*, "Ultraintense x-ray induced ionization, dissociation, and frustrated absorption in molecular nitrogen," *Phys. Rev. Lett.*, vol. 104, p. 253002, Jun 2010.

[41] J. P. Cryan *et al.*, "Auger electron angular distribution of double core-hole states in the molecular reference frame," *Phys. Rev. Lett.*, vol. 105, p. 083004, Aug 2010.

[42] L. Fang *et al.*, "Double core-hole production in $\mathbf{n}_2$: Beating the auger clock," *Phys. Rev. Lett.*, vol. 105, p. 083005, Aug 2010.

[43] L. Fang *et al.*, "Multiphoton ionization as a clock to reveal molecular dynamics with intense short x-ray free electron laser pulses," *Phys. Rev. Lett.*, vol. 109, p. 263001, Dec 2012.

[44] C. Buth, J.-C. Liu, M. H. Chen, J. P. Cryan, L. Fang, J. M. Glownia, M. Hoener, R. N. Coffee, and N. Berrah, "Ultrafast absorption of intense x rays by nitrogen molecules," *The Journal of Chemical Physics*, vol. 136, no. 21, 2012.

[45] Y. Hao, L. Inhester, K. Hanasaki, S.-K. Son, and R. Santra, "Efficient electronic structure calculation for molecular ionization dynamics at high x-ray intensity," *Structural Dynamics*, vol. 2, no. 4, 2015.

[46] C. Weninger and N. Rohringer, "Transient-gain photoionization x-ray laser," *Phys. Rev. A*, vol. 90, p. 063828, Dec 2014.

[47] V. Kimberg and N. Rohringer, "Stochastic stimulated electronic x-ray raman spectroscopy," *Structural Dynamics*, vol. 3, no. 3, 2016.

[48] A. Szabo and N. S. Ostlund, *Modern Quantum Chemistry: Introduction to Advanced Electronic Structure Theory*. New York: McGraw-Hill, 1st, revised edition ed., 1989.

[49] L. Rodney, *The Quantum Theory of Light*. Oxford:Oxford University Press, 1983.

[50] S. Weinberg, *The Quantum Theory of Fields*, vol. 1. Cambridge University Press, 1995.

[51] R. O. M. Born, "Zür quantentheorie der molekülen," *Ann. Phys.*, vol. 84, no. 457, 1927.

[52] J. D. Jackson, *Classical Electrodynamics*. John Wiley and Sons, 1975.

[53] G. M. Wysin, "Quantization of the free electromagnetic field: Photons and operators," August 2011.

[54] F. Schwabl, *Quantum Mechanics*. Springer-Verlag, 2007.

[55] F. Schwabl, *Advanced Quantum Mechanics*. Springer-Verlag, 2005.

[56] H. Friedrich, *Theoretical Atomic Physics*. Springer-Verlag, 2006.

[57] J. Andruszkow *et al.*, "First observation of self-amplified spontaneous emission in a free-electron laser at 109 nm wavelength," *Phys. Rev. Lett.*, vol. 85, pp. 3825–3829, Oct 2000.

[58] Y. Li, J. Lewellen, Z. Huang, V. Sajaev, and S. V. Milton, "Time-resolved phase measurement of a self-amplified free-electron laser," *Phys. Rev. Lett.*, vol. 89, p. 234801, Nov 2002.

[59] V. Ayvazyan *et al.*, "Generation of gw radiation pulses from a vuv free-electron laser operating in the femtosecond regime," *Phys. Rev. Lett.*, vol. 88, p. 104802, Feb 2002.

[60] C. Weninger, M. Purvis, D. Ryan, R. A. London, J. D. Bozek, C. Bostedt, A. Graf, G. Brown, J. J. Rocca, and N. Rohringer, "Stimulated electronic x-ray raman scattering," *Phys. Rev. Lett.*, vol. 111, p. 233902, Dec 2013.

[61] Y. R. Shen, "Quantum statistics of nonlinear optics," *Phys. Rev.*, vol. 155, pp. 921–931, Mar 1967.

[62] R. J. Glauber, "The quantum theory of optical coherence," *Phys. Rev.*, vol. 130, pp. 2529–2539, Jun 1963.

[63] S. J.C., "A simplification of the hartree-fock method," *Phys. Rev.*, vol. 81, no. 3, 1951.

[64] C. C. J. Roothaan, "New developments in molecular orbital theory," *Rev. Mod. Phys.*, vol. 23, no. 69, 1951.

[65] D. J. T. Daniela Kohen, "Quantum adiabatic switching," *J. Chem. Phys.*, vol. 98, no. 3168, 1993.

[66] J. J. Sakurai, *Modern Quantum Mechanics*. Addison-Wesley, 1994.

[67] K. Gottfried and T.-M. Yan, *Quantum Mechanics:Fundamentals*. Springer-Verlag, 2004.

[68] U.Gelius and K.Siegbahn, "Esca studies of molecular core and valence levels in the gas phase," *Faraday Discuss.Chem.Soc*, vol. 54, no. 257-268, 1972.

[69] J.-T. J.Huan and F. O. Ellison, "Esca: A theoretical intensity model based on the plane-wave approximation," *Journal of Electron Spectroscopy and Related Phenomena*, vol. 4, no. 233-242, 1974.

[70] M. Coville and T. D. Thomas, "Molecular effects on inner-shell lifetimes:possible test of the one-center model of auger decay," *Phys.Rev.A*, vol. 43, no. 6053-6056, 1991.

[71] R. Manne and H. Argen, "Auger transition amplitudes from general many-electron wave functions," *Chem. Phys.*, vol. 93, no. 201-208, 1985.

[72] E. Z. Chelkowska and F. P.Larkins, "Auger spectroscopy for molecules: Tables of matrix elements for transition-rate calculations corresponding to an s-,p-, or d-type initial hole," *Atomic Data and Nuclear Data Tables*, vol. 49, no. 121-206, 1991.

[73] S.-K.Son and R.Santra, *XATOM-an integrated toolkit for x-ray and atomic physics*. DESY, Hamburg, revision 398 ed., 2011.

[74] A. A. Sorokin, S. V. Bobashev, T. Feigl, K. Tiedtke, H. Wabnitz, and M. Richter, "Photoelectric effect at ultrahigh intensities," *Phys. Rev. Lett.*, vol. 99, p. 213002, Nov 2007.

[75] S.-K. Son and R. Santra, "Monte carlo calculation of ion, electron, and photon spectra of xenon atoms in x-ray free electron laser pulses," *Phys. Rev. A*, vol. 85, no. 063415, 2012.

[76] B. Ziaja, R. A. London, and J. Hajdu, "Ionization by impact electrons in solids: Electron mean free path fitted over a wide energy range," *Journal of Applied Physics*, vol. 99, no. 3, 2006.

[77] M. A. Mangan, B. G. Lindsay, and R. F. Stebbings, "Absolute partial cross sections for electron-impact ionization of co from threshold to 1000 ev," *Journal of Physics B: Atomic, Molecular and Optical Physics*, vol. 33, no. 17, p. 3225, 2000.

[78] R. Boyd, *Nonlinear Optics*. Academic Press, 2007.

[79] C. Weninger, *Propagation and Scattering of High-Intensity X-Ray Pulses in Dense Atomic Gases and Plasmas*. PhD thesis, Hamburg University, 2015.

[80] C. Weninger and N. Rohringer, "Stimulated resonant x-ray raman scattering with incoherent radiation," *Phys. Rev. A*, vol. 88, p. 053421, Nov 2013.

[81] M. Hirsch, S. Smale, and R. Devaney, *Differential Equations, Dynamical Systems, and an Introduction to Chaos*. No. v. 60

[82] D. Kiryanov and E.Kiryanova, *Computational Science*. David Pallai, 2007.

[83] I. O. for Standardization, "Natural gas – standard reference conditions (iso 13443)," Geneva,Switzerland, 1996.

[84] A. A. Lutman, R. Coffee, Y. Ding, Z. Huang, J. Krzywinski, T. Maxwell, M. Messerschmidt, and H.-D. Nuhn, "Experimental demonstration of femtosecond two-color x-ray free-electron lasers," *Phys. Rev. Lett.*, vol. 110, p. 134801, Mar 2013.

[85] Z. Deng and J. H. Eberly, "Multiphoton absorption above ionization threshold by atoms in strong laser fields," *J. Opt. Soc. Am. B*, vol. 2, pp. 486–493, Mar 1985.

[86] C. Buth, R. Santra, and L. Young, "Electromagnetically induced transparency for x rays," *Phys. Rev. Lett.*, vol. 98, p. 253001, Jun 2007.

[87] F. Krausz and M. Ivanov, "Attosecond physics," *Rev. Mod. Phys.*, vol. 81, pp. 163–234, Feb 2009.

[88] P. B. Corkum and F. Krausz, "Attosecond science," *Nat. Phys.*, vol. 3, no. 6, p. 381, 2007.

[89] F. Lepine, M. Y. Ivanov, and M. J. J. Vrakking, "Attosecond molecular dynamics: fact or fiction?," *Nat Photon*, vol. 8, pp. 195–204, 03 2014.

[90] F. Calegari, D. Ayuso, A. Trabattoni, L. Belshaw, S. De Camillis, S. Anumula, F. Frassetto, L. Poletto, A. Palacios, P. Decleva, J. B. Greenwood, F. Martín, and M. Nisoli, "Ultrafast electron dynamics in phenylalanine initiated by attosecond pulses," *Science*, vol. 346, no. 6207, pp. 336–339, 2014.

[91] P. M. Kraus and H. J. Wörner, "Time-resolved high-harmonic spectroscopy of valence electron dynamics," *Chemical Physics*, vol. 414, pp. 32 – 44, 2013. Attosecond spectroscopy.

[92] N. Gedik, D.-S. Yang, G. Logvenov, I. Bozovic, and A. H. Zewail, "Nonequilibrium phase transitions in cuprates observed by ultrafast electron crystallography," *Science*, vol. 316, no. 5823, pp. 425–429, 2007.

[93] T. R. M. Barends *et al.*, "Direct observation of ultrafast collective motions in co myoglobin upon ligand dissociation," *Science*, vol. 350, no. 6259, pp. 445–450, 2015.

[94] A. Pietzsch, A. Föhlisch, M. Beye, M. Deppe, F. Hennies, M. Nagasono, E. Suljoti, W. Wurth, C. Gahl, K. Döbrich, and A. Melnikov, "Towards time resolved core level photoelectron spectroscopy with femtosecond x-ray free-electron lasers," *New Journal of Physics*, vol. 10, no. 3, p. 033004, 2008.

[95] C. Bressler *et al.*, "Femtosecond xanes study of the light-induced spin crossover dynamics in an iron(ii) complex," *Science*, vol. 323, no. 5913, pp. 489–492, 2009.

[96] P. Wernet *et al.*, "Orbital-specific mapping of the ligand exchange dynamics of fe(co)5 in solution," *Nature*, vol. 520, pp. 78–81, 04 2015.

[97] B. K. McFarland *et al.*, "Ultrafast x-ray auger probing of photoexcited molecular dynamics," *Nat Commun*, vol. 5, 06 2014.

[98] A. Kotani and S. Shin, "Resonant inelastic x-ray scattering spectra for electrons in solids," *Rev. Mod. Phys.*, vol. 73, pp. 203–246, Feb 2001.

[99] A. Pietzsch, F. Hennies, P. S. Miedema, B. Kennedy, J. Schlappa, T. Schmitt, V. N. Strocov, and A. Föhlisch, "Snapshots of the fluctuating hydrogen bond network in liquid water on the sub-femtosecond timescale with vibrational resonant inelastic x-ray scattering," *Phys. Rev. Lett.*, vol. 114, p. 088302, Feb 2015.

[100] A. Pietzsch *et al.*, "Spatial quantum beats in vibrational resonant inelastic soft x-ray scattering at dissociating states in oxygen," *Phys. Rev. Lett.*, vol. 106, p. 153004, Apr 2011.

[101] P. A. Brühwiler, O. Karis, and N. Mårtensson, "Charge-transfer dynamics studied using resonant core spectroscopies," *Rev. Mod. Phys.*, vol. 74, pp. 703–740, Jul 2002.

[102] D. Ratner *et al.*, "Experimental demonstration of a soft x-ray self-seeded free-electron laser," *Phys. Rev. Lett.*, vol. 114, p. 054801, Feb 2015.

[103] A. J. *et al.*, "Demonstration of self-seeding in a hard-x-ray free-electron laser," *Nat Photon*, vol. 6, pp. 693–698, 10 2012.

[104] A. Marinelli, A. A. Lutman, J. Wu, Y. Ding, J. Krzywinski, H.-D. Nuhn, Y. Feng, R. N. Coffee, and C. Pellegrini, "Multicolor operation and spectral control in a gain-modulated x-ray free-electron laser," *Phys. Rev. Lett.*, vol. 111, p. 134801, Sep 2013.

[105] L. J. P. Ament, M. van Veenendaal, T. P. Devereaux, J. P. Hill, and J. van den Brink, "Resonant inelastic x-ray scattering studies of elementary excitations," *Rev. Mod. Phys.*, vol. 83, pp. 705–767, Jun 2011.

[106] S. Grenier, J. P. Hill, V. Kiryukhin, W. Ku, Y.-J. Kim, K. J. Thomas, S.-W. Cheong, Y. Tokura, Y. Tomioka, D. Casa, and T. Gog, "*d-d* excitations in manganites probed by resonant inelastic x-ray scattering," *Phys. Rev. Lett.*, vol. 94, p. 047203, Feb 2005.

[107] P. Marra, S. Sykora, K. Wohlfeld, and J. van den Brink, "Resonant inelastic x-ray scattering as a probe of the phase and excitations of the order parameter of superconductors," *Phys. Rev. Lett.*, vol. 110, p. 117005, Mar 2013.

[108] T. A. Carlson and M. O. Krause, "Electron shake-off resulting from *k*-shell ionization in neon measured as a function of photoelectron velocity," *Phys. Rev.*, vol. 140, pp. A1057–A1064, Nov 1965.

[109] P. Persson, S. Lunell, A. Szöke, B. Ziaja, and J. Hajdu, "Shake-up and shake-off excitations with associated electron losses in x-ray studies of proteins," *Protein Science*, vol. 10, no. 12, pp. 2480–2484, 2001.

[110] U. Saalmann and J.-M. Rost, "Ionization of clusters in strong x-ray laser pulses," *Phys. Rev. Lett.*, vol. 89, p. 143401, Sep 2002.

Acknowledgements

There are a lot of people I would like to thank who accompanied me in this long but exciting journey.

First and foremost, I would like to express my gratitude to my advisor, Nina Rohringer. Thank you for reading my e-mail which explained my interests in your research field and for giving me the opportunity to make research within your group. During my stay in Hamburg, you always encouraged me to participate in seminars, to attend to your lectures at Universität Hamburg, to be part of the data analysis team during FLASH beamtime, among other enriching experiences. I can assure you that I enjoyed all and tried to learn as much as I could from them. Also, thank you for your patience and the many discussions we had. Surely, I developed more physical intuition from them.

I would like to thank the CFEL-DESY Theory Division, particularly to Ludger Inhester, Sang-Kil Son and Robin Santra. Thanks for sharing me your rate equation code and all the transition rates calculated by `XMOLECULE` toolkit, so that I could complete the project I am currently presenting. But also, for all the discussions we had related to the theoretical foundations of `XMOLECULE` -which certainly helped a lot for writing this work- and, of course, thanks for co-examining this thesis.

Without the financial aid provided by the UNAM-DGECI student mobility programme I would not have gotten the experience I actually have. Similarly, thanks to Bremen Universität, who allowed to stay one more semester in Germany so that I could research in Hamburg. Right at the same time, thanks to the Max-Planck-Institut für Struktur und Dynamik der Materie (MPSD) and the Center for Free-Electron Laser Science (CFEL) for facilitating me to introduce myself in a cutting-edge research field.

Importantly, I am very happy to have worked and shared time with the current and previous members of the ”X-ray Quantum Optics” group at the

MPSD. Jhih-An You, Song Bin Zhang, Wen-Te Liao, Clemens Weninger and Laurent Mercadier. Thank you for the very nice time in Hamburg. Laurent and Jhih-An, thank you for explaining me bunch things related with High-Harmonic Generation. Today is as well my favorite research area. I am also thankful for all the people I met at CFEL: Luis Zapata, Kelly Collette, Sonia Utermann, Kathja Schröder, Andrea Freund and Carolin Wodars.

Many many thanks to you, my friend Clemens. Despite the fact you were tired, and you were rush to finish your thesis, you were always willing to help me with the many questions I had during my stay at the MPSD. I definitely appreciate your patience and all the tips I learned from you for `Python` and, in general, for programming. I also gain a lot of physical intuition in our discussions and realized how much I need to learn. Thanks' to you I also want to learn how to code in `C++` and to get into machine learning. Besides, I think that the very good friendship we built is because we love beer, party and a lot more things.

Also I would like to thank José Ignacio Jiménez Miér y Terán, who never declined to support many of the projects I undertook during my undergraduate's degree. Thank you for your encouragement that made possible this work, and for your enthusiasm for co-examining my thesis.

I appreciate the help and knowledge provided by Wolfgang Bietenholz. The programming skills in `FORTRAN` I developed while doing my social service under your supervision, absolutely enabled the execution of this work.

I would like to thank also Mirna Villavicencio Torres, whom from the remoteness supported the extension of my visa for staying more time in Germany, so that I could embark myself in this scientific journey. Likewise, for helping me to submit this thesis in English. Here, I would like also to express my gratitude to Fernando Ramírez for the useful comments on how to write the statement for the faculty's committee to present this work in English.

Of course, I am thankful for having learned over all these years at Facultad de Ciencias from amazing -the best- professors. Among them are Javier Páez, Faustino Sánchez, Víctor Romero and José Ignacio Jiménez. Your motivation while giving lectures and passion for science is indeed very contagious. Without the knowledge you transferred me I would not have been prepared to undertake this project.

The professors that left their door open for me, so that I could obtain a bit of experience in research by working with them as an intern: Guy Paic, Enrique Patiño and José I. Jiménez from Insituto de Ciencias Nucleares, as well as Margarita Rosado and Xavier Hernández Doring from Instituto de Astronomía.

I am delighted to have truly lifelong friends such as Tomás Santiago (alias "el Dirac") and Luis Pérez (alias "el guapo") from Facultad de Ciencias. All

these (almost) 6 years would not have been so funny and so enlightening without you, guys. Thank you for being able to discuss with me many of the weekly-assigned problems.

To the university that promotes the diffusion and advancement of science and culture all over Mexico: Universidad Nacional Autónoma de México (UNAM). I will always be indebted to UNAM, from which I am so proud of having graduated.

Thanks to my soulmates César García and Rosario Molina who always make the day brighter.

Finally, I thank to my family. My father Miguel Angel Silva Méndez, my beautiful mother María Guadalupe Toledo Espinosa and my dummy and stinky siblings, Aldo and Aline.